Molecular Design of Polymeric Feedstocks Tailored for Additive Manufacturing Guided by Polymer Science Principles

A Dissertation Presented for the

Doctor of Philosophy

Degree

The University of Tennessee, Knoxville

Akan Archibong George

December 2024

Dedication

This dissertation is dedicated to my late parents. I wish they were here to witness this academic dream come true. I also dedicate this work to my beloved wife, Justina George, and my son, Levi George, whose unwavering support has been my strength throughout this journey.

Acknowledgements

I would like to express my deepest gratitude to my advisor, Dr. Mark Dadmun. His financial and academic support have been instrumental in making this dissertation possible. My gratitude extends to my committee members: Dr. Rigoberto Advincula, Dr. Alexei Sokolov, and Dr. Shawn Campagna, for their time and deliberation throughout my PhD program. I thank all my colleagues in my research lab, past and present: Dr. Austin W. Riggins, Leondra S. Lawson, Kaizhong Guan, Dr. Josh Moncada, Dr. Jacob E. Fischer, Dr. Connor Perryman, Shelby Watson, Bailey Eberle, Dr. Nadim Hmeidat, Dr. Ashraf Haque, Dr. Neiko Levenhagen, Timothy Taylor, Sakunthala Wijesundera, Mrinalini Ayilliath Kolaprath, Saifuddin Ahmed, Mahmudul Hasan, Bhanuka Ekanayake, Susan Kenny, and Dr. Alison Biery for their support. I appreciate all my peers in the Chemistry department who have contributed to my academic success in various ways. Special thanks to my collaborators at Virginia Tech: Dr. Christopher Williams, Dr. Jack Bryant, and Dr. Michael J. Bortner, for the fruitful collaborations. Finally, I would like to express my gratitude to everyone outside the University of Tennessee who supported and believed in me throughout these years of my PhD program.

Abstract

Two widely used polymeric additive manufacturing (AM) techniques are powder bed fusion (PBF) and fused filament fabrication. These techniques enable the creation of complex geometries from digital models in a layer-by-layer fashion. However, structures created using these methods often exhibit weak mechanical performance and anisotropy compared to those produced by traditional manufacturing techniques, such as injection molding. Factors such as poor interlayer and interparticle adhesion, residual stress, large voids, and insufficient chain entanglement between layers contribute to the inferior mechanical performance and anisotropic behavior of parts processed by AM. Additionally, the range of polymeric feedstocks available for AM techniques is limited. To address these issues, this dissertation applies polymer science principles to design polymeric materials by controlling their molecular characteristics to form robust structures using polymeric AM. In Chapter 2, the coalescence in polypropylene (PP) powders is enhanced by blending low molecular weight (LMW) PP with high molecular weight (HMW) PP. Using the Hopper coalescence model, the results indicate that the viscosity of the powder and extensional flow dominates the coalescence process. In Chapter 3, the impact of blending LMW with HMW PP on the properties of structures processed via PBF are examined. The results demonstrate that structures formed from the PP MW blend exhibit reduced void space, increased crystallinity, and improved thermomechanical behavior compared to those printed from neat HMW PP powders. Chapter 4 employs liquid-liquid phase separation to create powders that are blends of polycarbonate (PC) and PP matrix, with the goal of correlating the presence of PC in the powder on the crystallization of PP in the PBF process. The results reveal notable variation in the crystallization behavior and crystal structure of PP, including an accelerated crystallization rate and reduction in lamellar thickness. Finally, Chapter 5 examines

the effect of ultraviolet (UV) light on the material extrusion AM of PC. UV exposure causes fragmentation of PC chains, creating smaller chains that facilitate interlayer diffusion, reduce interlayer voids, and strengthen the PC-printed parts. Ultimately, the feedstock formulation protocols presented in this dissertation offer straightforward and cost-effective approaches to develop and produce mechanically robust polymeric structures using AM techniques.

Table of Contents

List of Tables

List of Figures

Chapter 1: Introduction

An Introduction to Additive Manufacturing

Additive manufacturing (AM), also known as 3D printing, is a revolutionary technology that enables the creation of three-dimensional objects from digital models.[1,2] Unlike traditional manufacturing methods that involve subtractive processes, where materials are removed to create the desired shape, 3D printing builds objects layer by layer, adding material until the desired shape is achieved.[1] This process offers unprecedented design freedom, allowing for the production of complex geometries and customized products with relative ease.

The process of 3D printing begins with the creation of a digital 3D model of the desired structure using computer-aided design (CAD) software.[3,4] This digital model serves as the blueprint for the physical object. The digital model is then exported into a slicing software, where the software slices the model into numerous thin horizontal layers and generates the corresponding G-code instructions that the 3D printer can read and fabricate the desired structure layer by layer.[3,4]

Additive Manufacturing Techniques and Application

Various AM technologies, including powder bed fusion, material extrusion, vat photopolymerization, sheet lamination, material jetting, binder jetting, and directed energy deposition have been developed [5] to print a diverse range of materials, including polymers, ceramics, metals, composites, wood, glass, and even foodstuffs.[6] 3D printing is utilized in a wide variety of industries and applications, including aerospace, medicine, prototyping, hobbies, and education.[7]

3D printing is a promising technology, but it has its challenges. A significant issue, particularly with the material extrusion 3D printing, is the anisotropic behavior of the fabricated parts.[8,9] Anisotropy in 3D printing refers to the variation in mechanical properties when

comparing the properties of parts printed in orthogonal directions, for instance in the longitudinal direction (parallel to the bed, XY direction) vs. in the transverse direction (perpendicular, Z direction), as illustrated in **Figure 1**. [8] This problem arises due to poor polymer chain diffusion and insufficient chain entanglement across adjacent layers during printing, and the presence of void spaces between printed layers.[10] Consequently, weak interlayer bonds form within the printed object, leading to structural weakness of printed parts in the perpendicular direction compared to parts printed in the longitudinal direction.[8-10]

Previously, numerous researchers have focused on optimizing printing parameters to reduce anisotropy and enhance mechanical properties in 3D printed parts.[10] However, adjusting print settings yields only marginal improvements in the mechanical properties of the printed components and minor reduction in anisotropic behavior.[10] As a result, current studies have shifted focus towards material design and simple modifications of the printing process to better address structural anisotropy in the final printed structures.[4, 8-10]

Another major drawback associated with 3D printing is the limited variety of materials available for printing.[11-13] Although tens of thousands of polymers have been optimized for traditional manufacturing methods like injection molding, only about 30 are suitable for polymer powder bed fusion.[13] The limitations in 3D printing feedstocks stem from several factors, including the need for materials compatibility with specific printing technologies, the required performance characteristics of the final product, and the cost of producing these feedstocks. For successful 3D printing, materials must be developed to exhibit suitable service properties compatible with specific techniques.[14] This often requires specific formulations to tailor the intrinsic and extrinsic properties of the feedstocks to ensure successful printability and desired

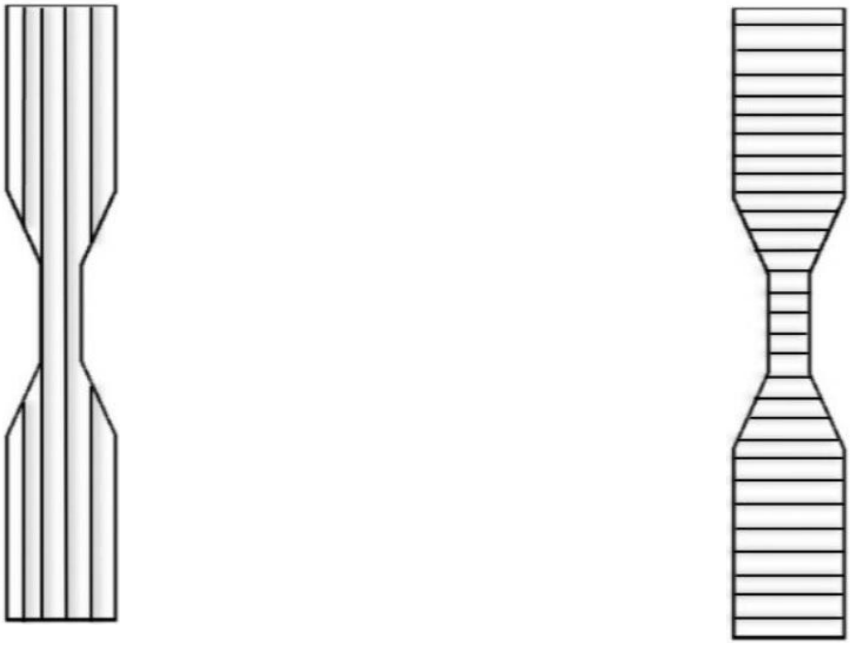

Figure 1. Printed layer orientations in Z-direction (right) and XY-direction (left).[8]

printed part properties. Developing feedstock formulations tailored for 3D printing is challenging and expensive, and it remains a key research area in additive manufacturing.[14]

To address this issue, this dissertation provides fundamental information that fosters the development of new polymeric materials suitable for powder-based and extrusion-based additive manufacturing. This dissertation utilizes fundamental principles of polymer science to design and control the molecular characteristics of polymeric feedstocks, rather than altering printing parameters, to enhance the quality and mechanical performance of 3D printed structures.

Principles of Powder Bed Fusion Additive Manufacturing

Powder Bed Fusion (PBF), also known as selective laser sintering, is continuously evolving as a crucial and transformative technology in the field of additive manufacturing. It drives innovation and opens new possibilities for designing and producing complex features that are difficult to fabricate with traditional injection molding techniques.[15,16] Currently, PBF additive manufacturing is utilized not only in prototyping but also in fabricating functional, complex structures used in the aircraft industry and medical field.[15-18]

As the name implies, PBF involves using powder feedstocks in the fabrication process, where laser energy selectively fuses and melts the powder particles layer by layer to create a three-dimensional object.[18] These powder feedstocks can be ceramic, metal, or thermoplastic.[15] A thorough understanding of the relationship between the powder characteristics and the PBF process is fundamental to achieving robust final printed part performance. A typical polymer PBF additive manufacturing process involves the following steps in sequence:

(1) *Powder deposition and preheating:* The powder bed is preheated up to a part bed temperature (Tb), then a thin layer of powder is spread across the build platform using a recoating blade or roller. For semicrystalline polymers, Tb is set close to the material's melting temperature, while for amorphous polymers, it is set close to the glass transition

temperature. Tb is the controlled temperature of the powder on the build platform during fabrication, which helps reduce laser power requirements and minimize distortion in the printing process.[19,20]

During the powder deposition process, layers of powder are spread sequentially without applying external pressure.[21] Achieving homogeneous and densely packed layers is crucial for producing dense and high-performance printed structures.[22] The physical characteristics of the powder, particularly its particle size and shape, significantly influence the quality of each deposited layer.[21,22] Spherical particles are known to enhance packing efficiency due to their superior flowability, resulting in a more uniform and tightly packed bed compared to irregularly shaped particles.[21]

(2) *Scanning of the polymer layer by laser:* After the powder deposition and preheating stage, a laser scans over the powder, selectively melting and consolidating the powder particles according to the pattern specified by the cross-sectional slice of the CAD file. The energy supplied by the laser is typically quantified by energy density. Energy density is a composite value that incorporates several key printing parameters of PBF machines, including laser power, beam velocity, hatch spacing, and laser diameter.[22,23]

To consolidate powder particles using a laser, the laser must interact with the powders through reflection, absorption, and transmission.[21] This interaction melts the powder, forming a melt pool.[22] The consolidation of particles in the melt pool is governed by droplet coalescence during the printing process. The degree of coalescence determines the final properties of the printed parts. Insufficient coalescence leads to poor interparticle fusion, large voids in the printed structures, and weakened mechanical strength of the parts. Thus, controlling the molecular characteristics of polymeric feedstocks to improve coalescence and decrease void space is imperative to producing

robust parts in powder bed fusion process. The rate of coalescence of polymeric materials in PBF process is inversely proportional to the material's viscosity.[24] Thus, polymers with low melt viscosity are ideal for the PBF process. Reducing the viscosity to an appropriate range for PBF process can be achieved by controlling the molecular weight of the polymer.[24]

(3) *Lowering the build platform:* Once the consolidation of first layer is completed, the build platform lowers by one layer thickness (10-300µm) and a fresh layer of powder is deposited onto the pre-sintered object.[15]

(4) *Repeating the process:* Steps 2 and 3 are repeated until the entire object is built. The unsintered powder acts as a support material, eliminating the need for additional support structures.[15]

An illustration of a typical polymer PBF fabrication process is shown in **Figure 2**.

Thermally Induced Phase Separation for Polymeric Powder Formation for PBF

An essential aspect of creating a new material for PBF is the production of powder particles that are appropriate for the process. Various production approaches, including cryogenic grinding and melt emulsification, have been employed to create powder feedstocks for PBF.[26-29] However, cryogenic grinding often results in irregularly shaped particles and poor particle distribution, which can negatively impact PBF processability and weaken the mechanical properties of the fabricated structures.[27,28] Melt emulsification techniques require more complex equipment and make the removal of surfactant challenging.[27]

A viable and economical method to produce polymeric powders suitable for the PBF process is thermally induced phase separation (TIPS).[13,15, 26-29] The process of TIPS begins by dissolving the polymer in a suitable solvent at an elevated temperature. Upon cooling the polymer solution, liquid-liquid phase separation followed by particle nucleation and growth and

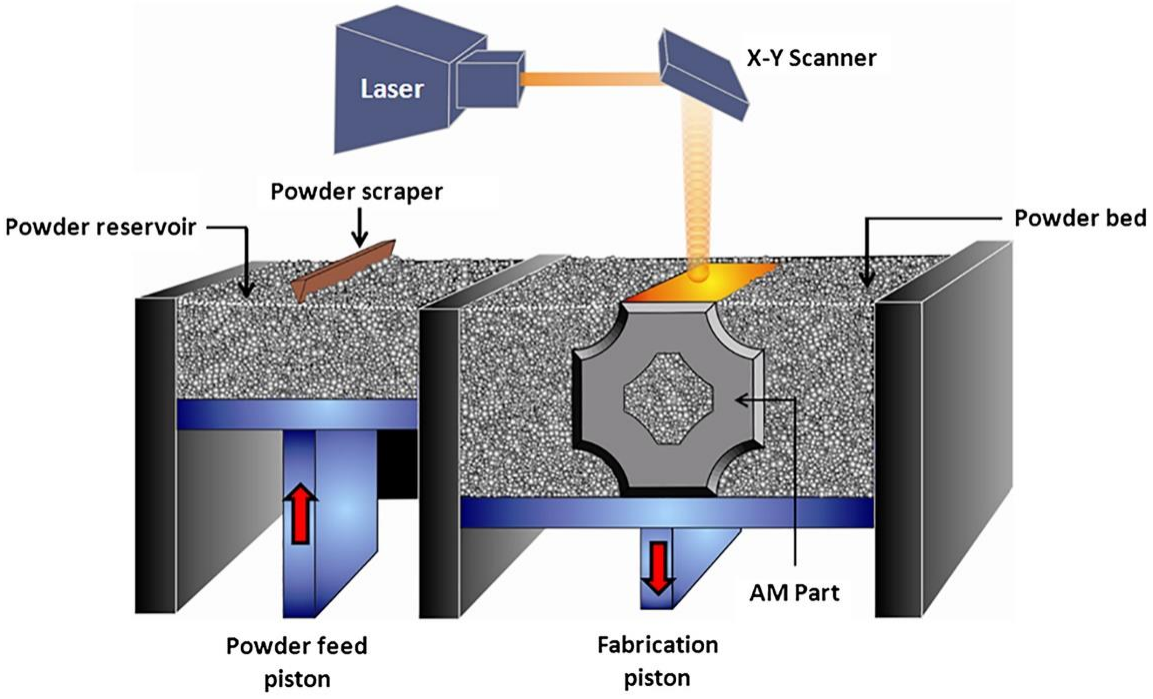

Figure 2. A diagrammatic representation of laser powder bed fusion printing process. [25]

precipitation occurs.[29] After the TIPS process, the solvent is typically removed through filtration, leaving behind the polymer powder with tailored properties.[13] By carefully controlling the cooling temperature, polymer concentration, solvent composition, and polymer molecular weight, TIPS can produce powders with tailored properties, including spherical powders with smooth surfaces and appropriate particle sizes ideal for the PBF process.[13,15,19]

Chapters 2-4 of this dissertation present the results of studies employing the TIPS method to create tailor-made polymer powders for PBF, including polypropylene, polycarbonate, and polypropylene-polycarbonate blend powders. Forming these powders from various polymers with a wide range of molecular weights expands the polymeric materials library for PBF printing, addressing a current limitation and opening new avenues for advancing PBF application fields.

Principles of Material Extrusion Additive Manufacturing

Material extrusion additive manufacturing, also known as melt extrusion additive manufacturing, is a 3D printing technique where material is precisely dispensed through a 3D printer nozzle during fabrication.[3,10,23,30] A common example of this technology is fused filament fabrication (FFF).[30] In FFF, a thermoplastic filament is fed through a heated nozzle, melted, and then extruded. The 3D printer's nozzle head moves to deposit the molten material onto the build plate according to G-code instructions for each layer. This process is repeated layer by layer until the entire object is fully formed.[3,10] A schematic diagram of the FFF process is shown in **Figure 3**.

As previously mentioned, a significant limitation of objects produced by FFF is the anisotropy in material properties compared to those created using the PBF process.[15] One primary reason for this is the limited entanglement of polymer chains between filaments at the

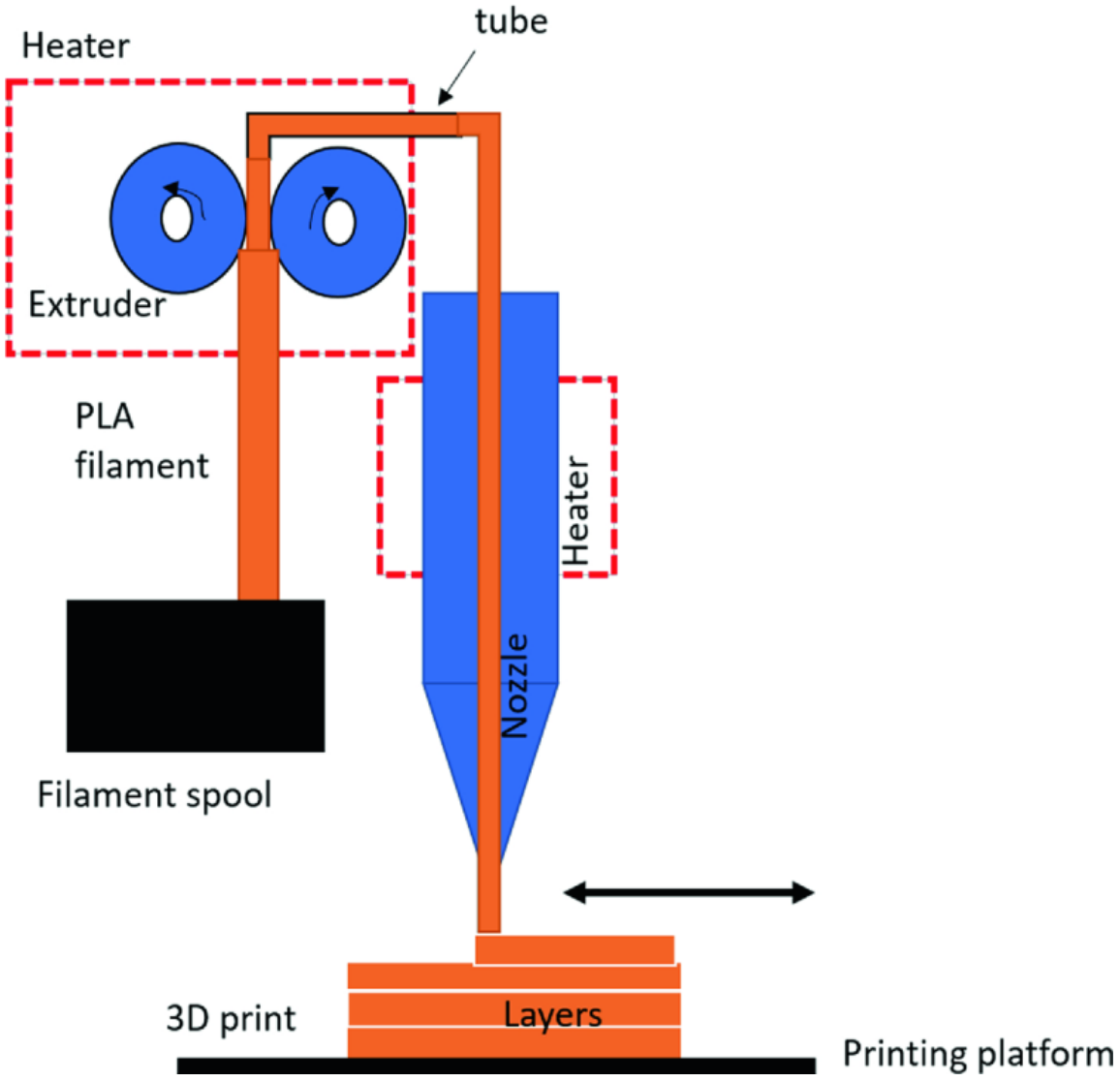

Figure 3. Schematic of fused filament fabrication process.[3]

interlayer interface, leading to significantly weaker adhesion between filaments compared to the stronger interparticle bonding observed in the PBF process.[15]

Previous studies by Levenhagen et al. and Perryman et al. in our research group applied a material design strategy to mitigate anisotropy in FFF-printed structures and enhance their mechanical properties. Levenhagen et al. employed ultraviolet (UV) irradiation to induce crosslinking in bimodal blends consisting of end-functionalized linear and three-arm poly(lactide) (PLA), along with linear PLA in the FFF filament.[31] Their findings demonstrated significant enhancement in the transverse maximum tensile stress of the printed parts, aided by 0.5% 2,2-dimethoxy-2-phenylactophenone photoinitiator incorporation and exposure to UV light. This improvement is attributed to the formation of covalent bonds between layers, facilitated by the diffusion and reaction of low molecular weight reactive species at the interfilament interface during the deposition process.[31] Levenhagen et al. also demonstrated that integrating surface-segregating materials into acrylonitrile-butadiene-styrene (ABS) filaments accelerates polymeric diffusion and interlayer adhesion between filaments, thereby enhancing the isotropic performance of the FFF printed structures.[8] Perryman et al. found that introducing crosslinkers between ABS filaments during the deposition process reduces the anisotropic performance of the FFF fabricated structures.[10]

While the material design strategies employed by Levenhagen et al. and Perryman et al. decrease the anisotropic performance of FFF fabricated structures and enhance their mechanical properties, the design strategies are associated with several challenges. These include the complex synthesis process of the new feedstocks, which can be costly and time-consuming, and the requirement for specific delivery methods to introduce crosslinkers to the interfilament interface, complicating the printing process. Thus, simplification of material design will improve the manufacturing efficiency in the FFF process and the resulting mechanical performance of the

printed parts. Chapter 5 of this dissertation presents a cost-effective protocol that enhances the quality and mechanical performance of polycarbonate printed by the FFF process, where synthesizing additional materials, utilizing additives, or employing crosslinkers are unnecessary.

Impact of Coalescence of Polymeric Feedstocks on Additive Manufacturing

Coalescence refers to the process where individual particles or layers of material merge together to form a single homogenous body. The extent of coalescence of polymeric feedstocks during printing significantly impacts the quality and properties of objects produced through 3D printing techniques, including PBF and FFF.[21,22,32-37] When polymeric feedstocks coalesce effectively during printing, the resulting material exhibits better bonding between layers, leading to enhanced durability and reduced likelihood of defects such as large voids in the printed structures.[34] Thus, understanding and controlling the physics of coalescence process is vital to advance additive manufacturing technologies, which may enable the production of high-quality parts with tailored properties for specific applications.

In 3D printing, the joining formation process through coalescence involves surface contact, followed by neck formation, and finally neck growth with molecular diffusion at the interface.[34,35] These processes are illustrated in **Figure 4**.[34] Neck growth occurs through two modes: the initial zipping mode, driven by adhesive intersurface forces, followed by the stretching mode, driven by curvature-based surface tension forces.[32,38,39] The quality of the adhesion between surfaces depends on the extent of neck growth[35]; the larger and more developed the neck, the stronger the adhesion. The coalescence of particles is driven by two temperature-dependent properties: surface tension (Γ) and zero-shear viscosity (η_0) of the polymer,[21,22,35] as described by the Frenkel model shown in Equation 1.

$$\frac{y}{a_0} = \left(\frac{3\Gamma t}{2a_0\eta_0}\right)^{\frac{1}{2}} \qquad Eq.\,1$$

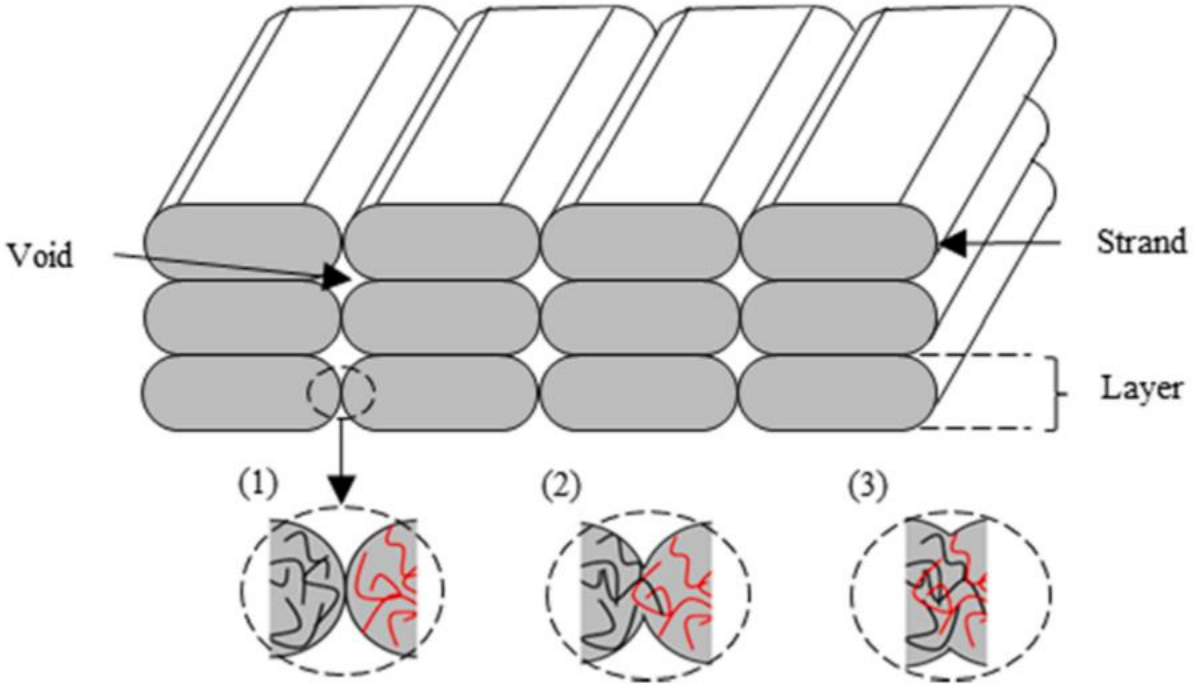

Figure 4. Bond formation process via coalescence: (1) Surface contact; (2) Neck formation; (3) Neck growth with molecular diffusion at the interface.[34]

In Equation 1, a_0 is the particle radius, y is the particle neck radius, $\frac{y}{a_0}$ monitors the neck growth, and t is the coalescence time.[21,22] Achieving sufficient coalescence between filaments in the FFF process and between powder particles in the PBF process will benefit from a polymer feedstock with sufficiently low viscosity to enhance material flow.[35] In injection molding, high shear rates are applied to the molten polymer, reducing its melt viscosity and facilitating flow to completely fill the mold. In contrast, PBF imposes no shear on the molten polymer. Therefore, particle coalescence depends on the zero-shear viscosity of the polymer melt at the processing temperature. [22] The surface tension of a polymer does not vary significantly with temperature and molecular weight.[21,40-42] In contrast, the zero-shear viscosity (η_0) of a polymer is highly dependent on its molecular weight (Mw) as described by Equation 2, where k is a constant.[43]

$$\boldsymbol{\eta_0 = k\, Mw^{3.4}} \qquad \boldsymbol{Eq.2}$$

Studies have shown that the polymer flow during the particle coalescence process is extensional rather than shear flow.[33,44,45] Therefore, when analyzing and predicting the extent of coalescence in PBF, one should consider the polymer properties that are relevant to extension flow, such as extensional viscosity at low rates.[33,44] Although extensional viscosity is often difficult to measure experimentally, the Trouton ratio can be used to approximate extensional viscosity (η_e) from shear viscosity at low shear rates, as shown in Equation 3.[33,43,44]

$$\boldsymbol{Trouton\ ratio} = \frac{\eta_e}{\eta_0} \qquad \boldsymbol{Eq.3}$$

Importance of Polymer Diffusion in Additive Manufacturing

Polymer diffusion plays a crucial role in FFF additive manufacturing, significantly influencing the mechanical properties and quality of the final printed structures.[8,30] In FFF, a thermoplastic filament is heated and extruded layer by layer to build a part. During this process,

polymer chains must diffuse across the interfaces of adjacent layers to form interlayer entanglements and strength.[46] Effective diffusion of polymer chains ensures stronger interlayer strength, improved coalescence and entanglement across interfilament interfaces, and reduced voids, thereby enhancing the overall structural integrity and mechanical performance of the printed object.[8,30,46] One crucial polymer property that profoundly affects its diffusive behavior is its chain length, its molecular weight. In fact, it is understood that smaller polymer chains diffuse more rapidly compared to larger polymer chains, where Equation 4 shows that the diffusion coefficient (D) of a polymer is inversely proportional to the square of its molecular weight (Mw).[47]

$$\boldsymbol{D \sim Mw^{-2}} \qquad \boldsymbol{Eq.4}$$

Equation 5 illustrates that D is directly proportional to the distance ($\bar{x}^2$) that the center of mass of a polymer chain diffuses over a given time (t) in three dimensions.[46]

$$\boldsymbol{\bar{x}^2 = 6Dt} \qquad \boldsymbol{Eq.5}$$

Equations 4 and 5 quantify the extent to which, that, under identical experimental conditions, larger polymer chains take longer to diffuse across or between interlayer interfaces, as they will transverse a shorter distance than smaller polymer chains within the same timeframe.

Impact of Polymer Crystallization on Additive Manufacturing

When polymers are heated and then cooled during the AM process, they may undergo crystallization in the temperature range between the glass transition and melting temperatures of a semi-crystalline polymer. During the crystallization process, the polymer chains align into ordered structures on molecular length scales.[4] When crystallization occurs, the resulting crystals inhibit the diffusion of macromolecular chains during coalescence, leading to weaker interlayer or interparticle interfaces and consequently poor mechanical properties in the printed

components.[22,23,33,34] Studies have shown that a high degree of crystallinity and the formation of larger crystals during the 3D printing process results in significant dimensional errors and reduced elongation at break of the printed parts.[23,48-50] However, it should be kept in mind that increased crystallinity can improve the tensile strength of 3D printed structures. Thus, this emphasizes the complexity of the importance of tuning crystallization of polymer in AM process, requiring sufficient crystallinity to achieve desired mechanical performance of the printed components without limiting the important coalescence processes during printing.

Crystallization starts with nucleation and advances through crystal growth.[51,52] Nucleation refers to the formation of nuclei. Once the nuclei are formed, then crystals grow from the nuclei.[52] When all nucleation sites appear simultaneously at the beginning, it is known as instantaneous nucleation. Conversely, if nuclei form steadily throughout the polymer volume over time, it is called sporadic nucleation.[52] Moreover, crystalline polymers are structured at different length scales: unit cells, lamellae, and spherulites.[4] The unit cell is the smallest repeating unit in a crystal lattice, with the dimensions usually on the order of angstroms.[4] Lamellae, formed by the folding of polymer chains, typically have a thickness between 100 and 500 angstroms and a width in the micrometer range.[4] Spherulites, the largest structures, range from micrometers to millimeters and are formed by the arrangement of lamellae.[4] Material manipulation to control the crystallization rate and crystal size is a crucial aspect of the research presented in this dissertation. Therefore, the following section provides a detailed summary of methods used to understand crystallization kinetics.

Avrami and Isothermal Differential Scanning Calorimetry

Isothermal differential scanning calorimetry (DSC) is an analytical technique used to measure the heat flow associated with process, including phase transitions in a material while maintaining a constant temperature. DSC is an important tool used to determine the change in

heat capacity of a material as a function of temperature. In this method, a small, weighed sample (5-10mg) is placed in a sample pan, and an empty reference pan is used for comparison. Both pans are heated at the same rate. The difference in the heat flow between these pans is then recorded as a function of time or temperature in a controlled atmosphere. This heat flow data reflects the heat needed to increase the temperature of the sample, including any physical or chemical changes that may occur. This data may be analyzed to elucidate the material's thermodynamic properties or reaction kinetics.

In this dissertation, the Avrami approach (Equation 6)[53,54] to analyze the crystallization kinetics of polycarbonate-polypropylene blended powders is employed.

$$\boldsymbol{X\,(t) = 1 - e^{-Kt^n} \qquad Eq.6}$$

In Equation 6, $X\,(t)$ represents the relative crystallinity of the sample, t is the crystallization time, n is the Avrami exponent, and K is the crystallization rate constant. $X\,(t)$ can determined in terms of the heat generated at time t (Q_t), heat generated at infinite time (Q_∞), and heat evolution rate $\left(\frac{dH}{dt}\right)$, as shown in Equation 7.[53,54] Both Q_t and Q_∞ are derived from the integration of crystallization peak in the DSC curves.

$$\boldsymbol{X(t) = \frac{Q_t}{Q_\infty} = \frac{\int_0^t \left(\frac{dH}{dt}\right) dt}{\int_0^\infty \left(\frac{dH}{dt}\right) dt} \qquad Eq.7}$$

By applying the logarithm to both sides of Equation 6, the Avrami equation can be transformed, resulting in Equation 8.

$$\boldsymbol{\log\left[-\ln\left(1 - X(t)\right)\right] = n\log(t) + \log K \qquad Eq.8}$$

Thus, plotting $\log\left[-\ln\left(1 - X(t)\right)\right]$ as a function of log (t) allows for the determination of the Avrami exponent, *n*, from the slope of the resulting line and the crystallization kinetic constant,

K, from the intercept with the y-axis. The crystallization rate constant and Avrami exponent can also be expressed in terms of crystallization half-time, $t_{1/2}$, as shown in Equation 9.

$$t_{1/2} = \left(\frac{\ln 2}{K}\right)^{\frac{1}{n}} \qquad Eq.\,9$$

$t_{1/2}$ is the time at which the crystallinity reaches 50% of the final value. Consequently, a higher $t_{1/2}$ value indicates a slower crystallization rate.[53]

The Avrami exponent is influenced by the nucleation mechanism and the geometry of crystal growth.[55-57] Thus, variations in the Avrami exponent provide information on the nucleation mode and the geometry of the crystals.[55-57] Specifically, an Avrami exponent of n =1 corresponds to one-dimensional crystal growth, such as rods; n=2 corresponds to two-dimensional growth, like disks; and n=3 corresponds to three-dimensional growth, such as spheres.[55-57] The Avrami equation provides a powerful framework to analyze experimental crystallization data, enabling the determination of growth geometry and nucleation mechanism. Consequently, it serves as a crucial model for studying the kinetics of polymer crystallization.

Role of Polymer Molecular Weight and Polymer Blend in the Fabrication of 3D Printed Structures

The molecular weight (chain size) of polymers plays a crucial role in determining the printability and mechanical properties of printed structures.[4,46] During printing, polymer molecular weight affects viscosity, melt flow behavior, and polymer chain entanglement.[46] Blending polymers of different molecular weights enables the customization of polymer molecular characteristics, such as viscosity, to potentially optimize both printability and mechanical performance of structures processed by AM technologies.[46] As previously discussed, the size of the polymer chains is an important factor that influences the diffusion of chains across interlayer interfaces during the printing process. Levenhagen et al. showed that adding lower

molecular weight (LMW) polymers to higher molecular weight (HMW) FFF filament substantially enhances the diffusion of the polymer sample.[58] This, in turn, improves the interfacial adhesion between layers in objects created through the FFF process. LMW additives in a polymer melt tend to migrate rapidly to the filament interface, where they can form entanglements between layers more quickly than their HMW counterparts.[58]

Surface segregation of polymer chains at the interfilament interface is a powerful opportuntiy for minimizing void spaces and enhancing the mechanical properties of structures created through FFF.[8,59] The tendency for polymer chains to migrate to the interfilament interface depends on their size; smaller polymer chains generally segregate to the interfilament interface more easily than larger ones, which improves adhesion between adjacent filaments.[8,59] This surface segregation is, at least partially, driven by the tendency of polymer chain ends to migrate to the surface of the polymer melt due to entropic effects.[60-62] The size of the polymer affects the number of chain ends: as the polymer molecular weight increases, the number of chain ends decreases.[62] Studies by Chen et al. showed that interfacial adhesion at a polymer-polymer interface improves as the number of polymer chain ends at the interface increases.[62] They interpreted these results to indicate that the enhanced mobility of chain ends promotes a higher rate and deeper interpenetration of the chains across the polymer interface, resulting in a more extensive polymer network and thus improving adhesion.[62]

Recognizing the crucial role of polymer molecular motion in particle coalescence during the PBF process, Chapters 2 and 3 of this dissertation employ the strategy of incorporating LMW polymers to modulate the molecular motion of HMW polypropylene powders. Incorporating LMW results in a significant reduction in the zero-shear viscosity of HMW polypropylene powders, thereby enhancing their droplet coalescence during printing and the mechanical

properties of the printed parts. These results are thoroughly discussed in Chapters 2 and 3 of this dissertation.

Thermodynamics of Phase Separation in Polymer Blends

Blending two or more polymers may create new materials that combine the properties of each polymer, resulting in a single material with tailored characteristics.[63] However, most polymer blends tend to phase separate into distinct phases, which can affect the resulting material's properties. Therefore, understanding the thermodynamics of phase separation in polymer blends is essential for optimizing and achieving desired properties in AM processes that utilize polymer blends.

The formation of a homogeneous polymeric mixture is characterized by a negative free energy of mixing, as described by Equation 10,[64] where ΔG_{mix}, ΔH_{mix}, and ΔS_{mix} are the change in free energy, enthalpy, and entropy of mixing, respectively. T is the temperature. [64]

$$\Delta \boldsymbol{G_{mix}} = \Delta \boldsymbol{H_{mix}} - \boldsymbol{T}\Delta \boldsymbol{S_{mix}} < \mathbf{0} \quad \boldsymbol{Eq.}\,\mathbf{10}$$

The enthalpy of mixing describes the molecular interactions within the mixture, while the entropy of mixing accounts for all possible molecular arrangements.[63] The enthalpy and the entropy of mixing can be expressed in terms of the volume fraction of each component (φ_i) in the blend, as shown in Equations 11 and 12.

$$\Delta \boldsymbol{H_{mix}} = \boldsymbol{\chi_{12} R T \varphi_1 \varphi_2} \quad \boldsymbol{Eq.}\,\mathbf{11}$$

$$\Delta \boldsymbol{S_{mix}} = -\boldsymbol{R}\left[\frac{\boldsymbol{\varphi_1}}{\boldsymbol{N_1}}\ln \boldsymbol{\varphi_1} + \frac{\boldsymbol{\varphi_2}}{\boldsymbol{N_2}}\ln \boldsymbol{\varphi_2}\right] \quad \boldsymbol{Eq.}\,\mathbf{12}$$

In these equations R represents the gas constant, N_i denotes the number of segments or the degree of polymerization of the component, and χ_{12} is the Flory interaction parameter.[63,64] χ_{12} describes the interactions between the components in a binary polymer mixture based on solubility and the energy change associated with the mixing.[63] A large positive value of χ_{12} indicates strong repulsive interactions and immiscibility in polymer mixtures.[64] The value of χ_{12} depends on various factors, including composition and temperature.[64] The entropy of mixing decreases with the size of the mixing entities and diminishes significantly for polymers due to their large size.[63] Consequently, the Gibbs free energy of mixing of polymer blend is mainly determined by the χ_{12} between the blend components.[64] Combining Equations 11 and 12, Equation 10 can be an be rewritten as shown in Equation 13, offering a quantitative method to predict the range of blend compositions where phase separation of the two components will occur as their compositions vary.

$$\frac{\Delta G_{mix}}{RT} = \frac{\varphi_1}{N_1}\ln\varphi_1 + \frac{\varphi_2}{N_2}\ln\varphi_2 + \chi_{12}\varphi_1\varphi_2 < 0 \quad Eq.\,13$$

Polymer Blend Morphology and Glass Transition Temperature

In a completely miscible binary polymer blend, the two components mix at the molecular level, creating a homogeneous mixture.[64] This means no distinct regions exist where one component is present more than the other. The domain size in such a system is on the order of the size of the statistical chain segment, which is a measure of the length of a segment of a polymer chain in which the orientation of the segments is statistically random.[64] In contrast, a completely immiscible polymer blend exhibits complete phase separation due to chemical incompatibility or repulsive interactions between the components.[64]

Determining the glass-transition temperature (T_g) is currently a popular method to test miscibility in polymer blends.[64-66] These DSC studies show that a completely immiscible

polymer blend shows two glass-transition regions for all blend compositions, with the T_gs similar to those of the constituent polymers. In contrast, a completely miscible blend exhibits a single T_g between the T_gs of the individual polymers. The exact T_g of a completely miscible blend can be predicted using various models, including the Fox equation as shown in Equation 14.[65,66] In Equation 14, w_1 and w_2 are the weight fractions of components 1 and 2 with Tg_1 and Tg_2, respectively, and Tg_b is the T_g of the blend.[66]

$$\frac{1}{Tg_b} = \frac{w_1}{Tg_1} + \frac{w_2}{Tg_2} \qquad \boldsymbol{Eq.14}$$

An extensive discussion of the application of the Fox equation in evaluating the miscibility and, thus, the morphology of polycarbonate-polypropylene blended powders for the PBF process is provided in Chapter 4 of this dissertation.

Dissertation Organization and Objective

This dissertation explores how fundamental principles of polymer science can be used to rationally design the molecular characteristics of polymeric feedstocks tailored for powder bed fusion (PBF) and fused filament fabrication (FFF) additive manufacturing techniques. The research presented in this dissertation focuses on understanding and controlling the molecular-level processes of polymer chains during 3D printing to develop materials that achieve stronger layer adhesion and improved mechanical performance in the final printed objects.

Chapter 2 presents a study that uses thermally induced phase separation (TIPS) to incorporate low molecular weight (Mw) polypropylene (PP) additives into high Mw PP powder, aiming to tailor the coalescence dynamics of the resultant powder for the PBF process. The results demonstrate a significant decrease in the zero-shear viscosity of molecular weight blend powders upon the addition of 12 kDa PP. This reduction in viscosity significantly enhances the coalescence rate of the blend powders. The Hopper model is used to understand the mechanisms

that control particle consolidation during the coalescence process. The results also reveal that extensional flow is the primary mechanism driving the coalescence of the fabricated PP powders.

Chapter 3 of this dissertation examines the impact of powder formed from PP Mw blends on the PBF process and the properties of PP-printed components. This Chapter details our effort to create PBF powders with customized Mw distributions, where high Mw PP is blended with an identical but low Mw PP to create molecular weight blends of PP. The material design protocol employed here effectively controls the particle size and size distribution of PP powders for PBF, independent of molecular weight and molecular weight distribution, thereby allowing for a focused investigation of the effects of polymer molecular weight, molecular weight distribution, and zero-shear viscosities on the PBF process. Including smaller polymer chains in the material formulation reduces powder viscosity and enhances coalescence kinetics during printing. Examining the printed parts from these powders shows that blended molecular weight specimens have reduced void space and greater crystallinity than unimodal molecular weight specimens. Dynamic mechanical analysis of the printed parts reveals a substantial increase in storage modulus for the blended molecular weight specimens over their unimodal counterparts. This substantial improvement in the mechanical properties of the blended molecular weight samples is attributed to reduced void volume and enhanced coalescence dynamics facilitated by the powders' reduced melt viscosity.

Chapter 4 of this dissertation offers crucial insights into the impact of polycarbonate (PC) on PP powder properties, presenting opportunities to tune PP printability and broaden the material library for the PBF process. Creating PBF powder that is a blend of polycarbonate and polypropylene using TIPS results in significant changes in the crystallization behavior and crystal structure of the PP in the PP/PC blend particles. Specifically, the lamella thickness of PP is significantly reduced, along with a slight decrease in the degree of crystallinity. These property

modifications will impact volumetric shrinkage and warp deformation, which are major challenges when printing semicrystalline polymers such as PP.

Chapter 5 of this dissertation examines the effects of ultraviolet (UV) light exposure on the structure and properties of PC components produced using fused filament fabrication (FFF). By incorporating a UV-LED optical fiber into the printer head and subjecting the PC to UV light during printing, alterations in the PC's molecular structure occur, including a decrease in molecular weight and modifications in Mw distribution due to chain fragmentation. The study shows that PC components exposed to UV light exhibit significant improvements in both transverse and longitudinal toughness, as well as reduced void spaces, compared to those printed without UV light. These results and GPC analysis leads to the interpretation that chain fragmentation leads to the formation of smaller polymer chains, which facilitates interfilament diffusion and improves interlayer adhesion. This process reduces interlayer voids and improves the overall mechanical performance of the printed components. Chapter 6 summarizes the research, presents the study's conclusions, and suggests potential future works.

Chapter 2: Impact of Polymer Molecular Weight and Dispersity on the Coalescence of Polypropylene Powders Suitable for Laser Powder Bed Fusion

A version of this chapter was published by Akan A. George and Mark D. Dadmun: George, A. A.; Dadmun, M. D. "Impact of polymer molecular weight and dispersity on the coalescence of polypropylene powders suitable for laser powder bed fusion." *Polymer*, **2024**, 312, 127663, 10.1016/j.polymer.2024.127663

Abstract

Understanding and controlling the fundamental processes governing the coalescence of polymers is vital to enabling the design of polymeric materials for improved mechanical performance and quality of manufactured structures, including those fabricated via additive manufacturing techniques. Our group has utilized thermally induced phase separation (TIPS) to produce spherical and size controlled polypropylene (PP) powders from 12,000 (12k), 250,000 (250k), and 340,000 (340k) molecular weight (Mw) PP, including 50-50 wt.% blends of 12k/250k,12k/340k, and 250k/340k, and a 33-33-33 wt.% blend of 12k/250k/340k to investigate the impact of polymer Mw, and thus zero-shear viscosity, on particle coalescence and its implication in laser powder bed fusion. The particles exhibit similar size distributions with an average particle size, Dx(50), in the range of 58 μm -86 μm. The coalescence behavior of the powders, evaluated via hot-stage microscopy, shows that adding 12k PP in the blend significantly alters the coalescence dynamics of the 250k and 340k PP, dramatically increasing their coalescence rate. The substantial drop in zero-shear viscosity with addition of 12k PP provides the driving force for the pronounced enhancement in coalescence. Strong agreement between experimental results and the Hopper model of coalescence is observed, assuming correction for extensional flow, exemplifying the importance of extensional flow on the coalescence process. The results also indicate that the 12k PP in the blend does not surface segregate in the TIPS process, but is homogeneously distributed in the blend. More broadly, these results provide molecular-level insight into how control of powder molecular weight characteristics and

viscosity can offer pathways to optimize the consolidation of particles in manufacturing processes, including laser powder bed fusion.

Introduction

The process of polymer coalescence is fundamental to understanding the consolidation mechanism of parts created using several manufacturing processing technologies, including laser powder bed fusion (LPBF) 3D printing techniques.[22,32,33] Coalescence, also known as sintering, refers to the process by which two or more particles merge into a single homogenous body.[44,67] Throughout this paper, coalescence and sintering will be used interchangeably. The coalescence of polymeric particles begins with elastic adhesive contact between the particles to form a neck. This neck then grows progressively until the coalescing particles form a single homogenous melt. Neck growth occurs via two modes. The first mode is the zipping mode, driven by adhesive intersurface forces, and the second mode is the stretching mode, driven by curvature-based surface tension forces.[32,38,39] The transition from the initial elastic contact to the neck growth mode is viscoelastic and depends on the particle radius.[38] Schematically, these modes are illustrated in **Figure 5**.[38] Fundamentally, the minimization of surface energy is the driving force for coalescence, where the surface tension and viscosity of the polymer are critical properties influencing the coalescence process. Several models, including the Frenkel and the Hopper models, have been developed to provide a fundamental correlation of the physical properties of the polymer to coalescence process, monitored by the time dependence of the change in neck growth and droplet radius. By equating the work done by surface tension to the energy dissipation due to viscous flow, Frenkel predicted that the neck radius, y, of two

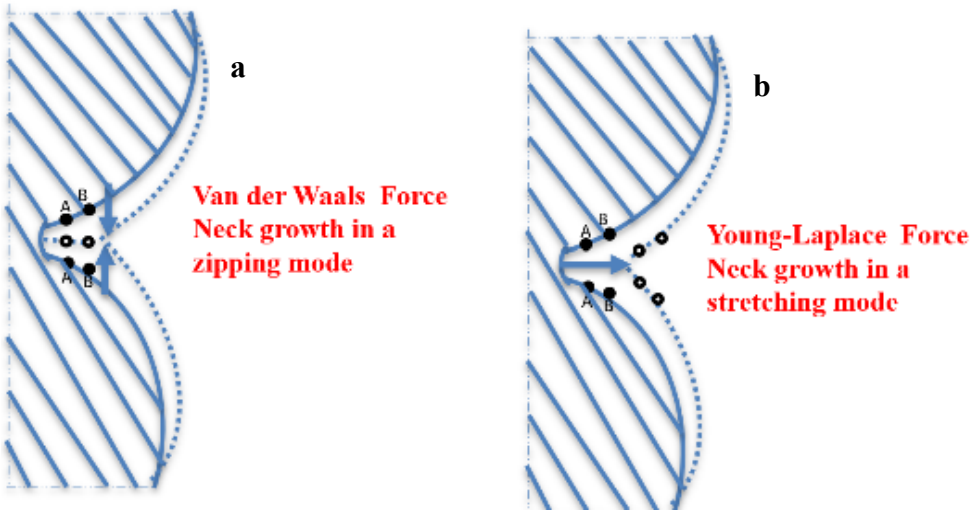

Figure 5. Schematic illustration of contact growth modes. (a) Elastic contact in a zipping mode dominated by van der Waals attraction forces. (b) Contact growth in a stretching mode dominated by curvature-based tractions.

coalescing spheres varies with sintering time, t,as $t^{1/2}$, as shown in the following Equation:[39]

$$\frac{y}{a_0} = \left(\frac{3\Gamma t}{2a_0\eta_0}\right)^{\frac{1}{2}}$$

, where a_0 is the initial particle radius, and Γ and η_0 are the surface tension and zero-shear viscosity of the polymer, respectively.[22,68] A schematic illustration of the coalescence of two spherical particles based on the Frenkel model is shown in **Figure 6**.[32] The Frenkel model assumes that the particle radius is relatively constant throughout the coalescence process. It should be noted that the Frenkel model is based on small angle changes, which corresponds to short annealing times when the particle radius is relatively constant and may not be applicable for long times of coalescence as the neck growth (y/a_0) approaches 1.[22,44]

The Hopper model for droplet coalescence is based on the exact analytical solution of the Navier–Stokes equation for two-dimensional viscous flow driven by capillary forces.[68,69] By analyzing the capillary flow for two equal cylinders having an inverse ellipse as their cross section, Hopper presented a coalescence model summarized in the following Equations: [68,69]

$$\frac{y}{a_f} = (1-\alpha)(1+\alpha^2)^{-\frac{1}{2}}$$

$$\frac{\Gamma t}{a_f \eta_0} = \frac{\pi}{4} \int_{\alpha^2}^{1} \left[\beta(1+\beta)^{\frac{1}{2}} K(\beta)\right]^{-1} d\beta$$

, where y, a_f, Γ, η_0 t, α, are the neck radius, final particle radius, surface tension of the polymer, zero-shear viscosity of the polymer, sintering time, and inverse ellipse parameter, respectively. When α =0, the droplet perimeter is one circle; as α approaches 1, the droplet perimeter approaches the shape of two circles. $K(\beta)$ is a complete elliptic integral defined as follow:

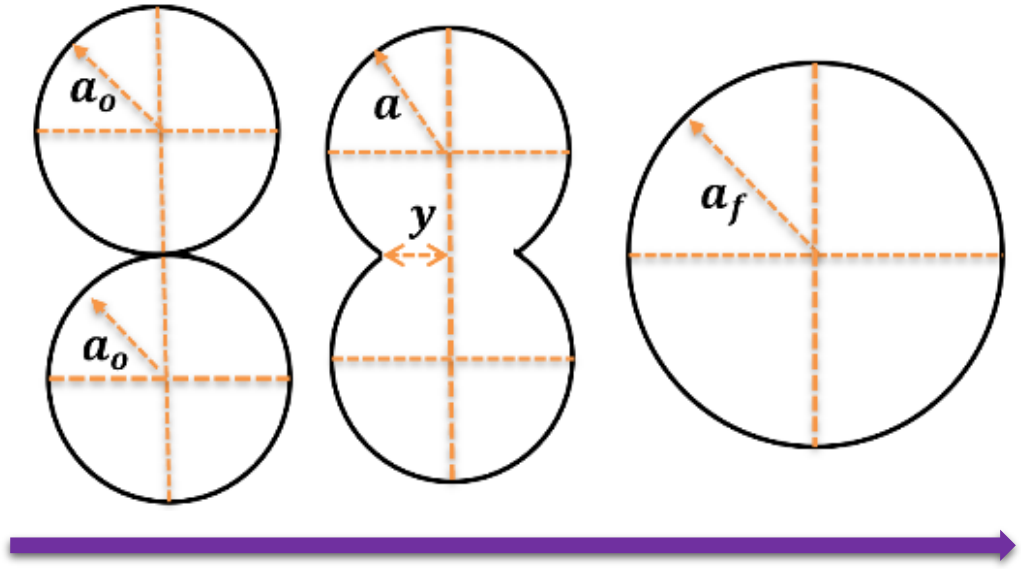

Figure 6. Schematic illustration of coalescence of two spherical particles based on the Frenkel model. At t=0, a_0, is the initial particle radius. At t > 0, the particle radii are denoted by a and a_f, where a_f is the final particle radius, while y is the neck radius.

$$K(\beta) = \int_0^1 [(1-\epsilon^2)(1-\beta\alpha^2)]^{-\frac{1}{2}} d\epsilon$$

, where ϵ is the parameter of the elliptic integral that ranges between 0 to 1.[68]

Bellehumeur et al. compared the experimental time dependence of the coalescence of different grades of polyethylene droplets to both the Frankel and the Hopper models.[68] The authors concluded that the Hopper model predictions agree well with the experimental data, but the Frankel model predictions significantly deviate from the experimental data, especially at longer coalescence times. The reason for the deviation of the experimental data from the Frenkel model is attributed to the assumption in the Frankel model that the particle radius is constant throughout the coalescence process. Such an assumption is satisfactory only when the neck growth is less than 0.3. On the other hand, the Hopper model considers the change in particle radius as the coalescence progresses.[68,69]

The extent of neck growth dominates the strength of a coalesced material; significant neck growth will result in an appreciable increase in strength and densification.[70,71] In the initial stage of coalescence, the extent of neck growth corresponds to $\lesssim 0.33$, and this stage is associated with significant void space present in the coalesced structure and no densification. The intermediate stage of coalescence corresponds to ~ 0.5 neck growth. In the final stage, also known as the late state of coalescence, the particles form a densified network, and at this stage, there is a significant reduction of void space in the coalesced structure.[72,73] Under the same coalescence conditions, a particle with higher Mw, thus higher viscosity, will exhibit a slower coalescence rate, which could lead to limited neck growth relative to that of a particle with lower Mw. In LPBF, the formation of substantial neck growth is needed to significantly reduce void space, thus improving the strength of the printed part.

Hot-stage microscopy (HSM) is a valuable tool to monitor the process of polymer

coalescence.[21] Some researchers have used HSM to study how temperature and heating rate impact droplet coalescence kinetics and to link these experimental conditions to the coalescence mechanism involved in the process of LPBF 3D printing. For example, Zhao et al. studied the coalescence of polyamide 12 powder, where the experiment was performed at different heating rates between 1°C/min - 150°C/min to identify the onset coalescence temperature. The authors also performed the coalescence experiment at 192℃ and 195℃ to monitor how neck growth changes with temperature. The results showed that the onset coalescence temperature increases as the heating rate increases and neck growth increases as the temperature increases.[74] In another experiment, Berretta et al. first heated poly (ether ether ketone) powder particles from room temperature to 400℃ at 120℃/min to identify the onset coalescence temperature, and then the experiment was repeated, where the powder particles were heated from room temperature up to 400℃ at 120 ℃/min and held at this temperature for 2 min to best approximate the layer formation time for this material in LPBF 3D printing.[75] In both Zhao et al. and Berretta et al. works, the HSM experiment was designed to identify the experimental conditions that mimic the conditions in LPBF 3D printing. It should be noted that the obtainable thermal history in HSM is not comparable to the thermal history involved in LPBF 3D printing. In fact, Laumer et al. reported that the heating rates involved in the laser sintering process of PA could reach values of 10^7 K/min.[76] Such a high heating rate is nearly impossible to achieve in HSM.

This work seeks to understand how polymer feedstock molecular design, rather than temperature and heating rate, impact droplet coalescence dynamics and provide molecular level insight to enable the development of polymeric feedstocks to improve and understand LPBF 3D printing. The polymer properties such as particle size, particle shape, and viscosity are critical factors that determine the success of the coalescence process involved in LPBF.

Appropriate particle size is essential for efficient flowability, energy absorption, and the formation of appreciable neck growth during the printing process. Thermodynamically, the driving force for the coalescence of two particles is the reduction of surface energy, which increases with decreasing particle size.[77,78] Both the Frenkel and the Hopper coalescence models qualitatively predict that an increase in particle size will slow down the coalescence rate, as increasing the particle size reduces the driving force arising from the surface tension.[68,79] Slower coalescence kinetics can lead to incomplete neck growth.[79] For example, the results provided by Hejmady et al., showed that 105 μm polystyrene (PS) particles coalesced to ~ 0.47 neck growth, whereas 30 μm PS particles coalesced to a neck growth of ~ 1 at the end of the coalescence process and under the same experimental conditions. The partial neck growth exhibited by the larger PS particle results in excess porosity in the printed parts formed by powder bed fusion.[79] These, and other considerations, lead to a recommended average particle size of 40-100 μm for powder bed fusion.[80]

Void space and mechanical properties of structures printed via LPBF are strongly influenced by the development of interparticle contacts and interparticle adhesion during the printing process.[81] Unlike the injection molding process, no mechanical pressure is applied during the LPBF process. Thus, evolution of structure in LPBF depends intimately on the zero shear viscosity of the material for the efficient densification and coalescence of particles during the printing process. Thus, the viscosity of the polymeric feedstocks for the LPBF process must be low enough to flow and facilitate interparticle adhesion during the coalescence process. Therefore, the aim of the study is to examine the impact of designing and controlling the molecular weight characteristics, and thus viscous properties, of polypropylene (PP) powders on coalescence dynamics. PP is an important thermoplastic that is used in a wide range of applications due to its good mechanical performance, chemical stability, and relatively low

cost.[82]

As shown in the Frenkel and Hopper sintering models, zero-shear viscosity is a crucial parameter that influences the coalescence process, whereby the coalescence rate decreases as the zero-shear viscosity increases. The relationship between the zero-shear viscosity of the polymer (η_0) and the molecular weight of the polymer (Mw) is given as follow:

$$\boldsymbol{\eta_0 = k\, Mw^{3.4}}$$

, where k is a constant. [43]

Given this relationship and fundamental understanding, this study is designed to address some fundamental questions: How robust are the Frenkel or the Hopper sintering models in describing the coalescence behavior of multicomponent powders? What fundamental driving forces control the Mw dependence on the coalescence process? Can the coalescence dynamics of high Mw materials be enhanced by tuning the molecular design of the powder?

To address these questions, the coalescences of particles made from Mw blends are evaluated by HSM and compared to the coalescence behavior of unimodal Mw polymer powders. By blending low Mw and high Mw polymers to form Mw blend powders, a reduction in the shear viscosity of the resulting polymer blend powder relative to the neat high Mw powder is anticipated. This reduction in viscosity should enhance powder coalescence during sintering relative to that of powders composed solely of unimodal Mw polymer, as shown in **Figure 7**. Thus, under the same experimental condition, we expect powder formed from blends of high and low molecular weight polymers to more readily coalesce within a short time than the powder formed from neat high molecular weight polymer. Providing this level of insight into the molecular level processes that control particle coalescence affords a foundation to rationally

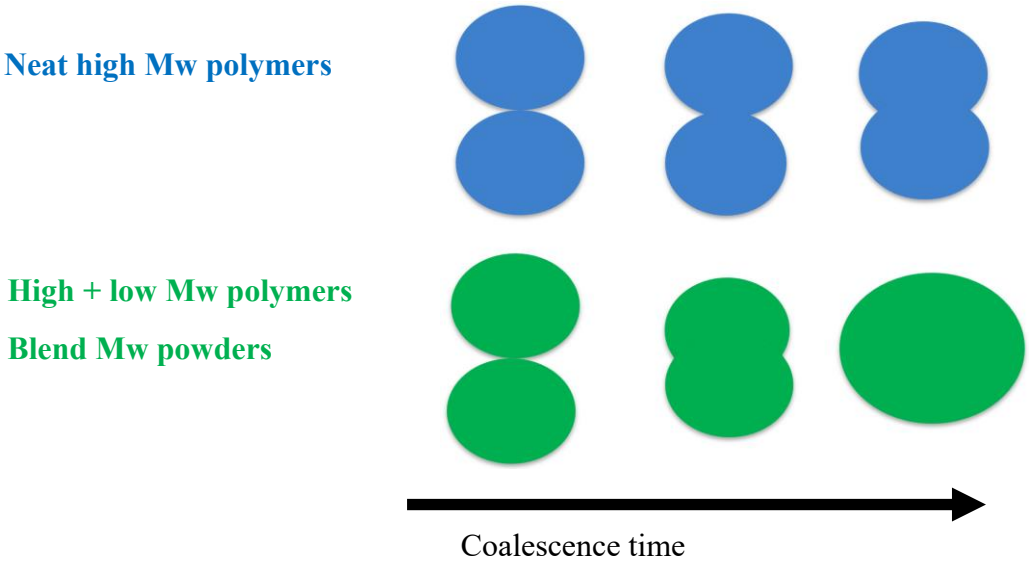

Figure 7. Proposed scheme to enhance coalescence of high Mw polymer by tuning the molecular design of the powder. Under identical experimental conditions, Mw blend powders with low molecular weight polymer should exhibit faster coalescence than unimodal powders.

design polymeric materials for optimal performance in LPBF printing. Furthermore, creating blended Mw powders offers an economical and efficient route to design feedstocks to address current challenges in the LPBF process.

Experimental

Materials

Pellets of isotactic polypropylene (PP) with weight average molecular weight of 12,000 (12k), 250,000 (250k), and 340,000 (340k) g/mol were acquired from Sigma-Aldrich. Silicone oil, xylene, and ethanol were obtained from Fisher Scientific. All chemicals were utilized without additional purification.

Preparation of PP microspheres by thermally induced phase separation (TIPS)

Thermally induced phase separation (TIPS), also known as liquid-liquid phase separation,[13,15,27] was employed to prepare PP microspheres for the coalescence study. TIPS involves the dissolution of a polymer in a suitable solvent at an elevated temperature, followed by cooling the polymer-solvent system below the binodal line, as shown in **Figure 8**,[15] to induce phase separation of the polymer from the solution to form microspheres. TIPS is a facile technique that does not require complex equipment, and the solvents used can easily be recovered and reused. Additionally, spherical microspheres with smooth surface morphologies are easily obtained, and experimental conditions such as polymer concentration and quench temperature can be tuned to control the particle size of the formed powders.[13,15]

Using this method, PP powders were prepared from the pellets of PP with molecular weights of 12k, 250k, and 340k, as well as from 50-50 wt.% blends of 12k/250k, 12k/340k, and 250k/340k and a 33-33-33 wt.% blend of 12k/250k/340k. For every PP sample formulation, 9g of PP pellets and 91g of xylene were placed into a 250 ml round bottom flask, heated to 190 °C,

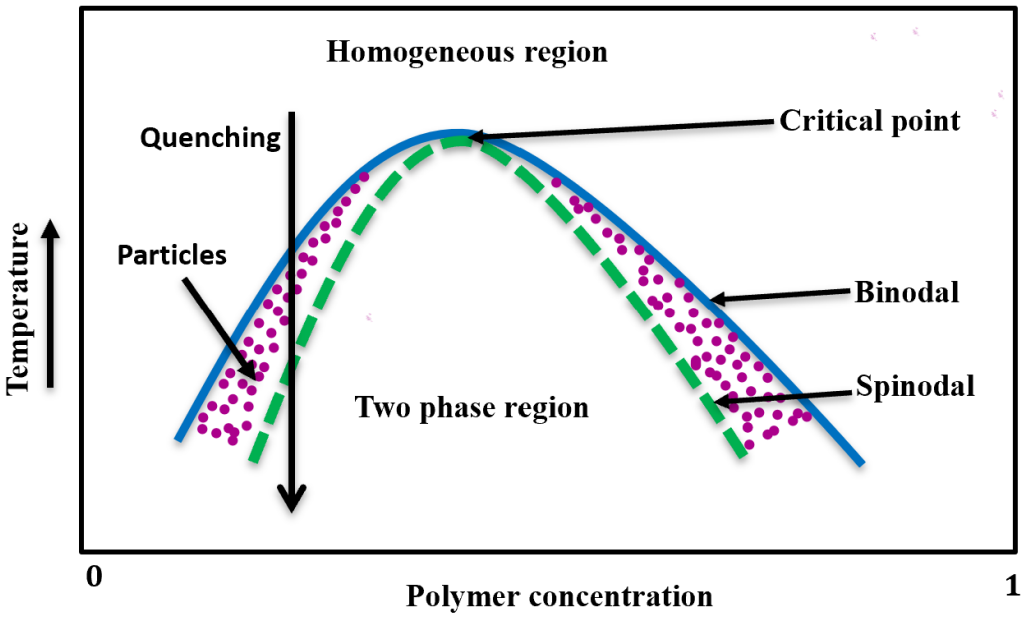

Figure 8. Scheme for formation of powder by TIPS. Polymers precipitate during a thermal quench below the binodal.

and refluxed for 1 hour stirring at 200 rpm, to form a homogeneous solution. After 1 hour of refluxing, the mixture was placed into a cold trap at 40 °C and equilibrated for 1 hour to precipitate the powder. The cold trap was set up using a Fischer Isotemp, with a refrigerant mixture of 50% water and 50% ethylene glycol. Vacuum filtration was performed for five minutes to separate the precipitate, and the resulting PP microspheres were washed with ethanol three times to eliminate residual xylene. The obtained powders were further placed in a vacuum oven at 40°C and left to dry for 24 hours to remove entrapped solvent. Throughout the drying process, the mass of the powder was monitored by every 6 hours. After 6 hours of drying, the mass of the powder remained unchanged with further drying, verifying the removal of entrapped solvents in the powder.

Laser diffraction particle sizing of powders prepared by TIPS

The particle size and distribution of the prepared PP powder was determined with a Mastersizer 3000 laser diffraction particle size analyzer, Malvern Instruments Ltd. The dry dispersion method dispersed the dried PP samples by accelerating particles through a venturi tube using compressed air. Each measurement was conducted with both blue LED and red laser lights for 10 seconds, providing the particle size distribution and median diameter, Dx(50), for all the prepared PP powder samples.

Particle shape analysis of powders prepared by TIPS

The shape of the powders was observed using scanning electron microscopy (SEM), a ZEISS-EVO. The SEM ZEISS-EVO instrument was operated with a high electron tension set at 20.00kV. Prior to imaging the powders, they were coated with a thin layer of gold to mitigate surface charging. The samples were imaged at a magnification ranging from ~ 500X to 800X, with a working distance varying from 8.5 mm to 14.5 mm.

Zero-shear viscosity of powders prepared by TIPS

Rotational rheometry was employed to measure the zero-shear viscosities of the pure PP and Mw blend powders prepared by the TIPS process. An AR200ex rheometer from TA Instruments at Oak Ridge National Laboratory was used for this measurement The viscosity was measured at 164 ℃ with a shear rate of 0.1 s^{-1}. Disc-shaped specimens, 25 mm in diameter and 1 mm thick, were prepared via compression molding. A 25mm diameter parallel plate was utilized for the measurement. Prior to each rheological measurement of a sample, a 10-minute thermal stabilization period was implemented to attain thermal equilibrium. Throughout all measurements, the temperature was maintained within a 0.2 K range.

Polypropylene Molecular weight of powders prepared by TIPS

A high-temperature Size Exclusion Chromatography was utilized to determine the molecular weight characteristics of the PP powder formed by the TIPS process. A Malvern high-temperature OMNISEC system was used for this analysis, with 1,2,4 trichlorobenzene used as the eluent and 1.0-3 mg/ml solution concentrations. Instrument calibration was conducted employing PP standards. Viscometer, refractive index, low-angle light scattering, and right-angle light scattering were used as detectors to determine the molecular weight characteristics of the PP powders, including number average molecular weight, weight average molecular weight, and dispersity.

In situ monitoring of particle coalescence via hot-stage microscopy

To monitor the rate of particle coalescence of the PP powders, PP microspheres were deposited on microscopic glass slides and placed on a Mettler FP82HT hot stage. The time development of the particle coalescence in the hot stage was then viewed at 164℃ with a BH-2 Olympus microscope at a magnification of 200x. Videos of the coalescence were recorded and analyzed to monitor the change in neck radius (y) and radii of the two coalescing PP particles

(a_f) as a function of coalescence time (t) with ImageJ software. Before each measurement, a micrometer calibration slide was observed in the microscope to calibrate the image length scale at the chosen magnification. The data presented represent the average of the measurement of the coalescence of 3-5 droplet pairs for each material formulation.

Printing of the prepared TIPS powders by laser powder bed fusion

Tensile bars and rectangular specimens were printed from each of the powders prepared by TIPS using a Prodways Promaker P2000 HT printer machine. The laser power, beam velocity, and hatch spacing in the printing process were 50 W, 3750 mm/s, and 0.3 mm, respectively. Throughout the printing process, the bed and feed temperatures were maintained at 140 °C. These processing parameters remained constant across all printed samples. The printed multi-layer tensile and rectangular structures printed from the prepared powder are shown in **Figure 9**.

Results and Discussion

Particle size of PP powders obtained via laser diffraction

In these studies, the formation of polypropylene powders that are suitable for powder bed fusion was targeted. Previous studies in our group [13,15] show that forming powder from 9 wt.% PP solutions in xylene that are quenched to 40 °C produces powders that are between 50 and 100 μm and tend to be spherical. **Figure 10** presents the average size and size distribution of the PP powders formed from the 12k, 250k, and 340k pellets, as well as for the molecular weight blends (50-50 12k/250k, 50-50 12k/340k, 50-50 250k/340k, and 33-33-33 12k/250k/340k). For all sample formulations, the particles demonstrate similar size distribution, as shown in **Figure 10b**. As shown in **Figure 10a**, the particles exhibit average particle size, Dx(50), in the range of 58-86

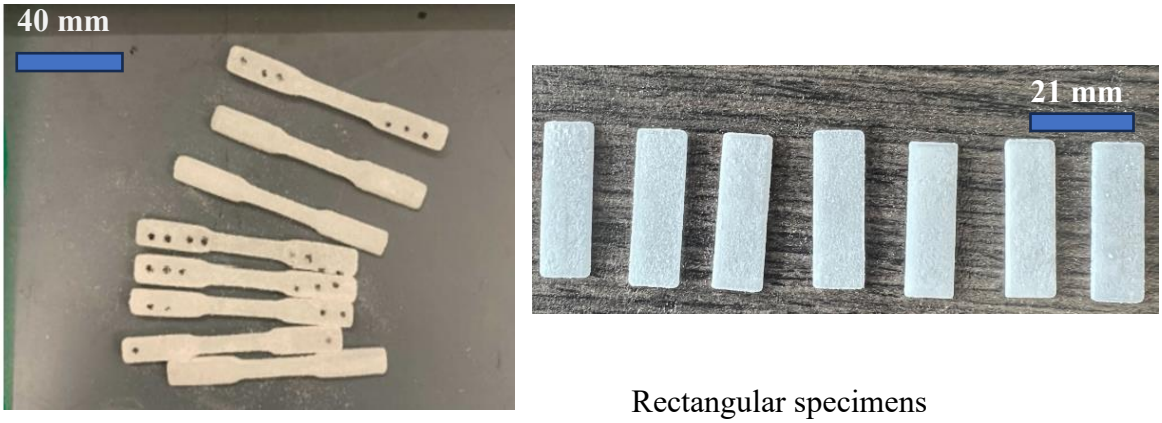

Tensile bars/Dogbone specimens

Rectangular specimens

Figure 9. Printed structures from polypropylene powders prepared by the TIPS process. The black dots on the tensile bar serve as markers for specimen identification and are not a result of processing artifacts.

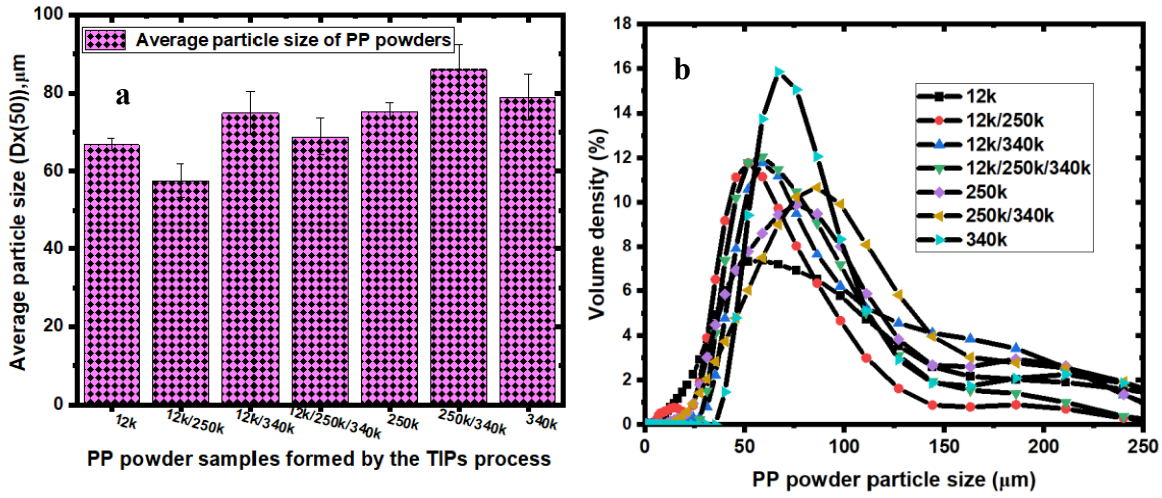

Figure 10. Average particle size (a) and size distributions (b) of the PP powders formed by the TIPS process.

μm, which is within the recommended average particle size range for powder bed fusion.[80] As shown in **Figure 9**, these powders have been utilized to create structures by powder bed fusion. The properties of the printed structures will be correlated to coalescence studies, where these results will be reported in a future publication. While the coalescence process was meticulously monitored for two specific droplets, it is imperative to note that the coalescence was performed across seven sample formations, each comprising hundreds of particles. Consequently, presenting the average particle size for every powder sample in this study offers a more representative and reliable measure of the particle size, ensuring a more thorough understanding of the particle size characteristics for all sample formulations. Fascinatingly, there is a subtle variation in average particle size across different material formulations, providing an opportunity to focus solely on exploring how molecular weight of the powders affects the coalescence process. More importantly, the formation of these PP powders with similar size and size distributions provides a foundation to eliminate the influence of particle size on the coalescence mechanism in this study.

Powder Shape

The shape of the powders prepared by the TIPS process was determined by electron microscopy, as it is well known that spherical powder offers the required flowability and packing for a successful powder bed fusion print. **Figure 11** shows the structure of the polypropylene powders, where most of the PP particles exhibit spherical shapes with smooth surfaces and some resemble ellipsoids. Some collapsed particles are observed in the neat 12k powder, and some particles in the neat 340k exhibit surface coarseness. Interestingly, blending 12k with high Mw PP in solution eliminates particle collapse in the resultant powder that is observed in the powder formed from the neat 12k and surface coarseness observed in the powder formed from the neat 340k. This change in morphology could be due to the thermodynamics of the phase separation

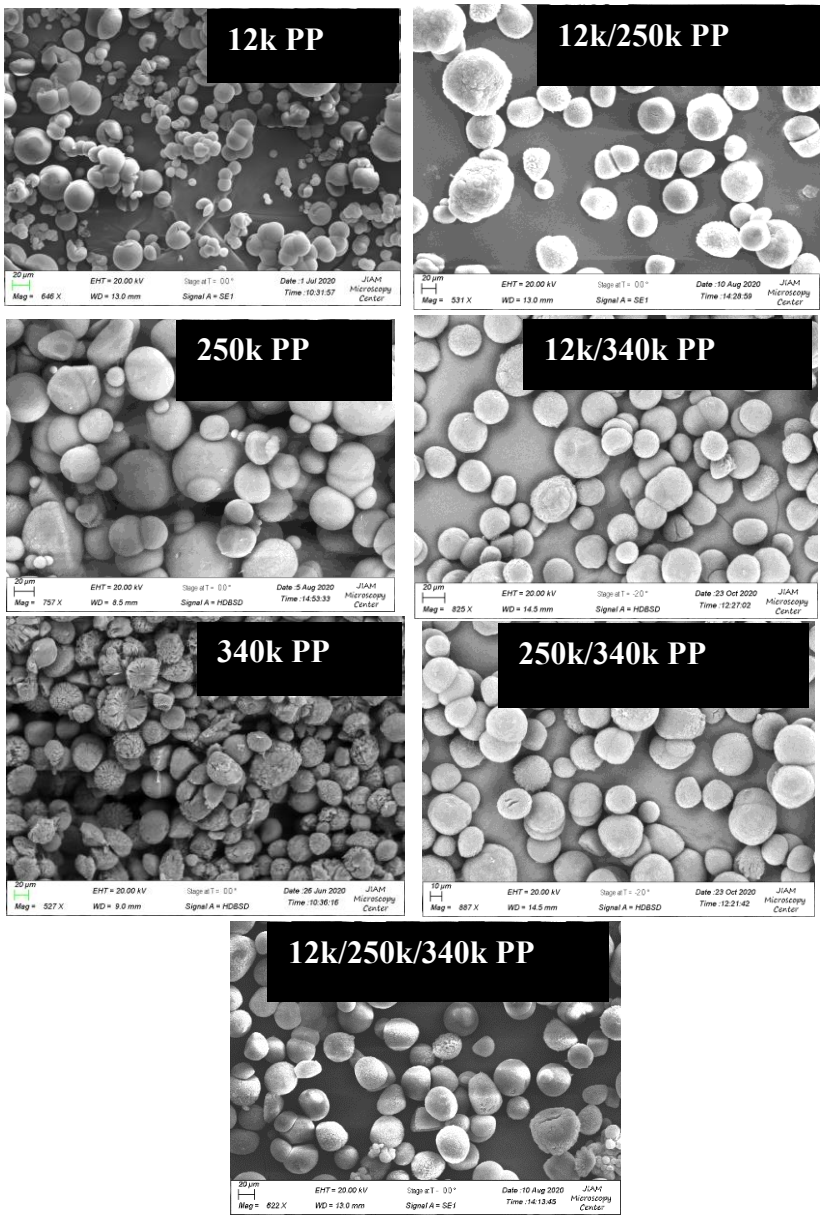

Figure 11. Scanning electron micrographs of PP powders formed from the TIPS process. Scale bars are included at the bottom of the image.

processes in TIPS. More importantly, the production of PP microspheres with similar shapes provides a foundation to eliminate the influence of particle shape on the coalescence process in this study.

Zero-shear viscosity and molecular weight of powders prepared by TIPS

The formation of PP particles with systematic variations in zero-shear viscosities provides the foundation needed to examine the quantitative dependence of particle coalescence rates to viscosity. Thus, the zero-shear viscosities of the powders formed from neat polymers and their blends by the TIPS process were measured and are reported in **Figure 12**. **Table 1** reports the molecular weight characteristics of the PP powders. It is well known that the molecular weight and dispersity of the polymer impact the zero-shear viscosity of the polymer.[83,84] Inspection of **Figure 12** shows that the viscosities of these samples range from 1.2-7000 Pa·s. As anticipated, there is a clear correlation between higher molecular weight and increased viscosity in the polymer. Not surprisingly, the addition of 12k polypropylene to the other, higher molecular weight polypropylene significantly decreases the zero-shear viscosity and broadens the dispersity, Mw/Mn, of the powders.

In situ monitoring of particle coalescence via hot-stage microscopy

Effect of zero-shear viscosity on particle coalescence

The impact of rationally varying the molecular weight characteristics of the polypropylene by blending different chain lengths on the particle coalescence process was monitored with hot stage microscopy. **Figure 13** offers a qualitative picture of the impact of varying the molecular weight characteristics of the polymer by blending polymer with different chain lengths, showing the extent of coalescence of PP powders after 3 seconds of the powder formed from the 12k PP, from the 250k PP, and the 50-50 blend of 12k/250k PP. The coalescence of the 12k sample is essentially complete, while the 50-50 blend shows significant neck growth,

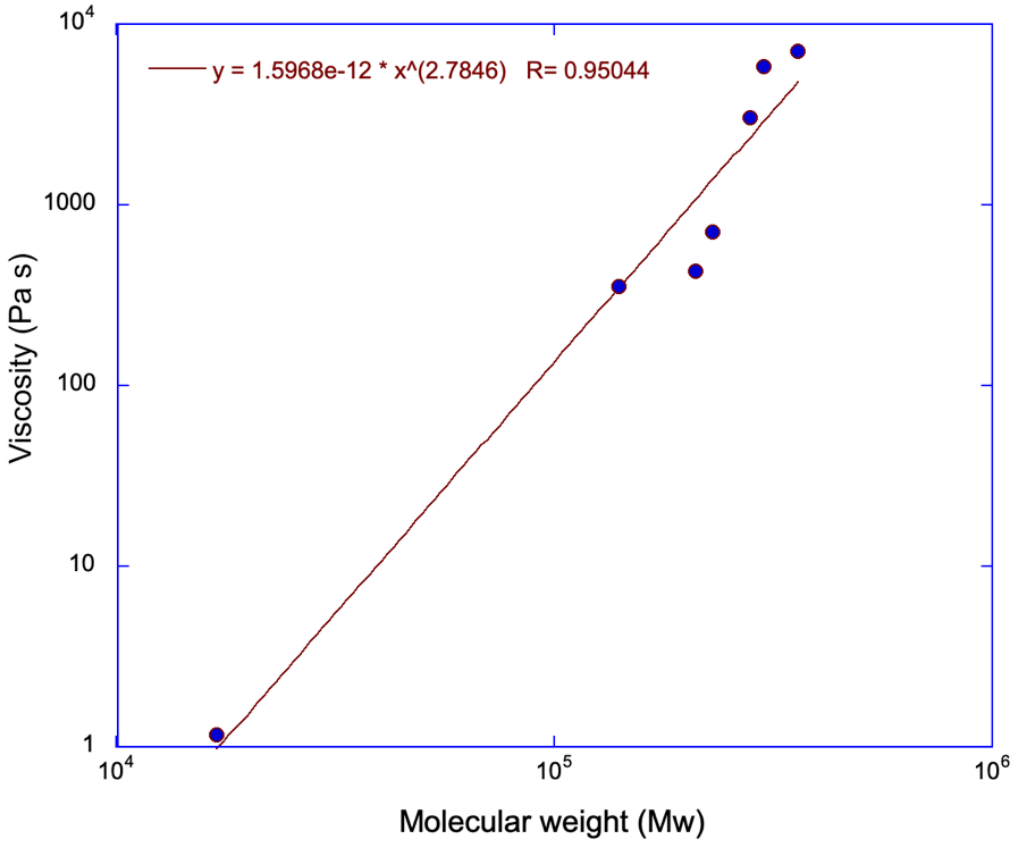

Figure 12. Zero shear viscosities of PP powders prepared by TIPS as determined via rotational rheometry at 164°C.

Table 1. Nomenclature and molecular weight characteristics of PP powders formed by the TIPS process.

Nomenclature of polymers used in the TIPS process	Molecular weight of PP powders formed by the TIPS process		
	Mn (1×10^3)	Mw (1×10^3)	Mw/Mn
12k	8.1	17	2.1
250k	130	280	2.2
340k	130	360	2.8
12k/250k (50-50)	24	140	5.8
12k/340k (50-50)	33	210	6.4
250k/340k (50-50)	130	300	2.3
12k/250k/340k (33-33-33)	17	230	14

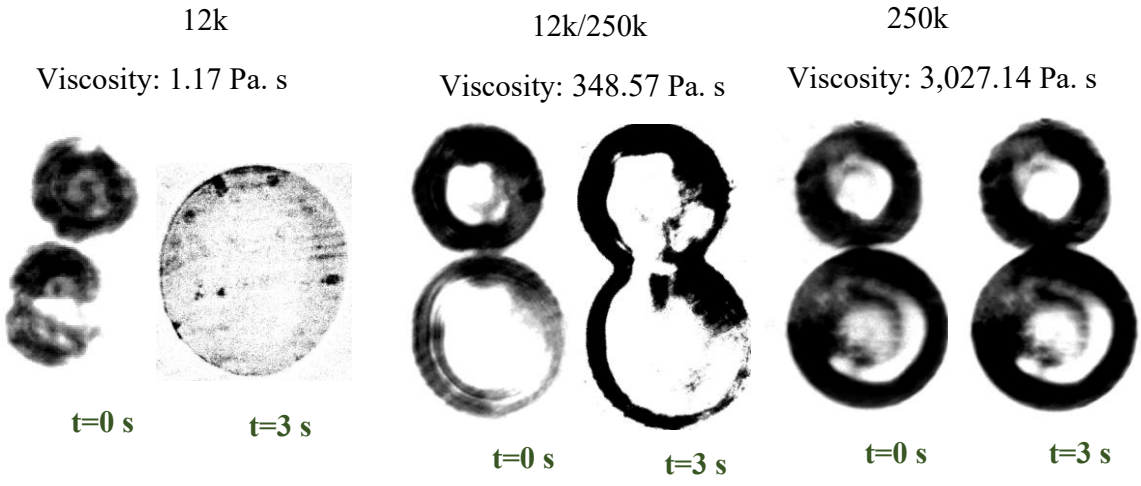

Figure 13. Structural evolution of PP powder during coalescence of two droplets.

and the 250k sample has barely formed the neck. As expected, the PP powders with lower zero-shear viscosity attains higher levels of coalescence within a short time than powders with higher zero shear viscosity. To more fully understand the impact of the molecular design of these powders on the PBF process, correlating the mechanical properties of parts printed from these PP powders to the examined coalescence process is currently underway.

Application of coalescence models to the coalescence of PP: Frenkel vs. Hopper model

As noted in the introductory section, the Frenkel model assumes a constant particle radius and is only valid in the initial coalescence stage. In contrast, the Hopper model assumes a change in particle radius during coalescence and is valid both in the initial and late stages of coalescence. Inspection of the structural evolution shows that the average particle radii of two coalescing particles varies significantly during the coalescence process, and thus the Hopper model is used to model the PP coalescence behavior, as discussed below quantitatively.

Quantification of neck growth and coalescence rate

Figure 14 shows the coalescence of two droplets of PP powder and illustrates how the growth of the neck (y/a_f) with coalescence time (t) growth is determined. **Figure 15** shows the growth of the neck in the PP powders as a function of coalescence time for all powders.

As shown in **Figure 15**, the timescales to reach full coalescence ($y/a_f \rightarrow 1$) vary significantly with changes in molecular weight, where PP samples with higher Mw and viscosities take longer to coalesce. For example, it takes 47 and 91 seconds for y/a_f to reach 0.8 for the 250k and 340k samples, respectively. Interestingly, the addition of 12k Mw to the blend significantly enhances the coalescence dynamics of the 250k and 340k samples; it only takes 4 and 8 seconds for the dimensionless neck (y/a_f) of the 12k/250k and 12k/340k powder to reach 0.8. These results show that the rate of particle coalescence of high Mw materials can be enhanced by tuning the

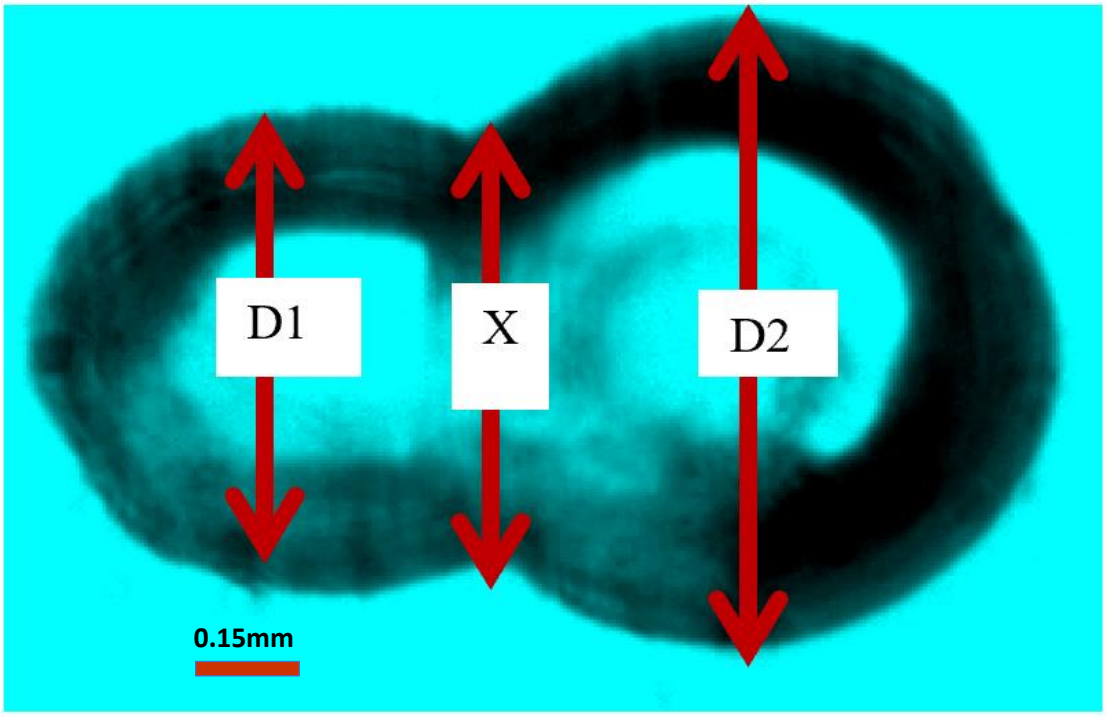

Figure 14. Coalescence of two droplets of PP powder. D1 and D2 are the diameters of droplet 1 and droplet 2, respectively. Average particle diameter (D) = $^{(D1 + D2)}/_{2}$. Particle radius (a_f) = $^{D}/_{2}$. Particle neck diameter =X. Particle neck radius (y)=X/2. y/a_f=neck growth= dimensionless neck radius

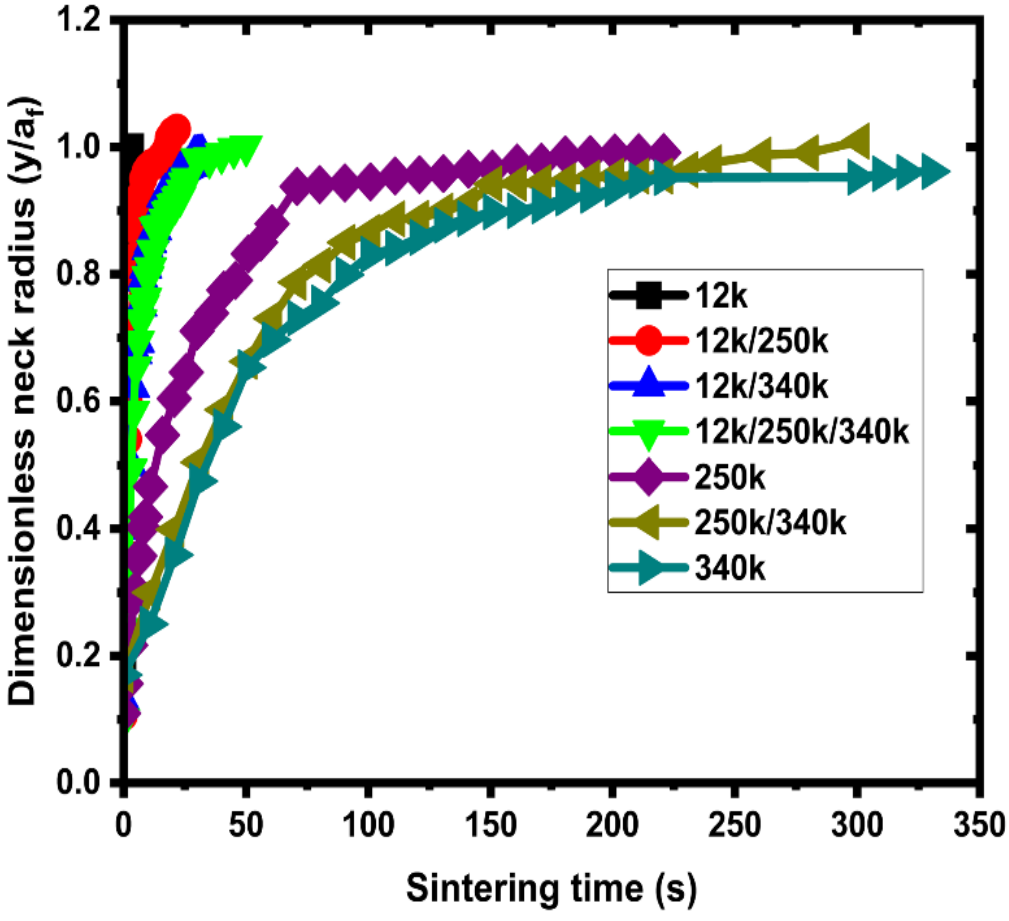

Figure 15. Neck growth of the PP powders as a function of sintering time.

molecular design of the powders by the addition of lower molecular weight polymer chains to the sample.

Fitting coalescence data to the Hopper model

To critically examine the ability of the Hopper model to model the coalescence behavior of these multi-component powders, as well as provide insight into the molecular-level processes that control the consolidation of particles during coalescence of multicomponent samples and understand the fundamental driving forces that control Mw dependence on the coalescence process, the coalescence data was fit to the Hopper coalescence model with no adjustable parameters. To fit the data to the Hopper model, the surface tension of PP must be known. Literature reports estimate that the surface tension of PP is between 0.026 - 0.034 N/m.[41,85] Thus, the experimental data was fit to the Hopper model using the measured zero-shear viscosities, shown in **Figure 12**, and a surface tension (Γ) of 0.03 N/m. **Figure 16** presents the experimental data and the estimate of the coalescence via the Hopper model. It is interesting that the shape of the Hopper model is similar to the experimental data, however, the Hopper model overestimates the rate of coalescence. Inspection of the data and the Hopper model shows that the Hopper model is ~7× and ~278× too fast in estimating the coalescence rates in **Figure 16a** and **Figure 16b**, respectively.

Further investigation in the literature shows that the flow that occurs during the coalescence process is not shear flow, but is extensional flow.[33,44] In fact, Verdier and Brizard[45] clearly visualize the extensional flow of the polymer during droplet coalescence. Thus, we believe that the extensional viscosity of the powders must be used in the Hopper model, rather than the shear viscosity. Fortunately, the extensional viscosity of a polymer, η_e, is related to its shear viscosity via the Trouton ratio, as shown in following Equation:[43]

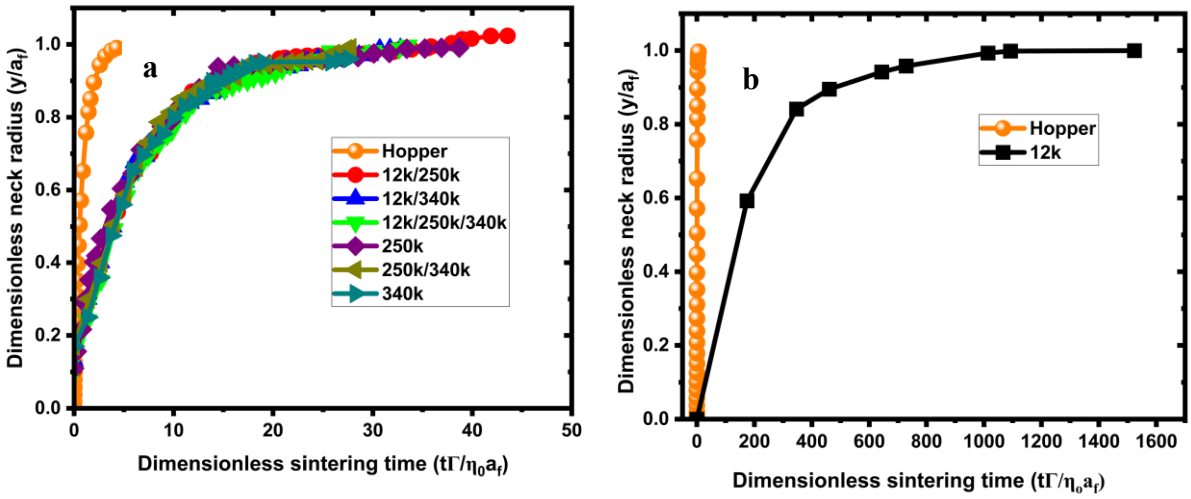

Figure 16. Comparing PP experimental coalescence data to Hopper model using shear viscosity of PP powder. (a) High Mw and blend. (b) 12k Mw.

$$\boldsymbol{Trouton\ ratio} = \frac{\eta_e}{\eta_0}$$

The Trouton ratio varies from ~3-10 for polymers dependent on a number of factors including the extensional shear rate, where a value of 3 is often offered for the Trouton ratio at low shear rate.[43] However, White et al. have measured the extensional viscosity and Trouton ratio of PP and report values of 6-10 at low Weissenberg number.[86] Thus, this data provides a quantitative method to estimate the extensional viscosity of our samples, $\eta_e = \eta_0 \times 7$. Therefore, to account for extensional flow, the shear viscosity in the Hopper Equation is replaced with the extensional viscosity. With this correction, the coalescence data were plotted with the Hopper model using the extensional viscosity with no adjustable parameters to obtain the data in **Figure 17**. Inspection of **Figure 17a** shows strong agreement between the experimental coalescence data of the 250k, 340k, and blend particles with the Hopper model that accounts for extensional flow. Surprisingly, the coalescence data of the 12k particles still significantly deviates from the Hopper model that accounts for extensional flow, where the Hopper model significantly overestimates the coalescence rate of the 12k powder even when accounting for the extensional flow of the polymer.

Inspection of the Hopper coalescence model shows that the Hopper model is also strongly dependent on the surface tension of the polymer, thus it may be that this discrepancy is because the surface tension of the 12k PP, which is the smallest chain length studied, differs significantly from that of the other polymers. In fact, it is well-known that the surface tension of a polymer depends on the Mw, where the contribution of the polymer chain end-groups increase as the polymer chain length decreases.[41,42] For instance, Moreira et al. showed the surface tension of polystyrene (PS) at 200 °C decreases by 24% as the molecular weight of PS decreased from 200000 to 12500 g/mol.[41] Jalbert et al. also report that the surface tension of trimethyl siloxy

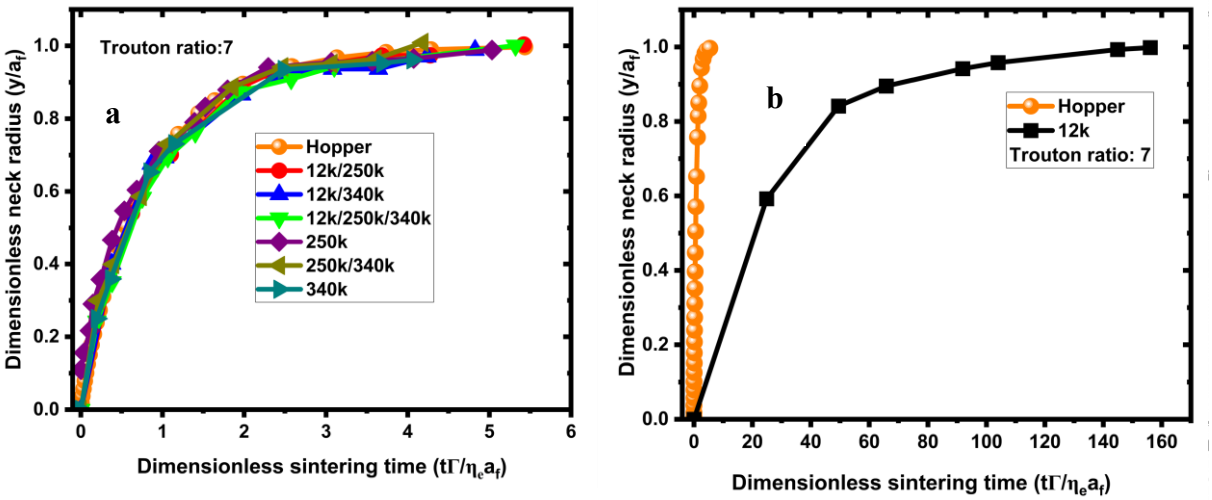

Figure 17. Comparing PP experimental coalescence data to Hopper model using extensional viscosity of PP powders. (a) High Mw and blends, $\eta_e = 7\eta_0$ (b) 12k Mw, $\eta_e = 7\eta_0$

terminated PDMS increased approximately by 14% as molecular weight increased from 1000-75000 g/mol.[42] However, in order to account for the dramatic variation of the data in **Figure 17b**, the surface tension of the 12k PP would have to decrease by 97 % from the surface tension of the higher Mw counterparts. This seems unlikely, leading to the conclusion that variation in the surface tension of the 12k sample is not sufficient to describe the data in **Figure 17b**, and thus additional factors must be impacting the coalescence of the 12k powder.

The Hopper model provides insight into the processes that govern the stretching regime of the coalescence process, which occurs after the initial zipping mode. Thus, this coalescence model models only the stretching process and therefore assumes that the zipping mode is much faster than the stretching mode and does not contribute to the experimentally measured coalescence rate. The zipping process typically occurs on a short timescale, often taking only a fraction of a second to a few seconds, whereas the stretching process can take considerably longer, often on the order of tens of seconds to minutes. It should be noted that the experiment does monitor both the zipping and the stretching processes during coalescence. Inspection of the Hopper model indicates that the stretching mode for the 12k sample (based on its viscosity and surface tension) is complete in a fraction of a second. However, the experimental data shows that the coalescence of 12k sample takes about 3 seconds, suggesting that this experiment is primarily monitoring the zipping process, which takes 2-3 seconds. If this is true, it is not surprising that the Hopper model does not accurately model the coalescence behavior of the 12k sample – the Hopper model provides insight to the *stretching* regime of the coalescence process, while the experimental results of the 12k sample primarily document the *zipping* regime of the coalescence process. This in turn suggests that the Hopper model is only valid if the stretching regime takes significantly longer (~3-4×) than the zipping regime.

The question therefore arises as to whether the zipping process, which takes about 3 seconds, is short enough to be ignored in the monitoring of the coalescence of the higher molecular weight samples. As shown in **Figure 15**, higher molecular weight samples complete their coalescence in ~ 20-330 seconds. This appears to be sufficiently longer than the zipping process, which we estimate to be 1-3 seconds based on the behavior of the 12k sample. Thus, the timescales associated with the coalescence of the high molecular weight polymer and blend samples monitored represent the *stretching* regime in the coalescence of these materials. Because the Hopper model effectively describes the stretching process, the model accurately describes the coalescence behavior of the high molecular weight polymer and blend samples.

Role of 12k PP in Coalescence of Molecular Weight Blends

The results presented in **Figure 17** show that the Hopper model does a very good job of modeling the coalescence behavior of the 250k and 340k powders, as well as for all of the molecular weight blend powders but does not accurately model the coalescence behavior of the 12k powder. This is somewhat surprising, as one might expect that the dynamics of the powders with a significant amount of 12k polymer to coalesce more similarly to the pure 12k powder than to the coalescence of the higher molecular weight polymers. However, this is not the case, where the coalescence of the molecular weight blends is accurately modeled by the Hopper model using the extensional viscosity of the blend and the estimated surface tension of 0.03 N/m. This, in turn, indicates that the surface tension of the molecular weight blends does not significantly deviate from 0.03 N/m, which can provide some insight into the role of the 12k PP on the coalescence of the molecular weight blends.

Previous work by Dee et al. [87] and Quian et al.[88] show that the surface tension of a miscible blend of low and high molecular weight polymer is slightly lower than that of the high Mw polymer. However, this decrease is subtle (4-7%) and similar behavior in our samples will

not alter the agreement of the experimental data and the Hopper model in our analyses. Nevertheless, if the low molecular weight polymer segregates to the surface of the powder, as one might expect in a multicomponent sample, it will form a shell that is rich in 12k polymer. **Figure 18** illustrates the potential morphology of such a surface segregated 12k corona (i.e., a core shell) as well as that of a homogeneous mixture of the high and low MW PP. In a core shell morphology, the excess 12k polymer at the powder surface would lower the viscosity of the shell and dramatically speed up the droplet coalescence of the molecular weight blend powders, as well as potentially lower the surface tension of the powder. We would expect that such a morphology would coalesce more rapidly than the Hopper model. However, the coalescence of the molecular weight blend powders fit the Hopper model with no adjustable parameters, which is consistent with the homogeneous distribution of 12k PP in the powder —but is not consistent with the surface segregation of the 12k PP in the powder. Thus, these results indicate that the 12k powder does not surface segregate in these powders. Rather the 12k PP is homogeneously distributed in the blend powders, impacting the coalescence process by lowering the viscosity of the polymer melt, but not altering the near surface properties of the droplet that would also alter the coalescence process.

Thus, one important conclusion of these studies is that the coalescence of these molecular weight blend powders is dominated by the variation in extensional viscosity of the powders, where lower average molecular weight correlates to lower viscosity and faster droplet coalescence. Moreover, this molecular design of powders offers a straightforward and broadly applicable mechanism to tune the coalescence properties of polymer powders for laser-based powder bed fusion.

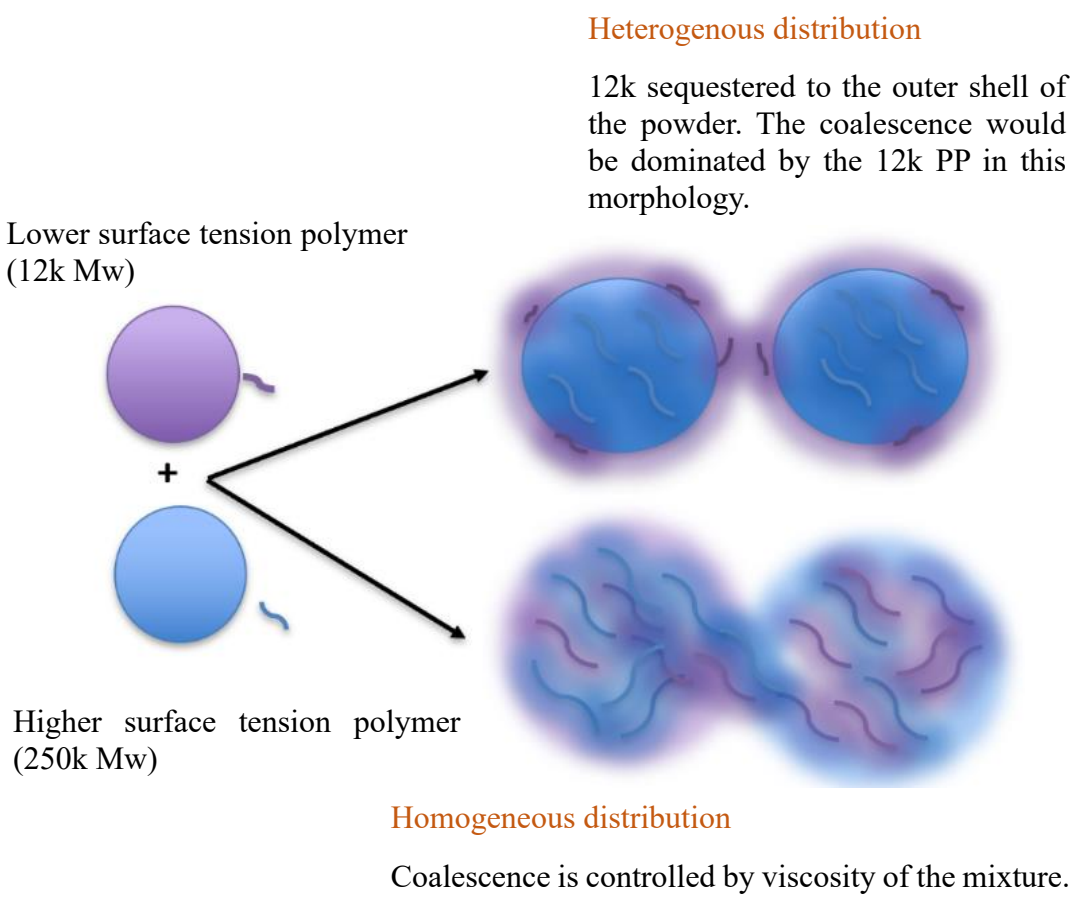

Figure 18. Schematic illustration for possible distribution of components in the molecular weight blend powders formed by the TIPS process.

Conclusions

This work describes the use of a processing protocol based on liquid-liquid phase separation to controllably design unimodal, bimodal**,** and trimodal molecular weight powders to investigate the dependence of polymer molecular weight, and thus zero-shear viscosities, on particle coalescence rate and their implication in polymer laser sintering. The data presented indicates that the addition of 12k low molecular weight PP to form bimodal and trimodal blends significantly increases the coalescence rate of the blend powders due to a substantial reduction in powder viscosity. Strong correlation between experimental results and the Hopper model of coalescence is observed, assuming correction for extensional flow for all samples, except in pure 12k PP sample. This demonstrates the significance of extensional flow in the coalescence of polymer particles. The results also indicate that the 12K PP in the blend powders is homogeneously distributed, improving the coalescence process by lowering the extensional viscosity of the polymer melt, but not altering the near surface properties of the droplet that would also alter the coalescence process. These results, therefore, provide a straightforward mechanism to tune the coalescence properties of powders and offer pathways to optimize the consolidation of particles in laser powder bed fusion.

Chapter 3: Impact of Polymer Molecular Weight Blends on the Powder Bed Fusion Process and the Properties of Polypropylene Printed Parts

Abstract

Designing and controlling the molecular characteristics of polymeric feedstocks is crucial for creating robust structures via the powder bed fusion (PBF) process. To explore the impact of a powder's molecular weight on printed part structure and properties, thermally induced phase separation was employed to produce spherical, appropriately sized polypropylene (PP) powders formed from individual unimodal molecular weights and molecular weight blends. More precisely, these powders are composed of 12,000 Daltons PP (12k), 250,000 Daltons PP (250k), or 340,000 Daltons PP (340k), as well as their blends (50/50 wt.% of 12k/250k, 12k/340k, 250k/340k, and 33/33/33 wt.% of 12k/250k/340k). Analysis of the printed parts from these powders shows that the blended molecular weight samples exhibit lower void space and higher crystallinity than the unimodal Mw counterparts. More importantly, dynamic mechanical analysis of the printed parts shows a substantial increase in storage modulus for blended molecular weight samples compared to unimodal Mw counterparts. This significant enhancement in the mechanical property of the blended molecular weight samples is due to improved coalescence dynamics driven by the powders' decreased melt viscosity. Improved coalescence reduces the void space in the printed parts, thereby improving mechanical performance. These results, therefore, provide a molecular-level understanding of the mechanism by which low Mw additives improve PBF processability, presenting avenues to augment the macroscopic properties of the printed parts. Additionally, the design powder approach presented in this work is cost-effective and offers a simple strategy to enhance the final part properties across various materials in additive manufacturing.

Introduction

Powder bed fusion (PBF), also known as selective laser sintering (SLS), is an additive manufacturing (AM) process in which objects are created by using laser energy to melt and

coalesce powders in a layer-by-layer fashion.[22,89] The PBF process offers numerous advantages among polymer AM technologies, including the ability to process semi crystalline polymers, high geometrical flexibility, and the ability to create customized parts without the need for dedicated support structures. [89,90] However, despite these advantages, parts produced through PBF often exhibit inferior mechanical properties when compared to those manufactured via traditional polymer processing techniques, such as injection molding.[90,91] At a molecular level, the poor mechanical properties associated with PBF fabricated parts are due to weak interfacial adhesion between layers caused by poor chain mobility, void spaces caused by insufficient coalescence, and poor molecular chain entanglement at the interface between adjacent layers. [91-94] Moreover, the physics that govern the PBF process involves complex thermal histories that differ substantially from conventional manufacturing processes.

Another major constraint restricting the application of PBF for manufacturing is the limited range of materials available for the PBF process. For instance, the clear majority of the polymeric materials used in PBF are polyamides (PA12 and PA11).[95] In order to expand the availability of polymeric materials for PBF, it is important to understand the relationship between fundamental material properties of newly developed powders and their printability, as well as utilizing an economically viable method to make powders from a wide variety of polymers.

Impact of powder properties on PBF process

Effect of particle size and size distribution on PBF process

The first step in forming a layer in the PBF manufacturing process is powder recoating, which involves spreading polymer powder evenly onto the powder print bed using a roller.[22] Efficient flowability during this powder-spreading step is imperative to achieve a densely packed powder bed that leads to more dense printed parts.[22] The flowability of the powder during the recoating process depends on the powder size and shape; powders with a spherical shape and

smooth surface are desirable in the PBF process because of their better flowability and packing efficiency.[21,22,33] If particles are too small, they may "evaporate off" when exposed to the high-energy beam, fogging the optics and heating elements and thus reducing the efficiency of the print process.[96] Furthermore, excessively small particles can adhere to the recoating roller due to electrostatic forces.[80] In fact, Averardi et al. highlighted that using particles smaller than 10μm in PBF tends to result in agglomeration or aggregates due to strong cohesive forces, hampering powder flowability and layer density.[97] Hence, utilizing powders with appropriate particle size and distributions in the PBF process is crucial for optimal printability.[21,79,97] A commonly recommended average particle size for powder bed fusion is usually 40-100 μm.[80]

After the powder recoating process, a laser heats the powder to selectively melt the powder to form melt pools at points in the layer to build the structure.[21,22,33] However, large variations in particle size can result in the complete melting of small particles and only partial melting of large particles, where incomplete melting of the larger particles results in incomplete coalescence of the powders and voids in the printed parts.[92,50] The time needed to conduct the heat from the laser throughout the particle strongly depends on the particle size of the powder. For example, the amount of laser energy required to raise the temperature of the powder particle correlates directly with the particle size. This relationship can be estimated using the following Equation: [79]

$$\boldsymbol{Q = mc_p \Delta T}$$

, where Q is the heat energy, m is the mass of the powder particle. c_p is the specific heat capacity of the particle, and ΔT is the temperature difference. Replacing the mass of the particle in Equation 1 by the particle density (p) times volume of the particle shows the dependence of the amount of heat required to raise the temperature of the powder particle (Q) on the particle radius. This substitution leads to the following Equation :

$$Q = \frac{4\pi r^3}{3} p c_p \Delta T$$

, which shows that Q varies with the particle radius cubed, r^3. Moreover, the characteristic time for heat conduction from the laser-illuminated area to the surrounding region of the particle, t_c, varies with the particle radius as r^2 , as shown in the following Equation:

$$t_c = \frac{4r^2}{\alpha}$$

, where α is the thermal diffusivity of the particle.[79] The Equations above offer a quantitative understanding of how powder particle size can impact the PBF process, where, under the same experimental condition, larger particles require more laser energy to melt and coalesce at a slower rate than smaller particles. [79,92,96] Additionally, the conduction of heat through larger particles takes a longer time than in smaller particles.[79] The absorptivity of laser energy by the particle also diminishes with increasing particle size, which is attributable to a reduction in the surface area-to-volume ratio. Smaller particles provide a larger surface area to absorb more laser energy, leading to a faster melting and coalescence rate.[97] Hejmady et al. showed that increasing particle radius from 30 to 105 μm, the ratio of the laser spot size to particle size decreases from 0.66 to 0.19; with a larger particle, a substantial portion of the particle may not efficiently absorb the laser energy, resulting in a pronounced temperature gradient within the particle, consequently decreasing the coalescence kinetics.[79]

Effect of particle shape on PBF process

In the PBF process, the geometry of powder particles affect their ability to flow during the recoating process to form a thin layer .[22,98-101] A freely flowing powder is also required to achieve a high packing density within the powder bed and to minimize interstitial voids between particles prior to coalescence to create dense parts.[22] The flow of particles during

recoating is also significantly influenced by interparticle forces. Spherical particles, for instance, result in minimal contact between particles, reducing inter-particle friction. This characteristic improves particle flowability, enhancing the overall flow dynamics during the recoating process.[98]

The packing quality of the powder bed also has a substantial impact on the heat transfer characteristics and flow of the molten materials during the printing process. Studies indicate that higher packing density of the powder in the bed minimizes void spaces between particles, thereby enhancing the thermal interaction among particles during sintering.[97,102] Numerous studies have correlated the packing efficiency of the powder bed to particle shape. For example, Nasato et al. and Haeri et al. investigated the dependency of the packing density of the powder bed on the particle aspect ratio.[99,100] Their findings show that as the particle aspect ratio increases, the packing density of the powder bed decreases. Deng et al. show that with increasing particle aspect ratio, the distribution of contact angle between the particles becomes wider, resulting in less packing of the particles and increased void spaces between the particles.[101] Given these findings, spherical and regularly shaped particles are preferred in the PBF process due to their superior flowability characteristics and higher packing efficiency compared to non-spherical and irregularly shaped particles.

Effect of polymer molecular weight and viscosity on PBF process

After selective heating of the powder by the laser beam, the melted powders coalesce and then solidify upon cooling to form intra- and inter-layer bonds.[21,22] Polymer viscous flow and particle coalescence control densification and impact the final mechanical properties of the printed parts. Sufficient particle coalescence within one layer and across layers is essential to achieving a homogeneous structure with few defects and mechanically robust 3D-printed parts.[33]

Viscous flow is a crucial driving force of the coalescence phenomena in the PBF process.[21] Theoretical models, such as the Frenkel model describe viscous coalescence with critical parameters that govern the coalescence kinetics, including, polymer zero-shear viscosity and surface tension .[21,22,33,79] No mechanical pressure is applied to the polymer during the PBF process as opposed to the injection molding process,[103] which results in the coalescence of particles in the PBF process being dependent on the zero-shear viscosity of the polymer melt. This is quantitatively shown in the Frenkel model:

$$\frac{\boldsymbol{x}}{\boldsymbol{a}}(\boldsymbol{t}) = \left(\frac{\boldsymbol{3\Gamma t}}{\boldsymbol{2a\eta_0}}\right)^{\boldsymbol{1/2}}$$

, where an increase in the zero-shear viscosity leads to a decrease in the time evolution of the coalescence ($\frac{x}{a}$ (t)).[22] In this Equation, x is the neck radius between two adjacent coalescing particles, a is the initial particle radius, t is the coalescence time, Γ is the surface tension of the polymer, and η_0 is the zero-shear viscosity of the polymer. η_0 is related to polymer molecular weight (Mw) via the following Equation:

$$\boldsymbol{\eta_0 = cMw^{3.4}}$$

, where c is a constant.[43]

The timescale associated with particle coalescence in the PBF process is ,only approximately 10 seconds[21]; thus, polymers with higher molecular weights, and higher viscosities, may not be exposed to laser power long enough to melt and sufficiently flow to complete consolidation within this short timescale. Therefore, we hypothesize that designing polymeric materials with tunable zero-shear viscosity to improve polymer flow during coalescence could improve interfacial adhesion, powder consolidation, and thus part robustness.

Strategies to enhance consolidation of particles and improve mechanical strength in PBF printed parts

Manipulation of print settings

Various mechanistic approaches have been attempted to promote the consolidation of particles and improve mechanical strength in PBF printed parts. For instance, the effect of laser power on the density on the tensile strength of PA12 printed parts by PBF has been investigated by Yan et al.[20] Their findings show that the density and the tensile strength increase with increasing laser power until they reach a maximum value and then further increasing laser power results in the decrease in the density and the tensile strength. Similar results have been reported by Zhu et al. in the PBF of Polypropylene (PP).[82] The correlation between increasing laser power (P_L) and the improved mechanical properties of the PBF printed parts is not surprising, as it stems from the direct relationship demonstrated in the Equation:

$$\boldsymbol{E_D = \frac{P_L}{D_l \times H_s \times V_S}}$$

, where increasing P_L will consequently increase the energy the laser beam delivers to the polymer powder per unit area (the energy density [E_D]), assuming all other parameters remain constant.[22]

In this Equation, H_s is the hatch spacing, D_l is the laser diameter, and V_S is the laser beam speed. Increasing laser power, thus, increases energy density, raising the powder temperature, which lowers the viscosity of the polymer, and fosters a faster coalescence during the printing process. However, increasing the energy density to extremely high value can lead to material degradation and dimensional errors in the printed structure .[20,82]

Material modification

Material degradation poses a significant limitation to parameter -based approaches to improving printed part properties . Therefore, material design, such as modifying the polymeric material rather than altering the physical print parameters and understanding how polymer feedstock molecular characteristics impact particle consolidation during printing are viable ways to design materials to fabricate mechanically robust 3D-printed parts. Hence, this study focuses on modifying the molecular characteristics of the polymer feedstocks to optimize the crucial consolidation processes in PBF.

In previous work by our group, designing bimodal molecular weight materials has been proven to enhance the mechanical performance of material extrusion-based 3D-printed structures. For example, Levenhagen et al. designed bimodal blend polylactic acid (PLA) filaments by incorporating lower molecular weight PLA additives into commercially available higher molecular weight PLA filament. The lower molecular weight PLA additives improve polymer chain diffusion between layers, strengthening the interfacial adhesion between layers in structures created by the fused filament fabrication (FFF) process, and result in mechanically robust 3D-printed parts.[58] Lower molecular weight additives in a polymer melt readily sequester to the interface of the filament, where they can more quickly form entanglement between layers relative to the diffusive processes of their higher molecular weight counterparts.[8,58]

Given this fundamental process and the importance of polymer molecular motion in particle coalescence in the PBF process, we hypothesize that the utility of such a molecular modification protocol will improve the mechanical performance of polymer parts fabricated by PBF. From the Frenkel model, it is clear that the zero-shear viscosity is a dominant parameter that governs polymer flow during coalescence, and thus the coalescence process. Moreover, the zero-shear viscosity has a well-known relationship to polymer molecular weight (Eq. 2), opening

avenues to control this crucial parameter by modifying the average molecular weight of the polymer. Thus, this work is designed to examine the impact of molecular weight blends of polypropylene (PP) powders on the PBF process and the properties of the printed parts.

To achieve this aim, we utilize thermally-induced phase separation (TIPS)[13,15] to create powders with bespoke molecular weight distributions, where high molecular weight PP is blended with an identical, but low Mw, PP to form molecular weight blends of PP. By combining low molecular weight PP with high molecular weight PP, we expect the viscosity of the blend to be significantly lower than that of the high molecular weight PP, potentially facilitating molecular mobility and improving the coalescence dynamics during the PBF process. This targeted improvement of the coalescence process is shown schematically in **Figure 19**. Thus, under the same thermal energy of the PBF process, we expect that the coalescence of the molecular weight blend powders will be faster, potentially reducing internal voids and creating a more robust structure relative to structures formed from neat high molecular weight polymer. As illustrated in **Figure 19**, a high degree of coalescence and substantial void space reduction should result in improved densification and enhanced mechanical performance of the printed parts. Providing this understanding of molecular-level mechanisms governing particle fusion establishes a solid foundation for the strategic creation of polymeric feedstocks for improved PBF printing. Moreover, developing materials with molecular weight blends presents a cost-effective approach to tailor feedstocks, effectively tackling some of the existing challenges encountered in the PBF process. This work aims to provide a fundamental understanding of the mechanism by which polymer molecular weight and, thus zero-shear viscosity, controls the fabrication of structures in the PBF process. PP is an important thermoplastic as it is widely

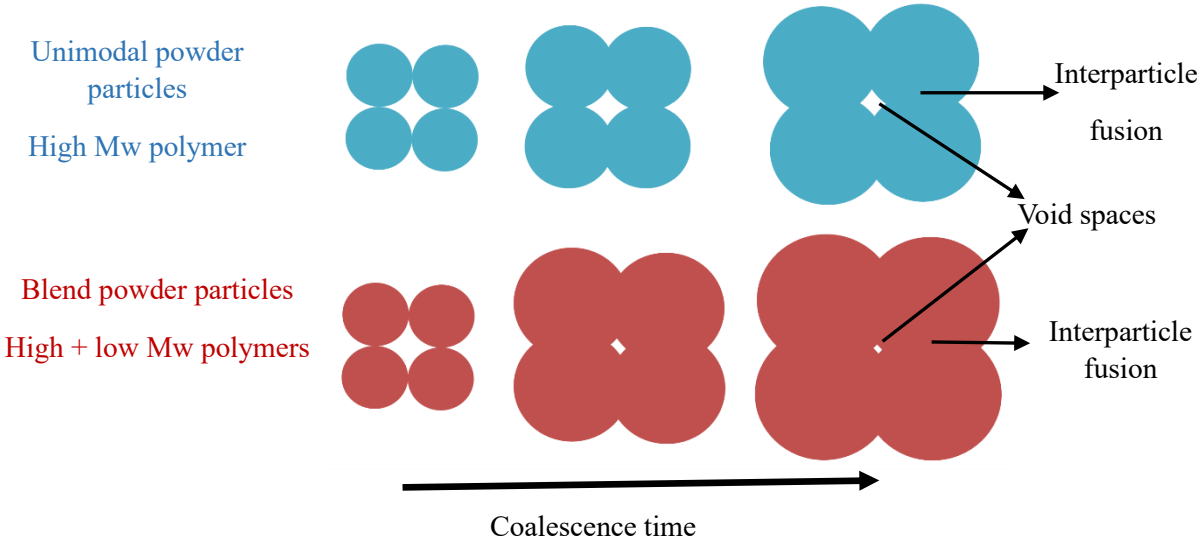

Figure 19. Proposed strategy to enhance coalescence and decrease void space in high Mw polymer by molecular modification. Under the same experimental condition, molecular blend sample should exhibit higher level of coalescence and lower void space than unblended sample.

applicable across various industries due to its good mechanical performance, chemical stability, and relatively low cost.[82] Understanding how polymer molecular weight affects PBF fabrication will not only contribute to improving PP printability but also potentially pave the way for advancements in other materials processed by PBF.

Experimental Methods

Materials

Isotactic polypropylene pellets with molecular weights of 12,000, 250,000, and 340,000 Dalton were purchased from Sigma-Aldrich. Xylene, ethanol, and silicone oil were purchased from Fisher Scientific. All chemicals were used without further purification. Throughout this work, molecular weights of 12,000, 250,000, and 340,000 Dalton will be denoted by 12k, 250k, and 340k Dalton, respectively.

Production of PP powders via thermally-induced phase separation (TIPS)

Thermally-induced phase separation (TIPS)[13,15] was used to form PP powders for PBF. With this process, PP powders were formed from neat 12k, 250k, and 340k PP pellets, 50/50 wt.% blends of 12k/250k, 12k/340k, and 250k/340k and a 33/33/33 wt.% blend of 12k/250k/340k. To fabricate each PP powder sample, 9g of PP pellets were added into a 250 ml round bottom flask. 91g of xylene was added, and the mixture was heated with a hotplate to 190 °C, stirred at 200 rpm, and refluxed for 1 hour to form a homogeneous solution. After 1 hour of reflux, the mixture was placed into a cold trap at 40 °C using a Fischer Isotemp, containing a mixture of 50% water and 50% ethylene glycol as the refrigerant and quenched for 1 hour to precipitate the powders. After the quenching process, vacuum filtration was perform to separate the precipitate, where the PP powders were washed with ethanol three times to remove residual xylene. The obtained powders were then placed in a vacuum oven at 40°C and allow to dry until a constant mass is reached.

Characterization of the prepared PP powder

Evaluation of particle size distribution via laser diffraction particle size analyzer

The particle size and particle size distribution of the produced PP powders were determined with a Mastersizer 3000 laser diffraction particle size analyzer (Malvern Instruments Ltd). This analysis provides the particle size distribution and median diameter, Dx(50), for all the prepared PP powders, where Dx(50) represents the particle diameter value at 50% in the cumulative distribution.

Scanning electron microscopy (SEM)

Scanning electron microscopy (SEM) was performed to monitor the shape of the prepared powders. To obtain SEM micrographs of the samples, each sample was coated with a thin layer of gold to eliminate surface charging. The SEM used in this study is a ZEISS-EVO with high electron tension set at 20.00kV.

Zero-shear viscosity

The zero-shear viscosities of the PP powders formed from TIPS were determined via rotational rheometry using an AR200ex rheometer from TA Instruments at Oak Ridge National Laboratory. The viscosity measurement was performed at 164℃ and at 0.005 s^{-1} shear rate. Disc-shaped specimens that were 25 mm diameter and 1 mm thickness were prepared by compression molding at 170 ℃ for 5 minutes under 2 metric tons. A 25mm diameter parallel plate was used. Before each rheological measurement, the sample was thermally stabilized for 10 minutes to ensure thermal equilibrium. The temperature was stabilized within 0.2 K for all measurements.

Molecular weight determination

The molecular weight and dispersity of the PP powder samples prepared via TIPS were determined by a high-temperature Size Exclusion chromatograph, a Malvern high-temperature OMNISEC system, using 1,2,4 trichlorobenzene as the eluent, with solution concentrations

ranging from 1.0 to 3 mg/ml and calibrated to polypropylene standards. Viscometer, refractive index, low-angle light scattering, and right-angle light scattering detectors were used to obtain the molecular weight and dispersity data.

Thermal analysis of PP Powders

Data from differential scanning calorimetry (DSC) is used to establish the feasible PBF processing temperatures of the PP powders. The DSC data were obtained with a TA Instruments DSC Q2000.. Approximately 5-10 mg of each sample was placed in standard aluminum pans with covers and the DSC curves were measured at a heating rate of 10 ℃/min from 40 °C to 200 °C, followed by cooling to 40 °C at 10 ℃/min under nitrogen purge gas flow. The PBF processing temperature ranges are defined as occurring between the onset melting temperature and the onset crystallization temperature.

The thermal stabilities of the PP powders were determined via thermogravimetric analysis (TGA) using a TA Instruments TGA Q50 . Approximately 10 mg of each sample was heated from 40 ℃ to 600℃ at the rate of 10 ℃/min under nitrogen gas. The thermal stabilities of the PP powders are obtained from the peak degradation temperature of the TGA curve.

Powder bed fusion of the prepared PP powders

All prepared powders were printed using a Prodways Promaker P2000 HT machine. This machine is equipped with a 60 W, 10.6 μm, CO_2 laser. Using the processing temperature identified from DSC data, and based on preliminary experimental trials, samples were printed with bed and feed temperatures set to 140 °C , a laser power of 50 W, beam velocity of 3750 mm/s, and hatch spacing of 0.3 mm. These print parameters correspond to an energy density (E_D) of 0.044 J/mm^2. Laser parameters were held constant for all powder specimens to enable direct evaluation of the impact of molecular weight on the structure and properties of the printed parts. The bed and feed temperatures were set. conservatively to reduce the risk of powders

prematurely melting and coalescing in the powder bed prior to energy deposition, which is more likely as these set temperatures approach the onset of melting for a powder. Tensile testing dogbones and rectangular prismatic structures (21 mm x 6 mm x 1 mm) for dynamic mechanical analysis (DMA) were printed from the fabricated PP powders, as, shown in **Figure 20**.

Characterization of the PP printed parts

Dynamic mechanical analysis (DMA)

DMA (TA Instruments DMA Q800) was used to characterize the viscoelastic behavior of the printed samples. Storage and loss moduli curves were obtained with a frequency of 1 Hz and a strain of 0.1 % where the temperature was ramped from -50℃ to 120℃ at 3℃/min. Additionally, the glass transition temperature (Tg) of each printed sample was determined from the peak of the damping factor, tan δ. The DMA was performed in tensile mode.

Evaluation of crystallinity and crystal structure of the PP printed parts

Differential scanning calorimetry (DSC) curves were analyzed to determine the crystallinity of the printed structures. DSC curves were obtained with a TA Instruments DSC Q2000 Approximately 5-10 mg of the printed samples were placed in standard covered aluminum pans and measured at a heating rate of 10 ℃/min from 40 °C to 200 °C, followed by cooling to 40 °C at 10 ℃/min under nitrogen purge gas flow. The percent crystallinity, X_C, of the polymer samples was calculated from the experimentally determined heat of fusion according to the following Equation:[82]

$$\boldsymbol{Xc} = \frac{\boldsymbol{\Delta H_m}}{\boldsymbol{\Delta H_m^0}} \times \mathbf{100}\%$$

, where ΔH_m is the measured melting enthalpy, of the printed structure, and ΔH_m^0 is the melting enthalpy of fully-crystalline PP material (209 J/g).[104] Wide-angle x-ray scattering (WAXS) was also performed to investigate the variation in crystalline structure. WAXS curves were obtained

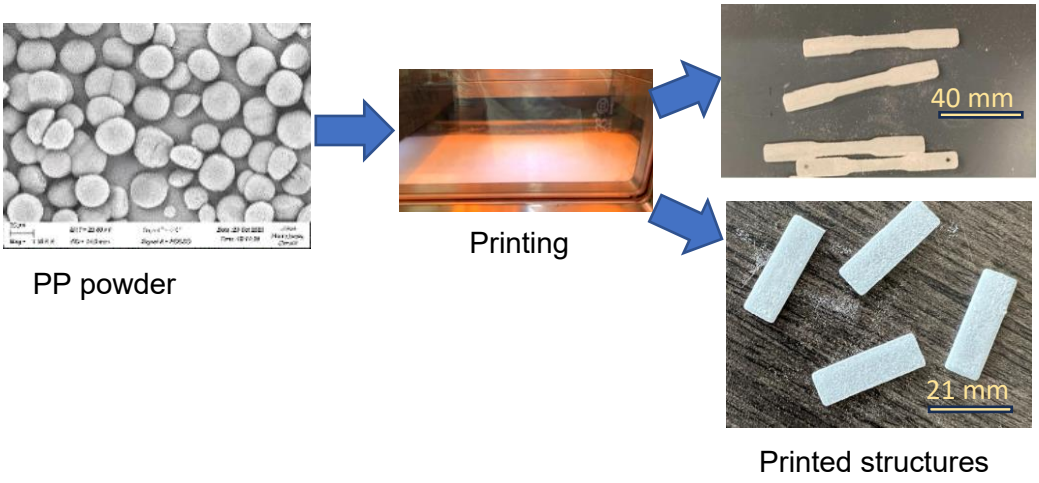

Figure 20. Powder bed fusion of the PP powder

using Xenocs Xeuss 3.0 X-ray scattering instrument. PILATUS3 R detector was utilized. The wavelength of incoming X-rays was 1.54Å. The sample detector distance was 0.045m. The printed solid samples were placed in a beam and scattered directly. All scans were obtained under a vacuum. Collected scans were analyzed using a Gaussian curve to obtain peak positions.

Void space evaluation via SEM and ImageJ software

Scanning electron microscopy (SEM) was used to determine the percent void space in the printed samples. Sample preparation included fracturing the PP printed samples with liquid nitrogen, followed by coating with a thin gold layer the sample surface to eliminate surface charging. The SEM used in this study is a ZEISS-EVO with high electron tension set at 5.00kV, where an example image is shown in **Figure 21**.

To determine the percent voids, ImageJ was first used to convert the SEM images to black and white, the Equation:

$$\textbf{Void space } \% = \frac{\textbf{total number of black pixels}}{\textbf{total number of black+white pixels}} \textbf{x100}$$

was then used to determine percent voids in the sample.

Results and Discussion

Particle size and distribution of fabricated PP powders

It is well known that the size of powder particles plays a critical role in governing particle flow dynamics during the recoating process, and thus directly affects the quality of the prepared powder bed and, its packing density. Thus, employing the proper particle size and distribution is vital for effective absorption of laser energy and ensuring proper coalescence during the printing process. Forming polymer powder with proper size and distribution for the PBF process is challenging but is required to create molecularly designed powders with similar size and distribution. Our previous studies have demonstrated that the TIPS process provides pathways to

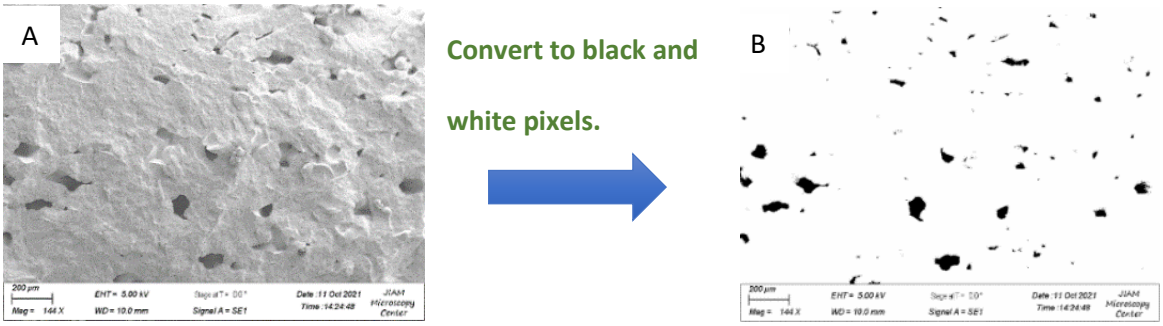

Figure 21. Evaluation of void space in the printed sample via SEM and ImageJ. (A) SEM image of the printed sample showing the void spaces. (B) converted SEM image of the printed sample to black and white pixels using ImageJ.

fabricate polypropylene powders of targeted size and distribution that are suitable for PBF.[13,15] **Figure 22** shows the size distribution of the powders created for this study, for both the neat polymers and all of the molecular weight blends. This figure shows similar size distributions and the production of powders with average particle size, Dx(50), that is consistent with the particle size range that is suitable for PBF. The successful production of the PP powders with target average sizes across various molecular weight and blends underscores the significance and the ability of the TIPS process in this study to develop and rationally control the powder production method to create bespoke feedstocks to address current challenges in the PBF process. Moreover, producing these PP powders with uniform sizes for all samples allows researchers to eliminate the impact of particle size on the PBF process. Summarily, PP particles of similar size require similar energy absorption and the influence of particle size on flowability and coalescence are comparable, allowing for a more detailed examination of molecular weight effects on the PP molecular weight on the PBF fabrication process.

SEM images of the structure of fabricated PP particles

Figure 23 shows SEM images of the fabricated PP powders, where the particles are spherical with smooth surfaces. However, a closer examination of the SEM images shows that the powders formed from the neat 12k sample have some particles that are crumpled, while the powders formed from the neat 340k sample shows some particles that have rough surfaces. Intriguingly, these structural characteristics are eliminated when the 12k sample is blended with high molecular weight polymers using the TIPS process This structural transformation becomes apparent in the 12k/250k, 12k/340k, and 12k/250k/340k powder particles. These variations in structure could be attributed to the complex interactions occurring during the formation of droplets from blends in the TIPS process. The fact that all the PP samples have identical shapes implies similar particle aspect ratios, suggesting comparable configurations in the print bed

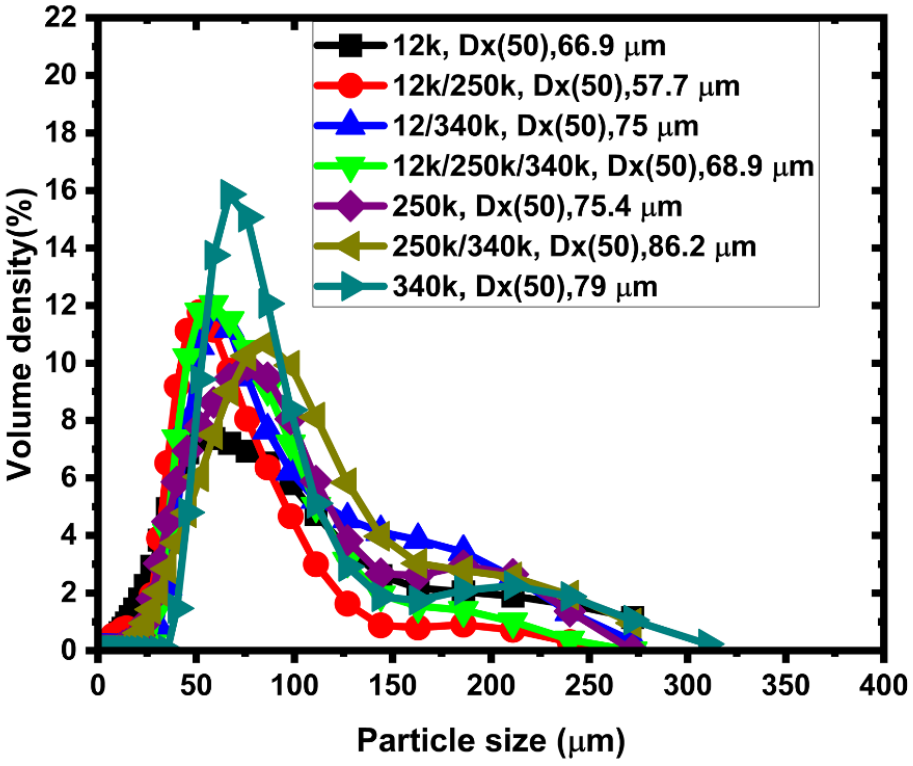

Figure 22. Particle size and distributions of produced PP powders analyzed using laser diffraction. The average particle size, Dx(50), is the proper size (58 μm - 86 μm) for PBF.

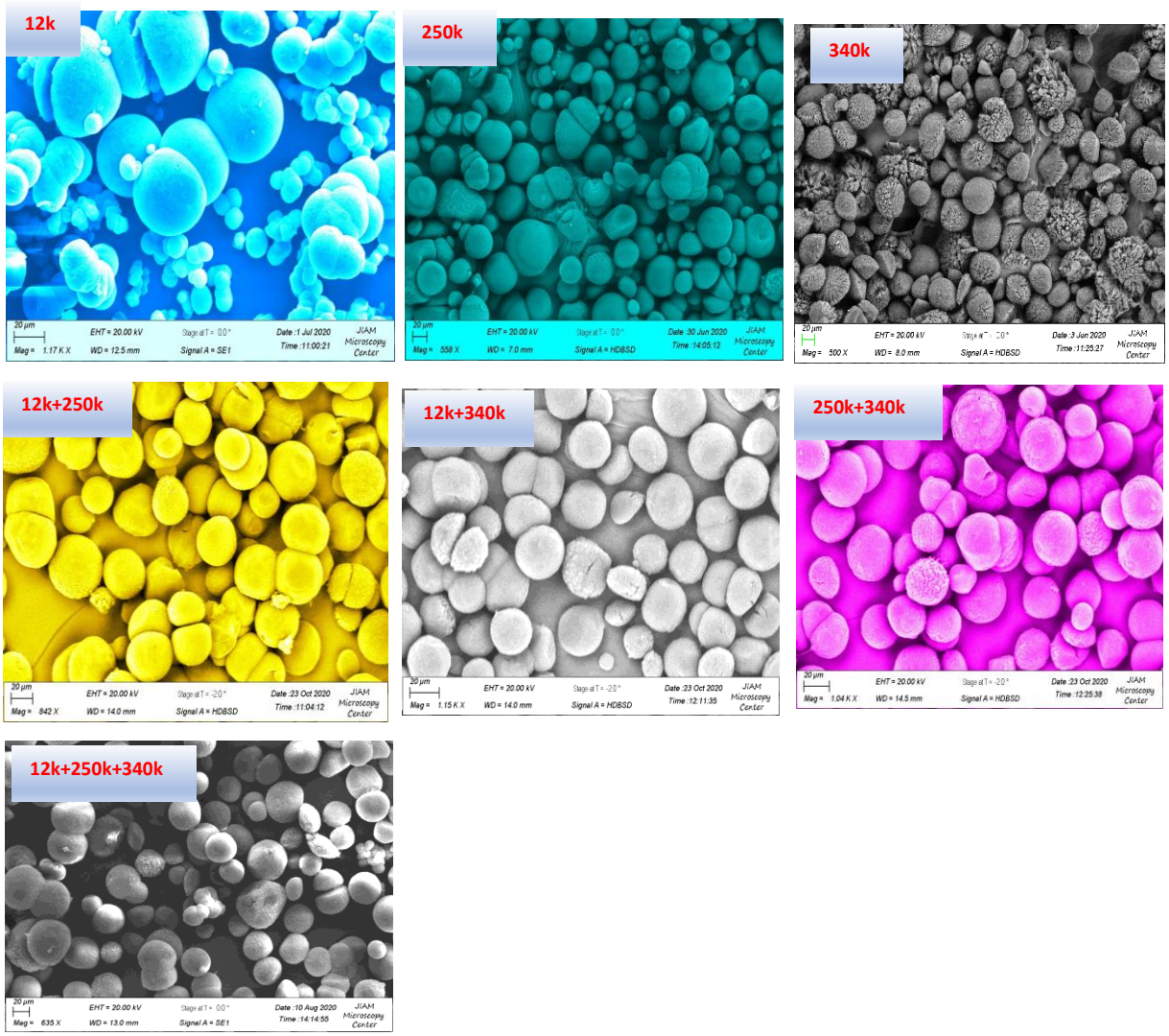

Figure 23. Structures of PP powders obtained via scanning electron microscope. PP samples produced in this work are highly spherical.

during powder spreading. This structural similarity provides a foundation to eliminate the impact of particle shape on the PBF process in this study. This, in turn, allows for a focused investigation of how the molecular weight of the powders influences the PBF process and the properties of the resulting printed structures, as detailed below.

Tuning powder zero-shear viscosity

Coalescence is a fundamental aspect of the PBF process that directly impacts the strength, quality, and properties of printed parts. It depends intimately on the surface tension and zero-shear viscosity of the polymer. **Table 2** shows the average molecular weight and the polydispersity of the PP powders made from the pure PP and their blends. It is evident that the inclusion of a polymer with lower chain length,12k PP, notably modifies the average molecular weight and polydispersity of the 250k and 340k PP counterparts.

Figure 24 correlates the zero-shear viscosities of the powders to the weight average molecular weight of the polymers, Mw, showing reasonable agreement of the expected molecular weight dependence of the polymer viscosity (Equation 2). The slight deviation of the molecular weight dependence of the polymer viscosity from Equation 2, the slope, is not uncommon. In particular, the zero-shear viscosity depends not only on the weight average molecular weight of the polymer but also on the polymer polydispersity,[83,84] which also varies significantly in these samples.

More importantly, the introduction of 12k PP to higher molecular weight PP provides a controllable method to significantly alter the molecular characteristics of the higher molecular weight polymers, substantially reducing their zero-shear viscosities; for instance, from 3,027 Pa.s for 250k to 349 Pa.s for 12k/250k, and from 7,031 for 340k to 426 Pa.s for 12k/340k. The results of these studies, therefore, offer a pathway to understanding the mechanism by which 12k additive impacts both the consolidation process of high molecular weight polymers and the overall quality of the printed structures. Moreover, the authors' prior examination of the particle

Table 2. Molecular weight characteristics of the PP powders prepared via the TIPS process.

PP samples used in the TIPS process	PP molecular weight of the powders produced via the TIPS process		
	Mw/Mn	Mw (1×10^3) Daltons	Mn (1×10^3) Daltons
12k	2.1	17	8.1
250k	2.2	280	130
340k	2.8	360	130
12k/250k (50/50 wt.%)	5.8	140	24
12k/340k (50/50 wt.%)	6.4	210	33
250k/340k (50/50 wt.%)	2.3	300	130
12k/250k/340k (33/33/33 wt.%)	14	230	17

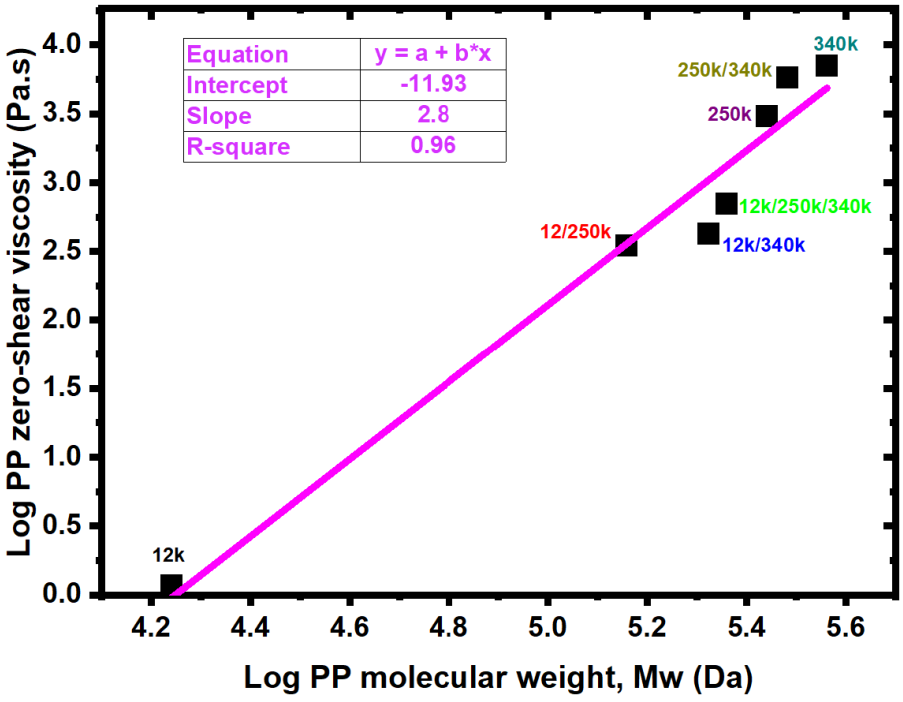

Figure 24. Zero shear viscosities of PP powders as a function of weight average molecular weight of the polymers.

coalescence of these powders shows that the addition of 12k significantly increases the coalescence rate of the powder.[105] The substantial decrease in zero-shear viscosity resulting from the addition of 12k PP is the dominant factor in the previously observed pronounced enhancement in coalescence.[105]

Impact of molecular weight on PP printability

All powders except that which is formed from the 12k PP were printable at PBF the set processing parameters. These printed samples showed minimal warpage during printing, which led to printed samples that could be tested mechanically. The PBF printing of the 12k powder, however, showed unique behavior. As shown in **Figure 25**, the structure that emerges from single layer scans did not match their defined geometry, which was a square in this case. While the outline of the scanned layer can be seen, it was observed that the molten polymer shrank from its defined shape after scanning to form a ribbed structure. In this ribbed structure, many pathways are thicker than the layer height.

Coalescence of a molten polymer in PBF depends on both the zero-shear viscosity and surface tension of the polymer. It is hypothesized that for the 12k sample, the viscosity is so low, that the surface tension dominates the coalescence process, leading to a sample that "over-coalesces". Since PBF research is primarily conducted on engineering or high-performance polymers with molecular weight significantly greater than 12k, it is likely that this material is below a threshold viscosity necessary for proper coalescence whereas the majority of materials researched in literature are above this threshold. Due to the over-coalescence that occurred in the 12k sample after scanning, multi-layer samples were not printable. This observation also emphasizes the need to more thoroughly understand the impact of polymer molecular weight, viscosity, and melt surface tension on the printing process.

Figure 25. Single layer scans of the 12k sample resulted in ribbed structures, which did not accurately match the set layer geometry.

Properties of the printed parts

Mechanical Performance of Parts Printed from Molecular Weight Blends

Figure 26 shows the thermomechanical behavior of the PP printed parts obtained from the DMA. Inspection of **Figure 26** shows that the parts fabricated from the molecular weight blends generally exhibit higher storage and loss moduli than that of the parts fabricated from the pure higher molecular weight PP. For example, at 50°C, the samples printed from the 12k/250k and 12k/340k powd250bit 52% and 194% higher storage modulus than the samples printed from the 250k and 340k powder, respectively. Also, at 50°C, the addition of 250k to 340k increases the 340k storage modulus of the printed part by approximately 102% and the storage modulus of the part printed from the 12k/250k/340k powder is 15% higher than the storage modulus of the part printed from the 250k/340k powder.

These results are surprising as conventional expectations would suggest that high molecular weight polymers often demonstrate superior mechanical properties compared to their low molecular weight counterparts. Additionally, one might expect that incorporating 12k PP in such large quantities to a high molecular weight polymer would adversely plasticize the polymer system, potentially weakening the mechanical strength of the printed parts. However, the findings presented in **Figure 26** contradict these assumptions. If the 12k additive were indeed causing detrimental plasticization on the polymer matrix, we would expect the mechanical properties of the samples printed from the 12k/250k, 12k/340k, and 12k/250k/340k blend powders to be significantly weaker than those of the samples printed from the 250k, 340k, and 250k/340k blend powders, respectively. **Figure 27** correlates the storage modulus of the printed parts to the polymer dispersity. Examination of **Figure 27** quantifies by how much the addition of 12k low molecular weight polypropylene to form molecular weight blends significantly increases the dispersity of the molecular weight blend powders; the data shows that the addition

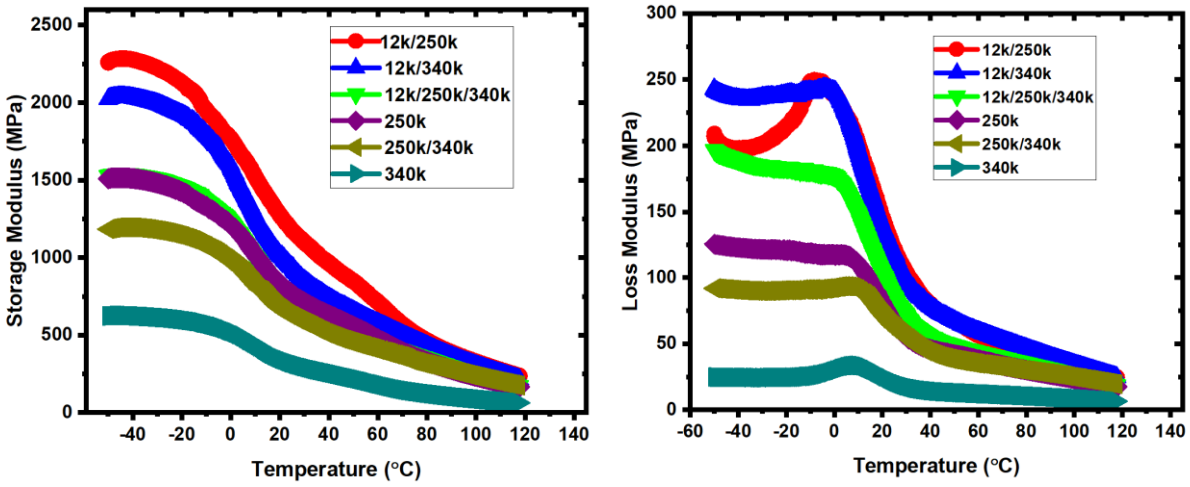

Figure 26. Thermomechanical properties of the PP printed parts

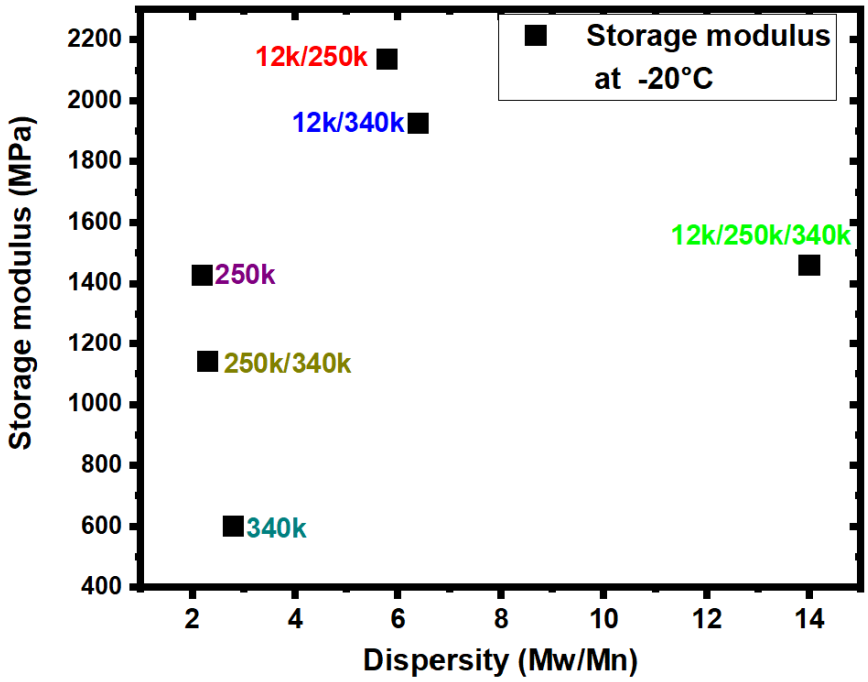

Figure 27. Correlating storage modulus to polymer dispersity

of 12k increases the dispersity of larger polymers by more than 100%. Interestingly, the data in **Figure 27** reveals that the blends with higher dispersity exhibit superior mechanical properties. This further verifies that the introduction of the 12k PP does not detrimentally plasticize the printed structures.

Furthermore, the storage modulus of the printed parts is plotted as a function of their glass transition temperature (Tg) in **Figure 28**. Unsurprisingly, the Tg of the polymer increases with increasing molecular weight, as one would expect from free volume theory.[106-108] However, as was observed in **Figure 28**, this lowering of Tg does not correspond to a decrease in storage modulus, as might be expected due to plasticization. Rather the samples printed form powders of lower molecular weight are stiffer (i.e. higher modulus) than those printed from higher molecular weight powders. This further emphasizes that the addition of 12k PP to larger polymers does not have a detrimental plasticizing effect on the mechanical properties, indicating that the variation in mechanical performance of the various molecular weight blends must be driven by other factors other than plasticization.

Hence, the subsequent sections are further analysis and experiments to provide insight into the underlying factors that drive the observed changes in the mechanical properties of the printed samples.

Crystallinity in printed structures and its impact on storage modulus

The addition of lower molecular weight additives to higher molecular materials can alter their crystallization processes during the PBF process, influencing changes in the percent crystallinity and crystal structures of the printed part that could contribute to the improved mechanical properties.[109,110] As shown in **Figure 29a** and **b**, the percent crystallinity of the PP printed structures determined by DSC ranges from 42-50%, which is consistent with previous studies.[109,110]

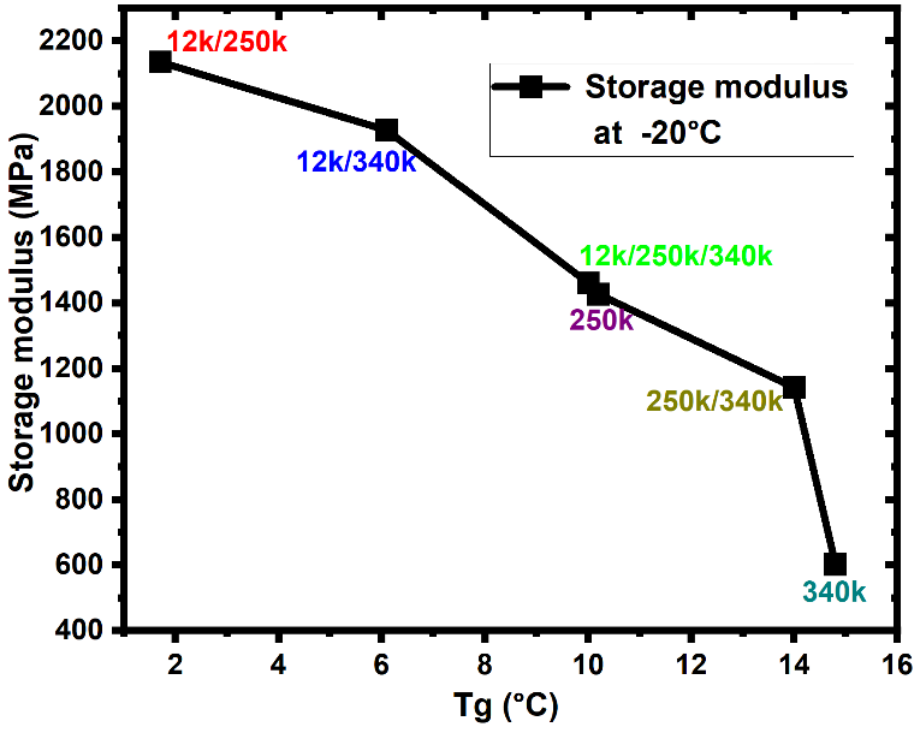

Figure 28. Correlating storage modulus of the printed structures to Tg

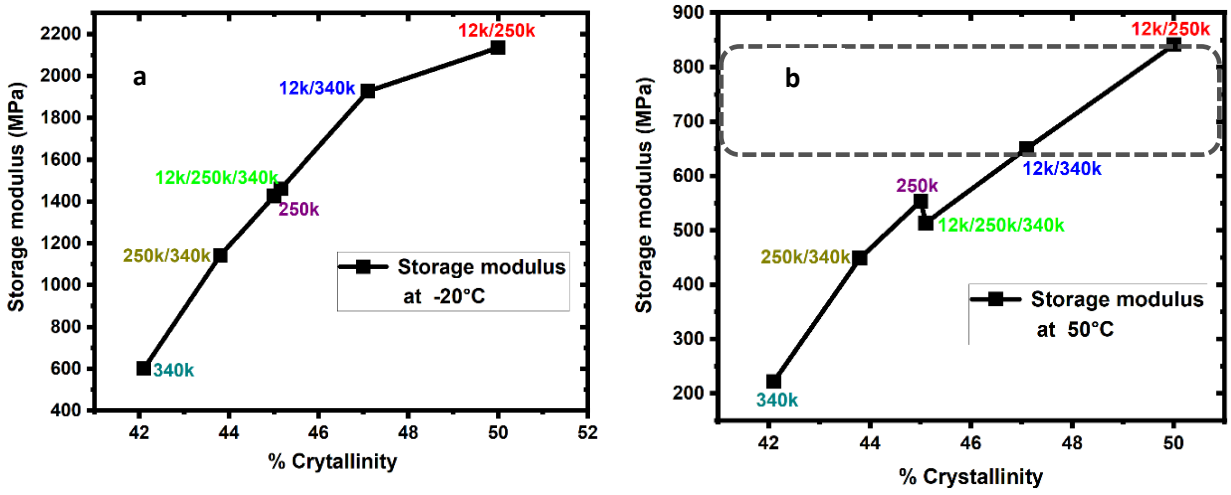

Figure 29a and b. Correlation of storage modulus with PP crystallinity at -20C (a) and 50 (b). The dashed box in Figure 11b shows the expected change in modulus at 50°C based on Li et al.[110]

The addition of 12k PP to the larger polymers, resulted in an increase in crystallinity, relative to those that are printed from powders that do not contain 12k PP. Moreover, **Figure 29a** shows a strong correlation between percent crystallinity of the printed structure and its storage modulus, where an increase in crystallinity corresponds to a commensurate increase in storage modulus. The dashed box in **Figure 29b** shows the storage modulus of melt pressed PP at 50°C with crystallinities that range from 42-50% as reported by Li et al.[110] It is interesting that the moduli of the samples printed from the 12k/250k and 12/340k powders approach the modulus of the melt-pressed PP parts.[110] Comparison of the relationship between % crystallinity and storage modulus of all of the printed samples, however shows that the modulus varies by at least a factor of four when the crystallinity changes from 42 to 50 %. This is a much broader range in modulus than the melt-pressed samples, and thus the change in percent crystallinity is not sufficient to account for the observed variation in storage modulus in the printed samples.

Furthermore, the crystal structures of the PP printed parts were examined by WAXS, as under certain conditions, PP can form different crystal structures, including α, β, and γ phases. Studies indicate that the presence of the γ phase in PP significantly contributes to enhancing mechanical performance.[111,112] Moreover, it has been established that lower molecular weight can notably augment the formation of the γ phase in PP[111,113], and PP can develop various crystalline structures, from spherulites to highly oriented shish-kebabs, which can significantly influence the properties of the printed part.[23]

Figure 30 shows the wide-angle x-ray scattering of all samples, showing that powder molecular weight does not affect WAXS scattering patterns. The lack of variation in the WAXS patterns indicates that the local ordering of the PP in the crystals is the same for all samples. Thus, the variations observed in the mechanical properties of the printed parts are not attributable to differences in any change in the packing of the PP molecules in the crystal structures.

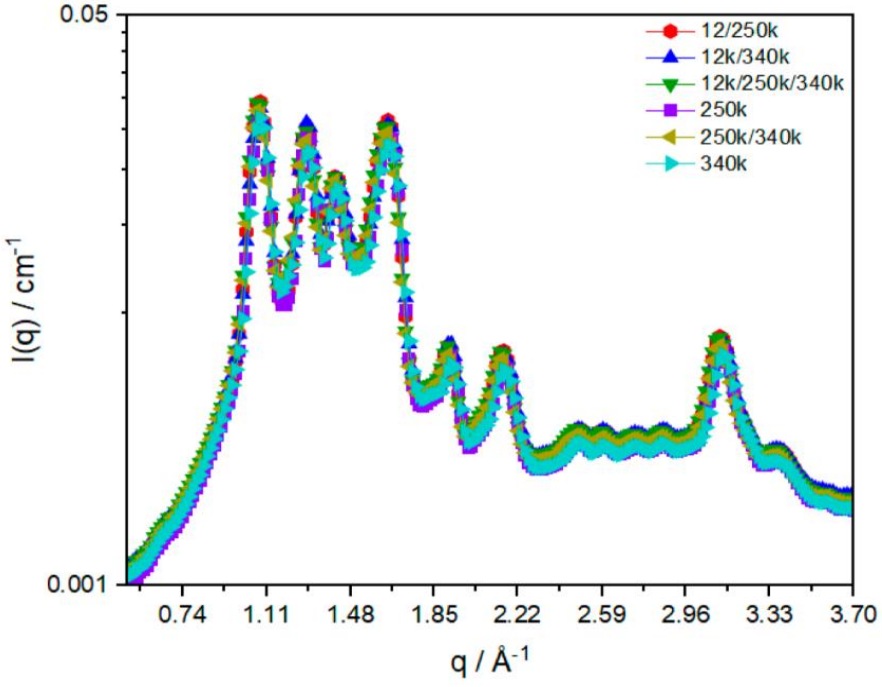

Figure 30. WAXS scattering patterns of the PP printed parts.

Void space in printed structures and its impact on storage modulus

PBF processing often results in parts with microstructural defects, including voids, which can adversely impact the performance of the printed structures. Large voids in PBF parts signify weak interparticle adhesion- often due to incomplete melting and/or incomplete particle coalescence, a detrimental aspect that limits mechanical integrity and consistency in manufactured parts.

The void fraction that is present in each PP printed structure was determined by analyzing SEM images of specimens' freeze-fractures. As shown in **Figure 31**, the presence of the 12k PP in the sample appears to decrease the amount of voids in the printed samples. Moreover, there is a strong correlation between the decrease in void space and an increase in storage modulus. This data appears to show that the inclusion of the 12k PP improves the particle coalescence during the printing process, limiting void space in the printed structure. Furthermore, the improved melting and coalescence of the powders results in improved mechanical performance of the printed parts.

We interpret these results to indicate that the incorporation of the low molecular weight 12k PP into the powder increases the molecular mobility of the polymer chain, thus enhancing particle coalescence without varying the print conditions. These results therefore suggest that incorporating a low molecular weight additive in the PBF powder lowers the zero-shear viscosity of the powder, promoting particle coalescence and interparticle adhesion, reducing void space, and thereby strengthening the printed structures.

In fact, the authors' prior droplet coalescence studies quantified how the molecular formulation alters the sintering process,[105] and showed that the powders containing 12k PP form substantial neck growth within very short timescales relative to the coalescence of pure molecular weight powders. For instance, the powder formed from the 12k/250k blend achieves

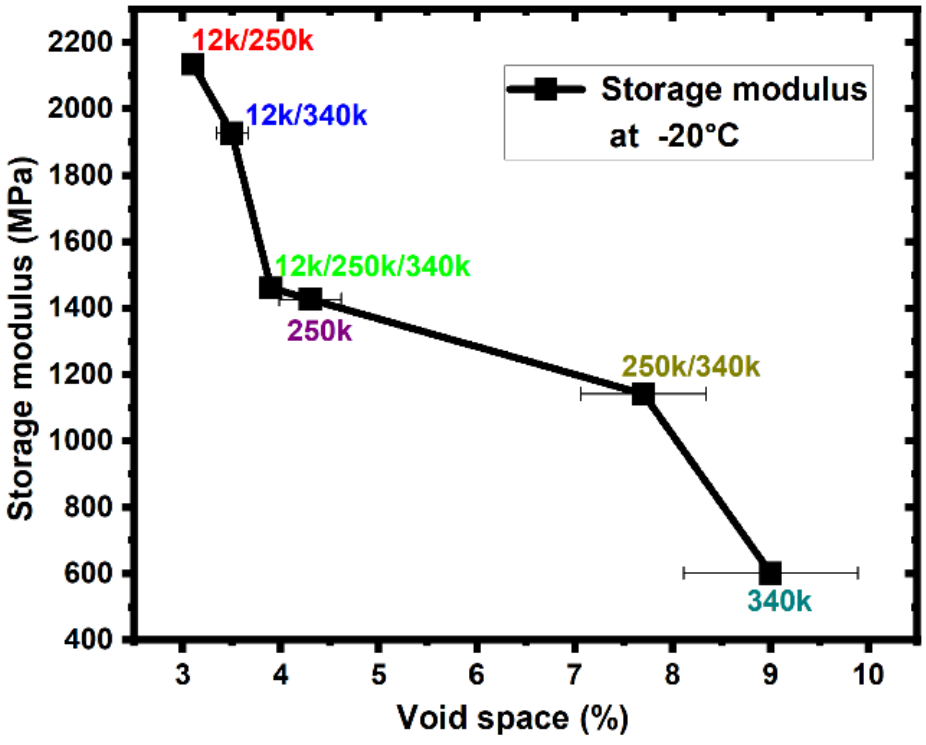

Figure 31. Storage modulus as a function of void space.

0.8 neck growth in just 4 seconds, while the powder formed from the pure 250k polymer only achieves 0.3 neck growth within the same timeframe.[105] The notable increase in rate of coalescence observed in powders formed from blends with 12k PP additives is attributed to a considerable reduction in zero shear viscosities, driving enhanced coalescence. Moreover, there is strong agreement between these experimental coalescence studies and the Hopper model, indicating that the 12k PP is homogeneously distributed in the powder and that the improved coalescence is primarily driven by the decrease in zero-shear viscosity.[105] Therefore, these studies demonstrate that molecular formulation of PBF feedstocks can tailor the zero-shear viscosities of powder polymer, enhancing their sintering during the PBF printing process, improving their suitability for the PBF process, and providing a mechanism to augment the overall performance of the structural printed parts fabricated by polymer powder bed fusion.

Conclusion

This study describes an innovative approach for tailoring the molecular characteristics of polypropylene powder feedstocks for the powder bed fusion (PBF) process via thermally induced phase separation (TIPS). Unimodal and molecular weight blend polypropylene powders were fabricated via TIPS to examine how their molecular design impacts the PBF process and the properties of the resultant printed part. All powders aside from those formed from 12k PP were printable at the set processing parameters. Failure to print the powder from the 12k PP suggests a minimum zero-shear viscosity to surface tension ratio is necessary to achieve proper coalescence of a scanned layer during the PBF process. Examination of printed parts using these powders shows that the molecular weight blended samples have decreased void space, increased crystallinity, and stronger mechanical properties relative to the parts printed from unimodal powders. Powders fabricated from designed molecular weight blends provide a route to improve the robustness of printed parts by improving coalescence during sintering, reduced void space,

and enhanced mechanical properties of the PBF printed parts. These studies thus provide the fundamental understanding of the mechanism by which low molecular weight additives in polymer blends can improve polymer PBF processability and offer pathways to optimize the macroscopic properties of the printed parts. Additionally, the designed protocol in this study can be applied to a variety of materials and processes in PBF additive manufacturing technologies.

Chapter 4: Design and Characterization of Polypropylene-Polycarbonate Blend Powders as Feedstocks for Powder Bed Fusion

Abstract

Developing new polymeric feedstocks and understanding their intrinsic and extrinsic properties is vital in advancing powder bed fusion (PBF) 3D printing technology. Blending multiple polymers is an effective method for creating new materials with desired properties. Our group has utilized a liquid-liquid phase separation (LLPS) processing method to incorporate polycarbonate (PC) into a polypropylene (PP) matrix to investigate its impact on PP powder properties tailored for PBF. The findings reveal that adding PC to PP does not significantly alter the spherical shape and size of the PP particles, suggesting that PP drives the formation of powder in the LLPS process. Energy dispersive X-ray spectroscopy experiments confirm the presence of oxygen peaks in every particle analyzed in the blend, with distinct variations in the intensity of the oxygen signal. This indicates that PC is present in all particles, but its content varies among individual particles. Morphological analysis of the powder via glass transition temperature (Tg) measurements revealed significant disagreements with the Fox model, where the Fox model underestimates the Tg of the blend. This suggests that PP and PC do not form a completely miscible system in the powder created by the LLPS process. More importantly, the examination of the crystallization behavior and crystal structure of the PP particles shows that the addition of PC results in faster crystallization, a decrease in percent crystallinity, and a reduction in lamella thickness of PP. The increased crystallization rate with PC addition could be attributed to the lowering of PP viscosity, potentially enhancing polymer chain mobility and consequently accelerating crystallization. The reduction in lamella thickness could be due to the presence of PC chains reducing the opportunity for crystalline regions to form during the crystallization process of PP. These results provide crucial insights into how PC impacts PP powder properties, offering avenues to tune PP printability and expand material options for the PBF process.

Introduction

Polymer powder bed fusion is a 3D printing technology that utilizes laser energy to selectively melt and coalesce polymer powders layer by layer, offering advantages in creating intricate geometries and functional parts directly from computer-aided design models.[18,114,115] Powder bed fusion (PBF) was pioneered at the University of Texas at Austin in the 1980s.[116,117] Although the technology has undergone numerous revisions and enhancements over the years, the printing process is fundamentally divided into three core sub-functions: first, powder (re)coating; second, energy input; and third, coalescence and cooling.[22,117] Powder properties, including particle size, particle size distribution, particle shape, viscosity, molecular weight, and crystallization, significantly influence these sub-functions.[22]

The first sub-function of the PBF process, powder recoating, refers to spreading a new, thin layer of powder material onto the build platform.[22] Spherical particles with smooth surfaces improve flowability during recoating and are preferred over non-spherical particles with rough surface morphologies. This is because irregularly shaped particles hinder tight packing, leading to lower packing densities.[22,118,119] One mechanism that hinders powder particle flowability is interparticle adhesion forces.[119,120] When these forces are strong, the particles stick together more readily, leading to high cohesiveness and causing the powder to form agglomerates, thus reducing flowability.[120] The size of powder particles is a crucial factor affecting the cohesiveness of the powder.[120] Smaller particles tend to have higher cohesion due to the larger surface area relative to their volume, which increases the effect of intermolecular forces such as van der Waals forces and electrostatic attractions. Mullarney et al. and Jallo et al. reported that powder particles smaller than 20 μm have sufficiently large specific surface area, which results in high adhesion to surfaces and strong cohesiveness between contacting particles, thereby decreasing flowability.[120,121]

The second sub-function of the PBF process, energy input, involves transferring heat energy from a laser to the powder particles, selectively melting them to form layers.[22] To efficiently melt the powder particle, it is crucial to have proper particle size distribution, as significant differences in particle size can cause smaller particles to melt completely, while larger particles may only melt partially. Under the same experimental conditions, larger powder particles typically require more laser energy to melt compared to smaller powder particles.[92] Partial melting of powder particles during the PBF process can lead to inadequate consolidation of the particles and an increase in voids within the printed parts, thereby reducing their mechanical performance.[92] Powder particles with a size range between 40-100 μm are commonly suggested for powder bed fusion.[80]

In the third and final sub-function of the PBF process, coalescence and cooling, the molten polymer particles flow into one another and merge before solidifying upon cooling and crystallization.[22] Coalescence is a vital aspect of 3D printing that directly impacts the strength, quality, and properties of the manufactured components. The viscosity, molecular weight (Mw), surface tension, and crystallization rate of polymer powders are crucial factors affecting polymer chain mobility during coalescence.[105,123,124]

One of the drawbacks of polymer powder bed fusion technology is insufficient coalescence during fabrication due to the high viscosity and rapid crystallization of the polymer melt. To address this, previous work in our group utilized a molecular design approach to tailor the viscosity of high Mw polypropylene (PP) to enhance their coalescence dynamics and the properties of the printed parts. Low Mw PP additives were incorporated into high Mw PP powder via a processing protocol based on liquid-liquid phase separation (LLPS) to create PP feedstocks for the PBF process. The results demonstrate that adding a low Mw PP (12 kDa) to a high Mw counterpart (250 kDa) significantly reduces the viscosity, enhancing the extensional flow and

increasing the coalescence rate of the high Mw PP. The enhancement in the droplet coalescence reduces void space and improves the mechanical strength of the resulting manufactured structures.[105,124]

In the context of powder formation, LLPS, also known as thermally induced phase separation, describes a process where a homogenized polymer solution at high temperature phase separates into polymer-rich and polymer-poor phases when it is cooled below the miscibility line.[13,28] Cooling the polymer solution below the miscibility line precipitates polymer powder, which can be obtained after removing the solvent.[13,26] LLPS is a cost-effective method for powder preparation, producing more uniformly shaped powder particles relative to cryogenic grinding , which leads to irregularly shaped particles and poor particle size distribution.[26,27]

In addition to insufficient coalescence during the fabrication process, PBF encounters several other challenges, such as a limited selection of polymeric materials available for fabrication, volumetric shrinkage and dimensional error, and residual stress.[114,125] Currently, polyamide-based feedstocks (PA12 and PA11) account for around 90% of the feedstocks used in the PBF process.[126] Conversely, commodity polymers, particularly polyolefins, constitute less than 5% of the PBF feedstocks.[126] Compared to polyamide materials, polypropylene (PP) has a lower processing temperature and better chemical resistance.[96,127] Additionally, PP is a highly cost-effective semicrystalline thermoplastics and is extensively utilized in consumer and technical products.[127]

Volumetric shrinkage and warp deformation of printed parts is one of the major challenges associated with printing semicrystalline polymer via powder-based and extrusion-based 3D printing.[23] This is predominantly due to the material-related crystallization rate, percent crystallinity, and crystal size.[96,125] Polymer crystallization takes place between the glass transition temperature and the melting temperature of a crystallizable polymer. When a sample

crystallizes, it develops a predominant crystal lamellar thickness, mainly governed by the kinetics of the crystallization process.[4] Thicker lamellae have greater thermal stability and thus require more energy to melt compared to thinner crystal lamellae under identical experimental conditions.[22] Moreover, in the PBF process, if the laser partially melts the crystals (for instance, if thicker lamellae are present in the powder) the partially melted lamellae will restrict polymer chain mobility during particle coalescence and lead to poor mechanical properties in the final printed part.[128] Dupin et al. showed that as percent crystallinity increases, the ductility, i.e. elongation at break, of the PBF printed structure decreases.[50] Thus, understanding and controlling crystallization behavior and crystal lamella thickness in 3D printing is vital to produce high-quality parts with desired mechanical properties. Numerous studies have been conducted to tailor the crystallization behavior of PP to improve printability and mechanical performance of printed structures in extrusion-based 3D printing.[23,48,129-132] While PP crystallization in extrusion-based 3D printing has been extensively studied, [23,48,50,128-132] there remains limited research on optimizing PP crystallization specifically for the PBF process.

In this work, we present a material formulation protocol to fine-tune and understand the properties of PP powders before printing them via PBF. More precisely, a polymer blend powder that consists of polypropylene and polycarbonate is formulated to control the crystallization kinetics, crystal lamella thickness, particle size, morphology, and shape of PP powder. This protocol employs an LLPS processing method to create powders where polycarbonate (PC) is intimately blended with the PP matrix at various concentrations. Given that PC is an amorphous polymer, we anticipate significant alterations in the crystallization rate, crystal size, and thermal properties of the PP in the PP-PC blended powder relative to that in the neat PP powder. Additionally, PC is known for its high mechanical strength compared to PP, suggesting that

adding PC to PP powder could potentially enhance the strength performance of the ultimate PBF printed structures.

Using energy dispersive X-ray spectroscopy and scanning electron microscopy (SEM), we show that every single powder particle is a blend of PP and PC. The results also show that the PC content differs among the individual particles. Furthermore, SEM reveals that despite the significant differences in size and shape between PC and PP powder particles, the addition of PC does not alter the spherical shape and size of the PP particles. Examination of the Tg of the prepared powders indicates that the PP/PC blends do not form a completely miscible system. Differential scanning calorimetry and small angle X-ray scattering results show that the PP-PC blends crystalize faster and form smaller lamellae thickness than neat PP powder. Moreover, to our knowledge, this is the first example of the formation of PBF powder that consists of a polymer blend within each particle. This study, therefore, demonstrates the utility of LLPS in creating novel powder blends from immiscible polymers that can guide the processing properties of the polymer for the PBF process, thereby expanding the material options available for 3D printing applications.

Experimental Section

Materials

Bisphenol A polycarbonates (PC) and isotactic polypropylene (PP) (250,000 Daltons) pellets were purchased from 3DXTECH and Sigma-Aldrich, respectively. Xylene, ethanol, and silicone oil were purchased from Fisher Scientific. All materials were used as purchased.

PC molecular weight determination

To determine the molecular weight of the PC pellets, a Tosoh EcoSEC gel permeation chromatography (GPC) with a refractive index detector was utilized. For this experiment, PC

was dissolved in tetrahydrofuran to make a solution with a 1.5 mg/ml concentration. The GPC was calibrated with a polystyrene standard.

Powders formation via liquid-liquid phase separation (LLPS)

Neat PP, neat PC, and PP/PC blend powders were prepared from polymer pellets via LLPS. To produce neat polymer powders, 4.5 g of polymer pellets and 45.5 g of xylene were placed in a 250 ml round-bottom flask. The mixture was heated to 190 °C on a hotplate, stirred at 350 rpm, and refluxed for 1 hour for the PP-xylene mixture and 4 hours for the PC-xylene mixture to dissolve the polymer. After reflux, the mixture was transferred to a cold trap at 40 °C using a Fischer Isotemp containing 50% water and 50% ethylene glycol refrigerant and left to quench for 1 hour to precipitate the powders. PP was completely dissolved after the reflux process. However, not all the PC pellets dissolved after reflux. Therefore, the PC-xylene solution was decanted to remove the undissolved PC, and the supernatant (dissolved PC in xylene) was reheated to 190 °C before quenching. The neat PC powder preparation procedure was also applied to PP/PC blends with PC content ranging from 10 to 50 wt.%. Following quenching, the precipitated powders were separated from the xylene using vacuum filtration, and the powders were washed with ethanol three times to eliminate residual xylene. The powders were then dried to a constant mass at 40 °C in a vacuum oven. Given that not all PC pellets were completely dissolved during the reflux process, the Equation :

$$\boldsymbol{Amount\ of\ PC}\ (\%)\ \boldsymbol{in\ the\ powder} = \frac{\boldsymbol{mass\ of\ dissolved\ PC}}{\boldsymbol{mass\ of\ dissolved\ PP + mass\ of\ dissolved\ PC}} \times \mathbf{100}$$

was used to determine the polymer content in the final blend powder. In this Equation , the mass of dissolved PC was calculated by subtracting the mass of undissolved PC, determined after drying it to a constant mass, from the initial mass of PC used in the dissolution process.

Scanning electron microscopy and energy dispersive X-ray spectroscopy of prepared powders

Powder samples were sputtered with a thin layer of gold and imaged at a magnification of 500X on a scanning electron microscopy ZEISS-EVO instrument with 20.00 kV electron high tension. Energy dispersive X-ray spectroscopy (EDS) was performed on the powder samples in the above SEM using a Bruker XFlash EDS.

Measurement of powder particle size

The particle size was measured by analyzing SEM images of the powder with ImageJ software. In this analysis, each pixel was calibrated to a length scale using the scale bar on the SEM image. For each sample formation, about 20 particles were selected, and their maximum lengths were recorded.

Differential scanning calorimetry analysis

The thermal behavior of all the powder samples was measured using a differential scanning calorimetry (DSC) Q2000 from TA Instruments. For non-isothermal DSC, about 10 mg powder sample was heated from -50 °C to 200 °C at a rate of 10 °C/min and then cooled to -50 °C at 10 °C/min under a nitrogen atmosphere. In this experiment, the percent crystallinity, X_C, of the neat PP powder was calculated using:

$$\boldsymbol{Xc} = \frac{\Delta \mathbf{H}_{\boldsymbol{m}}}{\Delta \mathbf{H}_{\boldsymbol{m}}{}^{\mathbf{0}}} \times \mathbf{100}\%$$

The percent crystallinity, X_C, of PP/PC blends was calculated using:

$$\boldsymbol{Xc} = \frac{\Delta \mathbf{H}_{\boldsymbol{m}}}{\boldsymbol{\varphi} \Delta \mathbf{H}_{\boldsymbol{m}}{}^{\mathbf{0}}} \times \mathbf{100}\%$$

, where ΔH_m is the measured melting enthalpy of the prepared powder, and the melting enthalpy of fully crystalline PP material, $\Delta H_m{}^0$, is 209 J/g.[104] φ is the weight fraction of PP in the PP/PC

blend. The glass transition temperature and peak melting temperature were obtained from the DSC curves via the TA Universal Analysis software. To monitor the crystallization rate, isothermal DSC was used. In this protocol, about 10 mg powder sample was heated from 20 °C to 200 °C at a rate of 10 °C/min and equilibrated at 200 °C for approximately 3 mins and then cooled at a rate of 10 °C/min to 120°C, the crystallization temperature. The powder sample was subsequently maintained at the crystallization temperature (120°C) for 1 hour before being cooled to 20 °C at a rate of 30 °C/min. The experiment was performed under a nitrogen atmosphere.

Small angle X-ray scattering (SAXS)

The scattering experiments were conducted on a Xenocs Xeuss 3.0 x-ray scattering instrument with a Pilatus3 detector. The x-ray wavelength used was 1.54A. The sample, which was a powder, was sandwiched between Scotch tape. A blank of pure tape was also scattered, and the curve of the tape was subtracted from the scattering curve from the sample. The data was normalized by thickness, and the inherent setup of the system allows immediate normalization to absolute intensity. Scattering over both ESAXS and SAXS ranges were obtained, with detector to sample distances of 1.8m and 0.9m, respectively. The two curves were then merged with careful attention to the intensity from SAXS. The data was then analyzed using the 1-dimensional correlation function in the XSACT software. This function allows direct analysis of the lamellae spacing thickness and the crystalline phase thickness by first fitting the background to a damped Porod function, then performing the correlation function (K(z)).

$$\boldsymbol{K(z) = \frac{\int 4\pi q^2 * I(q) * \cos(q * z) dq}{\int_0^{\infty} I(q) * q^2 \, dq}}$$

This analysis is applied to the raw data, then the resulting curves for the smoothened data and the raw data are compared until they overlap. At that point, the initial peak is taken as the lamellae

spacing (Lp), and the x-axis intercept of the linear fit of the resulting curve is the crystalline phase thickness (Lc). The crystalline ratio is then found from the ratio of the two (crystalline ratio = Lc/Lp).

Results and Discussion

SEM images and size of powder particles formed by the LLPS process

As discussed above, the shape and size of powder particles impact the particle flowability in the initial stage of the PBF process, powder recoating. Therefore, it is crucial to evaluate the powder particle size and shape to determine their suitability for the PBF process and achieve successful printability. **Figure 32** presents the SEM images of neat PP, neat PC, and blended PP/PC powders. The powders formed from neat PP and the PP/PC blend exhibit a similar shape: spherical and regular. In contrast, the powders formed from neat PC have non-spherical, elongated, and irregular shapes. The average particle sizes of the neat PP and the neat PC powder particles are ~ 49 μm and 97 μm, respectively. The average particle sizes of blend powders formed from the PP/PC blends range between 40 -51 μm. These powder particle sizes are in the range of particle size that is desirable for the PBF process.[80]

Interestingly, despite the substantial difference in size and shape of neat PC powder particles relative to the neat PP powder particles, the addition of PC to PP does not significantly alter the size and shape of the particles in the blended powders. This suggests that PP drives the formation of powders in the blend. The formation of polymer particles in the LLPS process is primarily governed by droplet coalescence.[13,28] While the results in **Figure 32** suggest that PP drives the formation of powders in the blend, the exact mechanism leading to the similarity in structures observed in both the neat PP and PP/PC blend particles remains unclear. However, one possible explanation is that that phase separation of PP occurs first, which then drives the PC to simultaneously phase separate along with it.

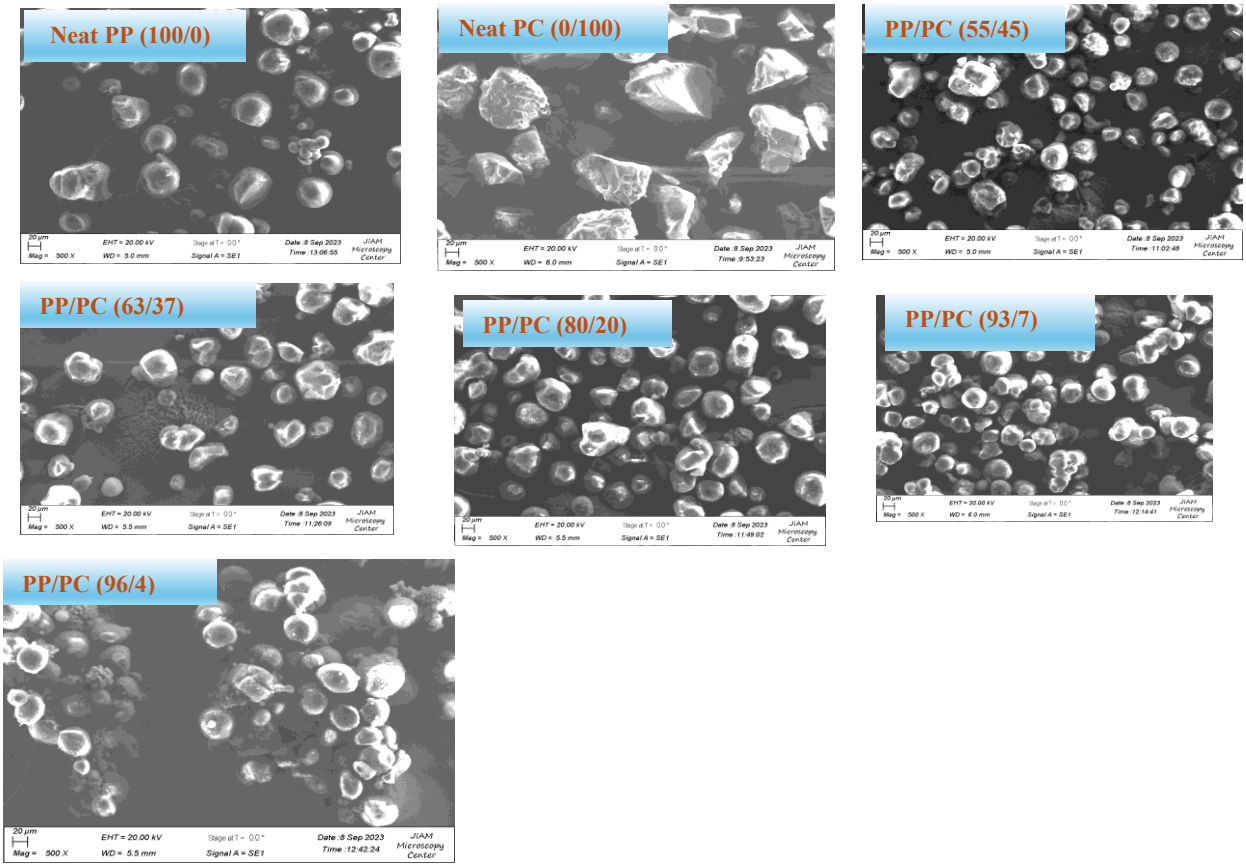

Figure 32. SEM images of neat and blended powders formed from LLPS

Energy dispersive X-ray spectroscopy of prepared powders

Dissolving PP/PC polymers in xylene at elevated temperature and quenching the solution to induce phase separation to form PP/PC blend powder involves complex interactions that can significantly impact the morphology of the resulting powder particles and the distribution of the polymer components within the blended powder. Identifying the presence and distribution of individual polymers in the blended powder is essential to understand the dispersion of the individual polymers within the blend powders at the molecular level. Thus, energy dispersive X-ray spectroscopy (EDS) is performed on the powders to address fundamental questions, such as whether every powder particle is pure PP and pure PC or each powder particle contains a mixture of PP and PC. **Figure 33** shows the SEM and the EDS spectra of the powder formed from neat PC, neat PP, and 55/45 PP/PC blend powder. Approximately 20 individual powder particles were analyzed for each sample, as shown in **Figure 33**. As expected, neat PC powders have pronounced oxygen signals at 0.525 keV. Examination of the SEM-EDS of the powder formed from the blend shows the presence of oxygen peaks in the EDS spectra for all particles examined in the blend. This indicates that the PC is distributed among all particles throughout the sample. Interestingly, neat PP also shows a small, baseline signal at 0.525 keV despite no oxygen in the PP chemical structure. These signals are taken to represent the background intensity of PP. Consequently, the EDS intensities at 0.525 keV for powder particles formed from neat PP and PP/PC blends are analyzed and compared, where the intensity in each particle at 0.525 keV is plotted in **Figure 34.** Inspection of **Figure 34** shows that for every particle analyzed in the blend, there is a distinct intensity at 0.525 keV, signifying the presence of PC in each powder. Moreover, for every particle analyzed in the blend, the intensity at 0.525 keV is always higher than the background intensity of PP, confirming that PC is present in all particles. Therefore,

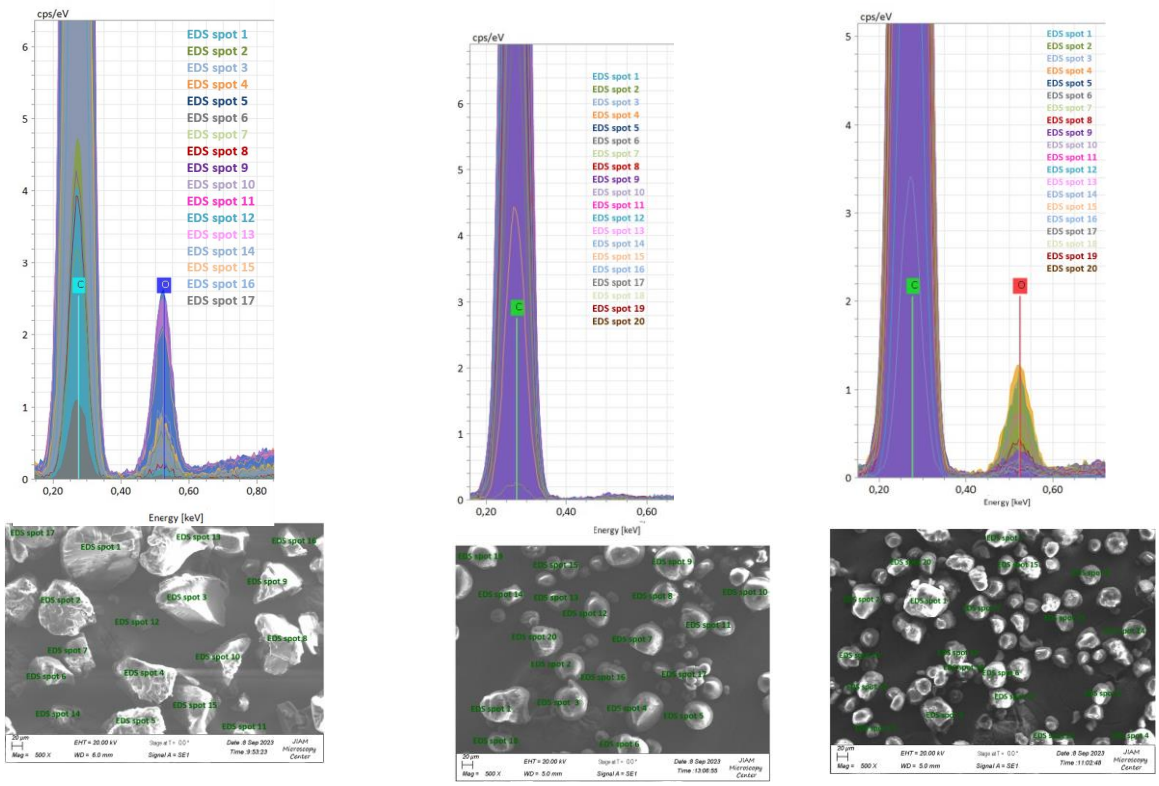

Figure 33. SEM-EDS of prepared powders. (a) neat PC, (b) neat PP, (c) PP/PC blend (55/45)

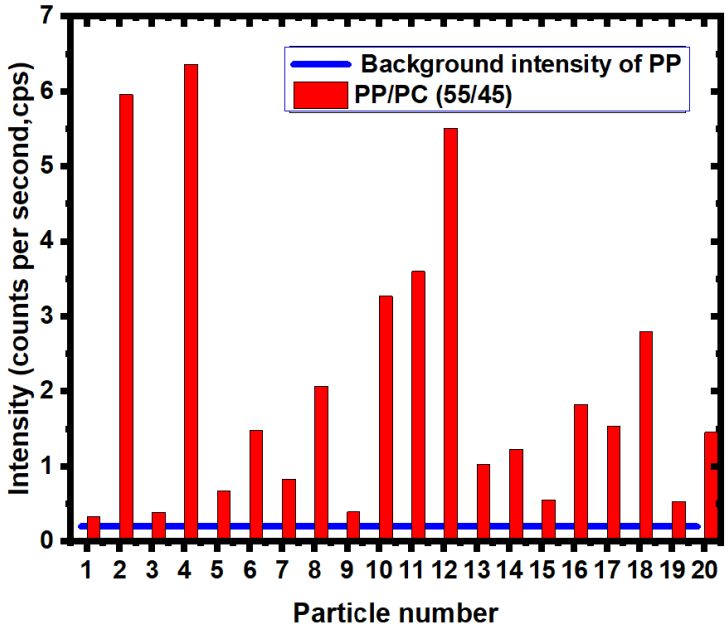

Figure 34. Comparing EDS intensities at 0.525 keV for powder particles formed from neat PP and PP/PC blend

SEM-EDS provides a mechanism to qualitatively assess the distribution of the PC in the blend and demonstrates that every powder particle in the blend is a mixture of PP and PC.

Examining the glass transition temperature of the powder

To gain deeper insights into the phase behavior of the powder, the glass transition temperature (Tg) of the samples were investigated. The formed powder is a mixture of two polymers that may exist in any of the four states of miscibility depicted in **Figure 35**. Measuring the blend composition dependence of the Tg of the powder provides insight into the phase behavior of these powders. For instance, in the case of an immiscible blend where each powder particle consists of pure polymer (case 1), the blend will exhibit two distinct Tgs that are similar to those of the constituent polymers in the blend. In the scenario where PP and PC are completely miscible (case 3), a single Tg will be observed, where Tg will be between those of the two pure polymers and will fit a predictive model such as the Fox equation. A partially miscible blend (case 2) will exhibit two Tg values that are also intermediate to those of the constituent polymers, but do not fit the predictive model. Finally, in case 4, where polymers are immiscible in the same particle, two Tg values closely resembling those of the individual polymers in the blend will be found. The SEM-EDS result provides the foundation to eliminate case 1 morphology, as those results clearly show that each particle contains both PC and PP.
To determine whether the powder structure is case 2, case 3, or case 4, the Tgs of the samples were determined via differential scanning calorimetry (DSC), where the DSC curves are shown in **Figure 36**, and the Tg values are presented in **Table 3**. Interestingly, **Figure 36** reveals that both the neat polymers and the powder blends display a single Tg. The presence of a single Tg in the blend raises the question of whether the PP and PC form a fully or partially miscible blend. As the Tg of a miscible blend will fit a predictive model, the experimental Tgs were fitted to the Fox model, which is given in the following Equation:[65,66]

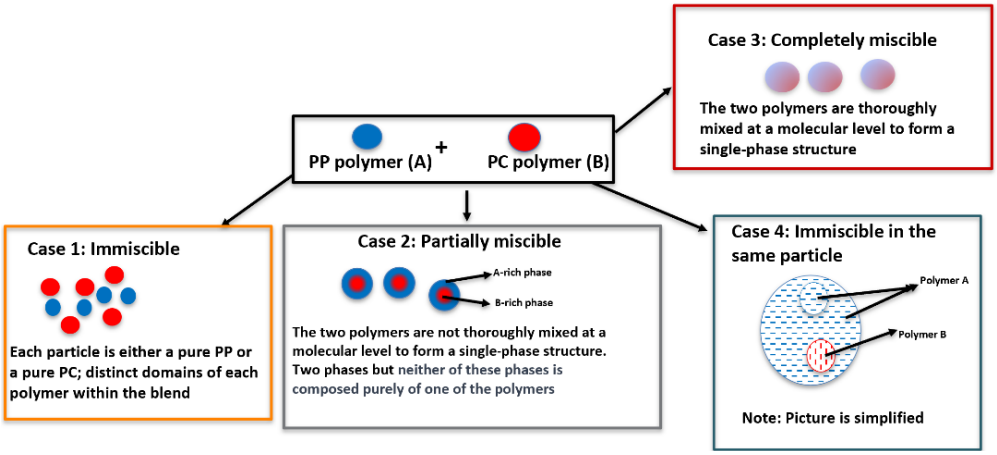

Figure 35. Illustration of the Four possibilities for PP/PC powder

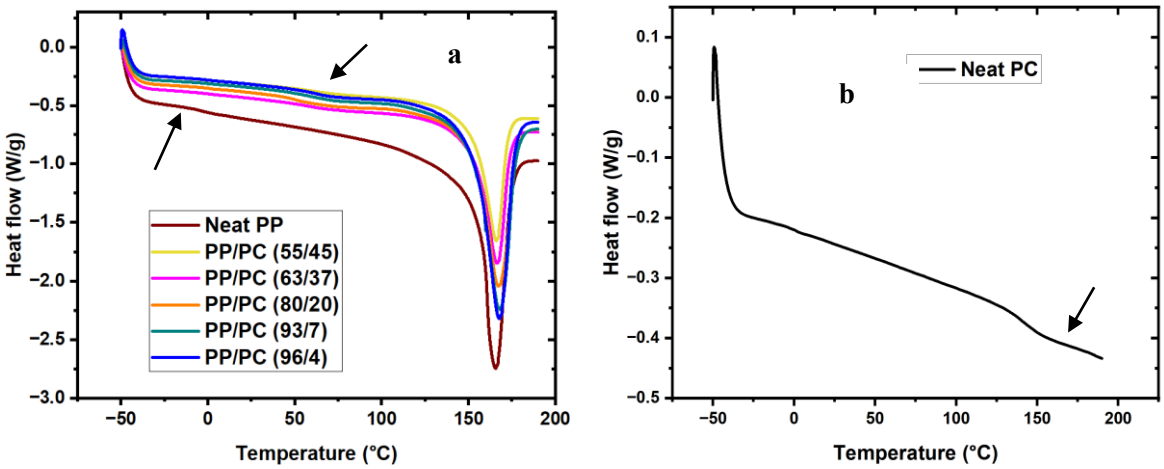

Figure 36. DSC curves for determining Tg (a) DSC curves for neat PP and PP/PC blends, (b) DSC curve for neat PC.The arrow in the DSC curves indicate the location where Tg is determined.

Table 3. Tg of powders formed from LLPS process.

Samples	Tg (°C)
Neat PP (100/0)	-16.5
PP/PC (96/4)	48.3
PP/PC (93/7)	50.6
PP/PC (80/20)	57.4
PP/PC (63/37)	61.1
PP/PC (55/45)	67.5
Neat PC (0/100)	148.7

$$\frac{\mathbf{1}}{\boldsymbol{Tg_b}} = \frac{\boldsymbol{w_1}}{\boldsymbol{Tg_1}} + \frac{\boldsymbol{w_2}}{\boldsymbol{Tg_2}}$$

, where w_1 and w_2 are the amorphous weight fractions of PP and PC, respectively. Tg_1 and Tg_2 are the Tg of neat PP and neat PC, respectively, and Tg_b is the Tg of the blend. It is important to remember that the Tg is only relevant for the amorphous part of the polymer. Given the fact that PP is semi-crystalline, the composition of the amorphous phase is not that of the blend. Therefore, the compositions of the amorphous phase must be calculated to be used in the Fox model. This is determined via the following Equations:

$$\boldsymbol{w_2} = \frac{\boldsymbol{mass\ of\ PC}}{\boldsymbol{mass\ of\ PC + mass\ of\ amorphous\ PP}}$$

$$\textbf{Mass of amorphous PP} = \textbf{mass of PP} \times (\mathbf{1} - \%\ \textbf{crystallinity})$$

$$\boldsymbol{w_1} = \mathbf{1} - \boldsymbol{w_2}$$

, where the composition of the amorphous phase (w_1 and w_2) are presented in **Table 4**. **Figure 37** plots the dependence of the experimental Tg of the blend and that of the Fox equation using the amorphous weight fraction of PC as presented in **Table 4**. Inspection of this figure shows that the Fox model significantly underestimates the Tg of the blend. This indicates that the blend is not a miscible blend of the PC and the PP. This leads to the conclusion that the polymer blend particles are forming a partially miscible system, case 2 in **Figure 35**.

Impact of PC on the crystallization behavior of PP/PC blend particles

Impact of PC on the crystallization rate of PP

The presence of the PC in the PP/PC blend powders will alter the crystallization behavior of PP, as the presence of PC may hinder or promote the crystallization kinetics of PP. To examine the impact of the PC on the PP crystallization kinetics, the isothermal crystallization of the neat

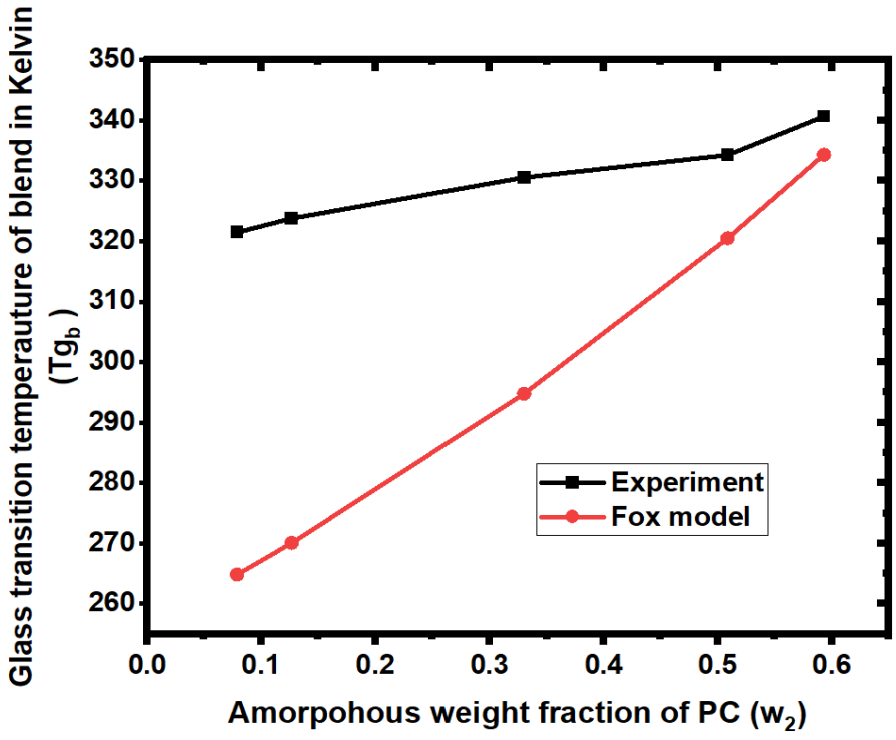

Figure 37. Comparing experimental Tg to Fox model.

Table 4. Amorphous weight fractions of PP and PC used in the Fox model

Samples	Weight fraction of PC (w_2)	Weight fraction of PP (w_1)
PP/PC (96/4)	0.08	0.92
PP/PC (93/7)	0.13	0.87
PP/PC (80/20)	0.33	0.67
PP/PC (63/37)	0.51	0.49
PP/PC (55/45)	0.59	0.41

PP and PP/PC blended powders was monitored with DSC, and their crystallization kinetics were evaluated using the Avrami Equation:[53-56]

$$\boldsymbol{X\,(t) = 1 - e^{-Kt^n}}$$

In the Avrami Equation, X(t) is the percent crystallinity of PP, t is crystallization time, n is the Avrami exponent, and K is the crystallization rate constant. X(t) can be expressed in terms of the heat generated as a function of crystallization time t(Q_t), the heat generated at infinite time (Q_∞), and heat evolution rate $\left(\frac{dH}{dt}\right)$, as shown in the following Equation:[53-56]

$$\mathbf{X(t) = \frac{Q_t}{Q_\infty} = \frac{\int_0^t \left(\frac{dH}{dt}\right) dt}{\int_0^\infty \left(\frac{dH}{dt}\right) dt}}$$

Both Q_t and Q_∞ are obtained from the integration of crystallization peak in the DSC curves. Applying logarithms to both sides of Avrami equation , the Avrami equation can be rewritten as follow:

$$\mathbf{log\left[-ln\left(1 - X(t)\right)\right]} \;\; = \boldsymbol{n}\mathbf{logt} \; + \; \mathbf{logK}$$

Thus, plotting log[-ln(1-X(t))] as a function of log (t) provides a straightforward analysis to determine the Avrami exponent from the slope of the line, and the crystallization kinetic constant from the intercept with the y-axis.[53] The crystallization rate constant and Avrami exponent can also be expressed in terms of crystallization half-time, $t_{1/2}$, as shown in the follwing Equation:

$$\boldsymbol{t_{1/2}} = \left(\frac{\mathbf{ln2}}{\mathbf{K}}\right)^{\frac{1}{n}}$$

,where $t_{1/2}$ is the time at which crystallinity reaches 50%. Consequently, a higher $t_{1/2}$ value indicates a slower crystallization rate.[53,54] **Figure 38** shows the relative crystallinity as a function of crystallization time for the neat PP and blended PP/PC powders. **Table 5** provides the Avrami

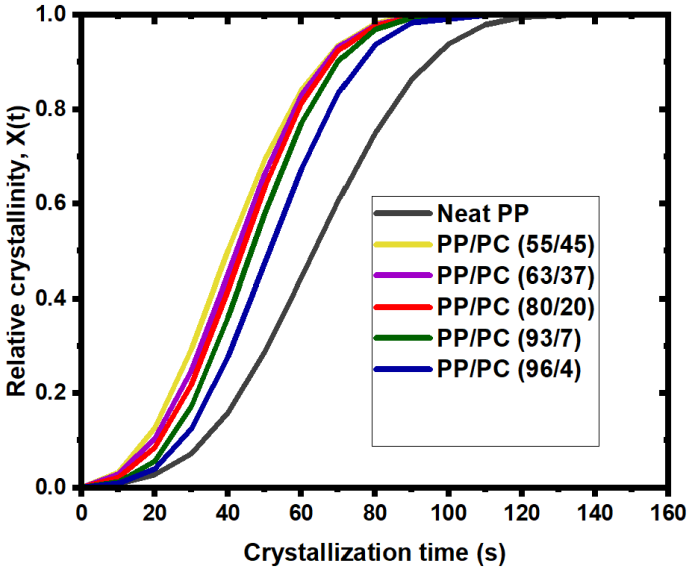

Figure 38. Relative crystallinity as a function of crystallization time of the prepared powder samples

Table 5. Avrami exponent, crystallization kinetic constant, and crystallization half-time of the powders formed from LLPS.

Samples	Avrami exponent, n	Crystallization rate constant, K (s^{-1})	Crystallization Half-time, $t_{1/2}$
Neat PP (100/0)	2.75	8.7×10^{-6}	60.6
PP/PC (96/4)	2.84	1.0×10^{-5}	50.6
PP/PC (93/7)	2.8	1.6×10^{-5}	45.3
PP/PC (80/20)	2.56	4.8×10^{-5}	42.2
PP/PC (63/37)	2.42	8.8×10^{-5}	40.7
PP/PC (55/45)	2.38	1.2×10^{-4}	38.1

exponent, crystallization rate constant, and crystallization half-time the of these powders. Assessment of **Figure 38** and **Table 5** shows that the addition of PC to PP results in faster crystallization. Moreover, as the PC content increases, the crystallization rate increases. The increase in the PP rate of crystallization may be attributed to changes in blend viscosity with the addition of PC. The molecular weights of the PC and PP pellets used in forming these powders are 36 kDa and 250 kDa, respectively. The molecular weight of PP is approximately 7 times higher than that of PC, indicating that PC has shorter chains and less chain entanglement. Consequently, when mixed, PC can act as a plasticizer for the higher molecular weight PP, reducing the overall viscosity of the blend. Increased polymer chain mobility impacts the crystallization rate by enabling polymer chains to more quickly assemble into ordered structures. Thus, the plasticizing effect of the PC will enhance the movement of polymer chains into growing crystalline regions, and promoting faster crystal growth.[51,57] We interpret that the more rapid crystallization observed in the PC/PP blend powders may be attributed to the reduction in the blend viscosity, which potentially enhances polymer chain mobility and accelerates crystallization. Furthermore, since viscosity is concentration-dependent, the viscosity of the blend likely decreases with increasing PC content, leading to a higher crystallization rate as the PC content increases in the blend.

Further examination of **Table 5** reveals a slight change in the Avrami exponent with blend composition, where *n* ranges from approximately 2 to 3. The Avrami exponent provides information on the type of nucleation mechanism and geometry of the crystal growth. Therefore, changes in the Avrami exponent with blend composition suggests a change in the nucleation mode and crystal geometry. Crystallization begins with a nucleation process and progresses through crystal growth.[51,52] When all nucleation centers emerge simultaneously at the outset, it is termed instantaneous nucleation. In contrast, if nuclei appear as a function of time throughout the

polymer volume, it is referred to as sporadic nucleation.[52] The Avrami exponent, n, indicates the dimensionality of crystal growth: n =1 corresponds to one-dimensional crystal growth, such as rods; n =2 to two-dimensional crystal growth, like disks; and n =3 to three-dimensional crystal growth, such as spheres.[55-57] Relating this fundamental information to the Avrami exponent of the powders presented in **Table 5**, it is clear that the powder samples undergo either instantaneous nucleation or sporadic nucleation, forming crystals with circular or spherical geometry.

Impact of blend composition on percent crystallinity, melting temperature, and crystal structure of PP

The percent crystallinity of the powders and the peak melting temperature obtained from DSC curves are plotted as a function of PC content in the blend in **Figure 39**. Upon inspection of **Figure 39**, it is evident that adding PC to PP results in a decrease in both percent crystallinity and melting temperature. This reduction is attributed to the presence of PC chains, which limit the formation of crystalline regions in the PP.

One of the goals of this study is to control the crystal lamella thickness of the PP powder, as the crystal size in the powder can impact the required melting during the powder bed fusion process. As previously discussed, thicker lamellae in the powder can result in only partial melting by the laser, which will limit polymer chain mobility during coalescence and result in poor mechanical performance of the printed structures.

Thus, small angle x-ray scattering (SAXS) was performed on the powders to determine the lamellar structure in the powder particles **Figure 40** shows the thickness of the lamellae in the powder obtained from the SAXS experiment. As illustrated in **Figure 40**, the size of PP lamellae, and consequently the crystal size, significantly decreases with the addition of PC. Thus, we expect the decrease in lamellae size in these powder particles to benefit the PP powder

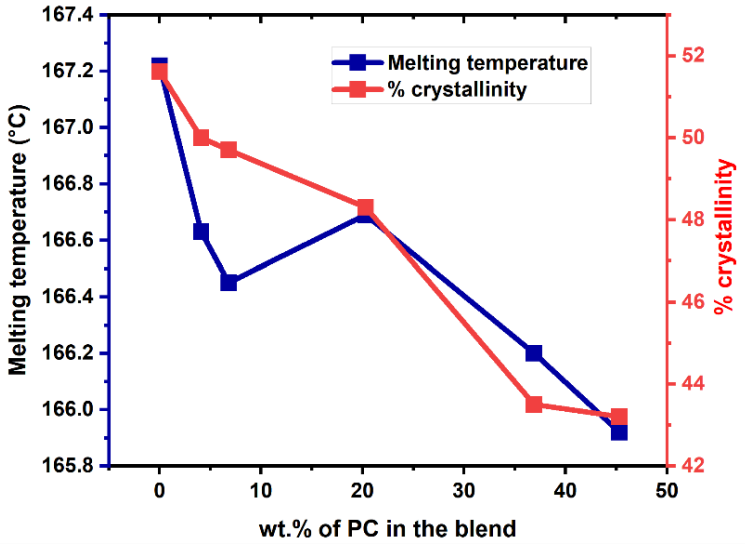

Figure 39. Percent crystallinity and melting temperature of prepared powders as a function PC content in the blend

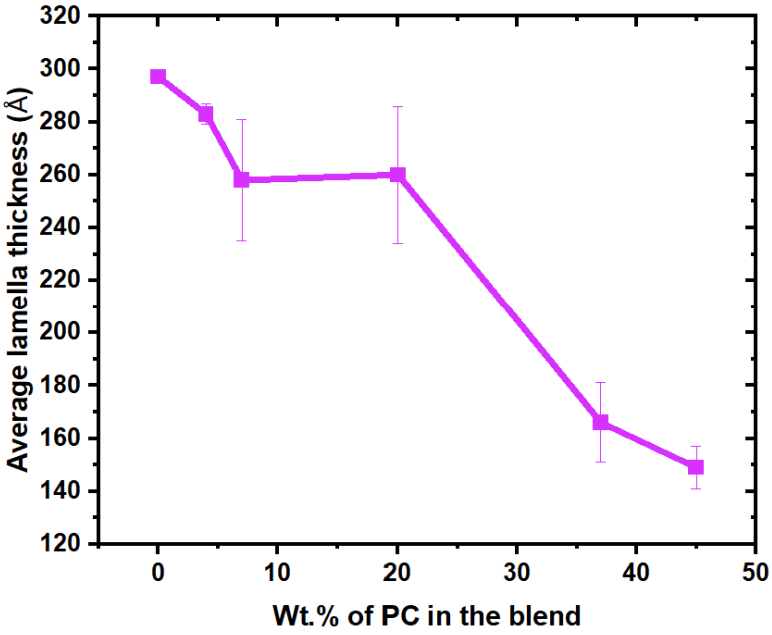

Figure 40. Lamellae thickness of the prepared powders as a function of PC content in the blend

bed fusion process by enhancing melting efficiency, enabling particle coalescence, resulting in better quality and mechanical performance of the final printed parts.

Conclusion

This research program employed a liquid-liquid phase separation (LLPS) to create powders that are tailored for polymer powder bed fusion (PBF) that consist of a blend of polycarbonate and polypropylene in each particle. Analysis of the resultant powders shows that incorporating PC into the opowder with the PP does not significantly alter the shape and size of powder particles, suggesting that PP predominantly controls particle formation in the LLPS process. Energy dispersive X-ray spectroscopy confirmed the presence of an oxygen peak in all particles analyzed, indicating that the PC and PP exist in each particle. Analysis of the phase behavior by monitoring the glass transition temperature revealed significant discrepancies with the Fox model, suggesting partial miscibility between PP and PC during the LLPS process. Moreover, investigation into crystallization behavior and crystal structure showed that adding PC accelerates the crystallization of the PP, leading to decreased percent crystallinity and thinner lamellae. The increased crystallization in the blend is likely facilitated by reduced PP viscosity, enhancing polymer chain mobility and nucleation rates. The reduction in lamella thickness could be due to the presence of PC chains reducing the opportunity for larger crystalline lamellae to form during the crystallization process of PP. These insights into the properties of PP-PC blended powders are crucial to optimize their processability in the PBF process. To our knowledge, the formation of PP-PC powders through the LLPS process and their application in the PBF process have not been reported previously. We anticipate the newly designed PP/PC feedstocks to broaden the range of materials available for the PBF process. Future research will focus on printing the powder samples via PBF to investigate the impact of PC on the quality and mechanical performance of PP printed parts.

Chapter 5: UV Light Exposure Modifies the Molecular Weight Characteristics and Improves the Melt Extrusion Additive Manufacturing of Polycarbonate

A version of this chapter was published by Akan A. George and Mark D. Dadmun: George, A. A.; Dadmun, M. D. "UV Light Exposure Modifies the Molecular Weight Characteristics and Improves the Melt Extrusion Additive Manufacturing of Polycarbonate." *ACS Applied Polymer Materials*, **2024**, 6, 20, 12559–12567, 10.1021/acsapm.4c02110

Abstract

Bisphenol A polycarbonates (PC) are among the important engineering thermoplastics utilized as feedstocks for melt extrusion additive manufacturing, including fused filament fabrication (FFF). However, limited diffusion of polymer chains between adjacent layers and complex thermal histories encountered during the printing process lead to poor interlayer adhesion, residual stress, and voids in the printed parts, which in turn leads to poor mechanical performance and mechanical anisotropy. To address these issues, our group has modified an FFF printer by integrating an ultraviolet (UV)-LED optical fiber into the printer head. This modification allows for real-time illumination of the printed structure during the deposition process, enabling a thorough investigation into its impact on the FFF process and the properties of the resulting printed parts. Examination of the mechanical behavior and fracture surfaces of the printed parts shows that PC printed with UV light attains higher toughness both in the transverse and longitudinal directions, as well as decreased void space compared to PC printed without UV light. Careful analysis of the molecular weight characteristics of the printed parts shows that PC printed with UV light has a slight decrease in *average* molecular weight and a broader molecular weight *distribution* compared to PC parts printed without UV light. This indicates that the polymer chain scission upon UV light exposure leads to the formation of shorter polymer chains and broader range of chain sizes, which in turn increases in the toughness of the UV-light-printed PC. These observations are interpreted to indicate that the change in molecular weight *distribution* upon UV illumination fosters improved interfilamentous diffusion,

consequently lowering the interlayer voids, and thus enhancing the mechanical performance. These findings therefore provide foundational insights into how UV light can be used to tune the molecular weight distribution of the polymer and thus impact the FFF process, offering a distinctive and straightforward strategy to tune the properties of parts created by extrusion additive manufacturing of a range of thermoplastics.

Introduction

Fused filament fabrication (FFF) is an additive manufacturing (AM) technique that enables rapid object design and prototyping with large-scale manufacturing capabilities.[30] The print process of FFF begins by using computer aided design software to create a 3D model of the desired structure.[3,10] The 3D model of the desired structure is then sliced into thin layers using slicing software, which generates G-code that the printer reads to fabricate the desired structure in a layer-by-layer fashion.[3] FFF uses polymeric filament in the printing process, where the thermoplastic filament is passed through a heated nozzle, heated to a molten state and then extruded via a 3D printer nozzle. The movement of the 3D printer nozzle head deposits the extruded material on the build plate according to the G-code instructions for a given layer. The print head then moves up to deposit subsequent layers. This layer-by-layer process continues until the required object is completely fabricated.[3,10]

FFF technology offers a rapid method to create complex objects with low cost and design flexibility. However, major shortcomings of the layer-by-layer process of creating 3D printed parts include lack of part reliability[30] and anisotropic mechanical performance, where longitudinally printed parts exhibit significantly higher mechanical properties compared to parts printed in a transverse orientation.[8] These shortcomings are associated with the complex shear and thermal histories the filament experienced due to the layer-by-layer deposition process of FFF.[8,10,30] As molten filaments are deposited onto previously deposited solidified layers, a

conductive heat transfer to the bottom portion of the print occurs.[30] This initiates repetitive heating-cooling cycles and a thermal gradient that intensifies as the print increase in height along the perpendicular direction, the z-axis.[10,30] This dynamic and variable nature of the temperature profiles experienced by the printed material during the printing process results in residual stress[30] and limited diffusion of polymer chains between adjacent layers,[10] leading to poor interlayer adhesion and formation of large voids between solidified layers. Also, the layer-by-layer deposition process of FFF reduces the interaction of polymer chains between adjacent layers, limiting chain entanglement between subsequent printed layers, and consequently, resulting in inadequate welding and weak interfaces.[8,59] Poor inter-filament bonding, residual stress, large voids between fabricated layers and poor chain entanglement between filaments results in anisotropic behavior, poor mechanical performance of the printed parts, and lack of part reliability.[8-10,30,58,59]

In addition to the complex thermal history affecting the interlayer adhesion, several print parameters such as the print temperatures, print orientation, print speed, and layer height have been shown to influence the welding of adjacent layers during the printing process, which in turn affects the resulting mechanical performance of the printed structure.[134-138] Numerous research endeavors have focused on the optimization of these print parameters as strategic approaches to alleviate anisotropic behavior and improve mechanical performance of FFF printed samples. Despite efforts to optimize these parameters, the reduction in anisotropy and overall improvement in part properties remain limited.[10,31,139] In fact, optimizing a set of parameters to enhance one specific property can lead to a deterioration of other printed part properties and compromise other aspects of the printing process. For instance, aiming for minimal dimensional error and surface roughness, lower extruder temperatures or the implementation of active cooling are recommended. However, such adjustments can diminish the overall strength of the part due

to a reduction in interlayer bond strength.[139] Similarly, reducing layer thickness may improve bonding but at the expense of increased printing time.[139,140]

Consequently, recent research has shifted focused towards material designs and slight modifications of the printing process as more promising routes for increasing interfilamentous adhesion, mitigating structural anisotropy, and improving the mechanical properties of final printed parts. This methodology entails manipulating the filament by introducing low molecular weight polymers,[8,58,59] incorporating additives like graphene,[9] or utilizing crosslinking agents.[10,141,142] However, a constraint associated with material design is the intricate synthesis process, which may prove to be both expensive and time-consuming. Additionally, incorporating crosslinkers in the FFF process may require specific delivery steps to the interfilamentous interface, which can add complexity to the printing process. For example, in a study by Perryman et al., multi-amines crosslinkers were deposited during the fabrication process by applying crosslinker solutions to the central layers of the printed sample during printing. This was achieved by soaking cotton swabs in the crosslinker solution and then manually painting the crosslinker solutions onto the filament.[10] These limitations underscore the need for research to simplify material design to improve the manufacturing efficiency in the FFF process and the resulting mechanical behavior of the fabricated structures.

In this study, we identify a promising avenue for improving the properties of polycarbonate (PC) printed by the FFF process, where synthesis of additional materials, utilization of additives, or crosslinkers are not needed. PC is an engineering thermoplastic known for its high impact strength, temperature resistance, excellent dimensional stability, transparency, and resistance to creep.[143,144] It finds widespread application across various industrial sectors due to these desirable properties. **Figure 41** illustrates the chemical structure of PC. In this research, we investigate the efficacy of ultraviolet (UV) in-situ illumination of PC to enhance polymer chain

diffusion and adhesion throughout the printing process, aiming to potentially minimize anisotropy and enhance the mechanical integrity of the printed parts.

As shown in **Figure 41**, PC possesses functional groups, including carbonate groups and isopropylidene linkages, which serve as potential reactive sites for various chemical processes, particularly when exposed to external stimuli such as thermal energy and UV radiation.[145-149] Numerous studies have shown that exposing PC to UV irradiation at elevated temperatures can lead to direct cleavage of the CO-O bond, generating phenoxyl (R^1) and carboxyl radicals (R^2).[148,150-152] These radicals readily undergo further chemical reactions, including hydrogen abstraction, decarbonylation, decarboxylation and combination, resulting in the formation of various new functional groups and oligomers, as summarized in **Figure 42**.[148,150-152]

The diffusion of polymer chains plays a significant role in FFF 3D printing, influencing various aspects of the printing process and the properties of the printed components. For example, improved polymer diffusion is essential to enhance interlayer adhesion, expedite interfilament coalescence, and minimize void spaces between layers during the deposition process.[8,30,58,59,153-157] Polymer chain diffusion is a crucial molecular level process to form strong adhesion between layers. Coalescence of adjacent filaments occurs through viscous flow and molecular diffusion of the polymer chains.[155] The bonding strength between adjacent filaments depends on the neck size formed during coalescence and the extent of chain entanglement.[156,157] Faster molecular diffusion between adjacent filaments leads to larger neck sizes, resulting in stronger adhesion between the filaments. Moreover increasing the neck size and improving entanglement across interfilament interfaces reduces interfilament voids, further strengthening

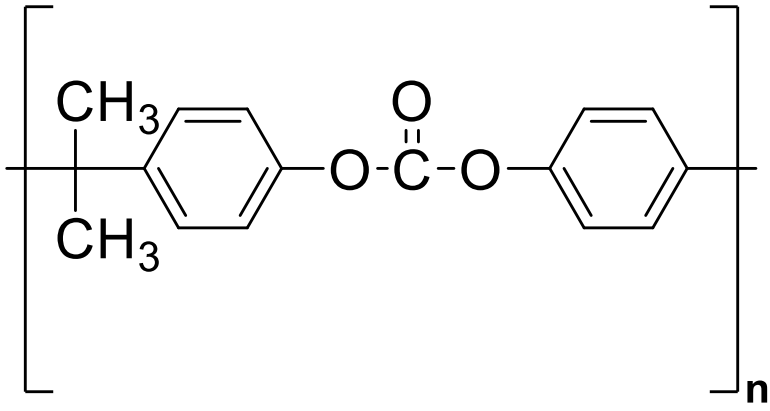

Figure 41. Chemical structure of bisphenol-A polycarbonate (PC).
n is the number of repeating units in the polymer chain

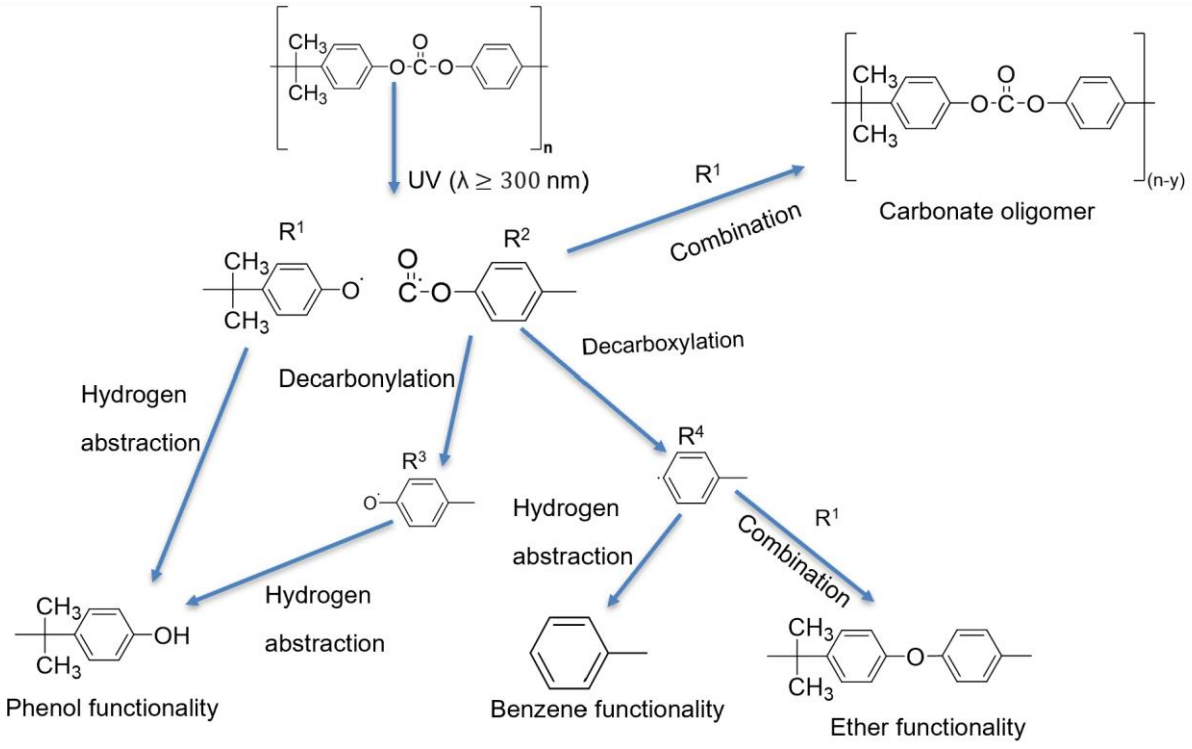

Figure 42. Photodegradation of PC, leading to the formation of various smaller molecules. R^1, R^2, R^3, and R^4 are phenoxy, carboxyl, phenoxy, and phenyl radicals, respectively. n is the number of repeating units in the polymer chain. y is the number of repeating units that have been removed from PC during degradation.

the FFF-printed structures.

It is well established that small polymer chains diffuse more quickly compared to their larger counterparts, where the diffusion coefficient (D) of a polymer is inversely related to the square of its molecular weight (Mw), as shown in the following Equation:[47]

$$D \sim Mw^{-2}$$

Consequently, under the same condition, smaller chains move significantly faster than their larger counterparts. Moreover, the distance ($\bar{x}^2$) that the center of mass of a polymer chain diffuses in 3 dimensions over a period of time (t) is related to the diffusion coefficient, as shown in the follwing Equation:[46]

$$\bar{x}^2 = 6Dt$$

The Equations above offer a quantitative understanding of how the size of polymer chains can impact the FFF process, where, under the same experimental condition, larger polymer chains require more time to diffuse across or between interlayer interfaces and travel a shorter distance than smaller polymer chains over the same time period.

From this background knowledge, we hypothesize that printing PC via FFF at elevated temperature under UV light radiation will alter the molecular structure of the PC, such as a decrease in its molecular weight (Mw) and alterations in its Mw distribution due to chain scission. This process generates a range of chain sizes that could facilitate diffusion and enhance interlayer adhesion during the FFF process. Therefore, in this study, we will examine the impact of UV-light exposure on the structure, and properties of polycarbonate structures printed by FFF. Providing an understanding of molecular-level processes that are altered by UV-light exposure which govern interlayer adhesion will establish foundational knowledge to formulate polymeric

materials for improved properties of parts fabricated by additive manufacturing. Moreover, the strategy described in this work presents a cost-effective approach to tune properties of printed parts in FFF process, offering an economically viable alternative to material design methods involving intricate synthesis procedures.

Experimental section

Polycarbonate filament preparation

Polycarbonate (PC) pellets purchased from 3DXTECH were dried under vacuum at 110℃ prior to use. These dried pellets were then processed into filaments using a Filabot EX6 single screw extruder. Extrusion temperatures for the front, middle, and back heating zones of the extruder were set to 220℃, while the feed zone temperature was set to 50 ℃. The resulting filaments were extruded to a diameter of 2.70 ± 0.10 mm.

Sample printing, tensile specimens' preparation, and tensile testing

The prepared filament was fed into a LulzBot TAZ 5 3D printer with a 0.5 mm nozzle to print cubes. The printed cube has dimensions of 70 mm × 70 mm × 20 mm, with a wall thickness of 3.58 mm. Printing parameters included a nozzle temperature of 290˚C, a bed temperature of 135˚C, a layer height of 0.3 mm, and an infill density of 100%, with a print speed of 60 mm/s. After printing, cubes were allowed to cool to room temperature before removal from the print bed. Dogbone tensile bars, adhering to the ASTM D638-V standard, were cut from the printed cubes using an OMAX 2626 waterjet cutter. The dogbones were cut in two orientations as shown in **Figure 43**, where the filament orientation in the final dogbone is either transverse or longitudinal to the print direction. To establish statistically relevant results, a minimum of two cubes were printed, and at least 10 tensile bars were generated for each test. The dogbones were dried under vacuum at 110℃ overnight, and subsequently, their tensile properties were determined via an Instron 5965 machine with an extension rate of 1.00 mm/min. For samples

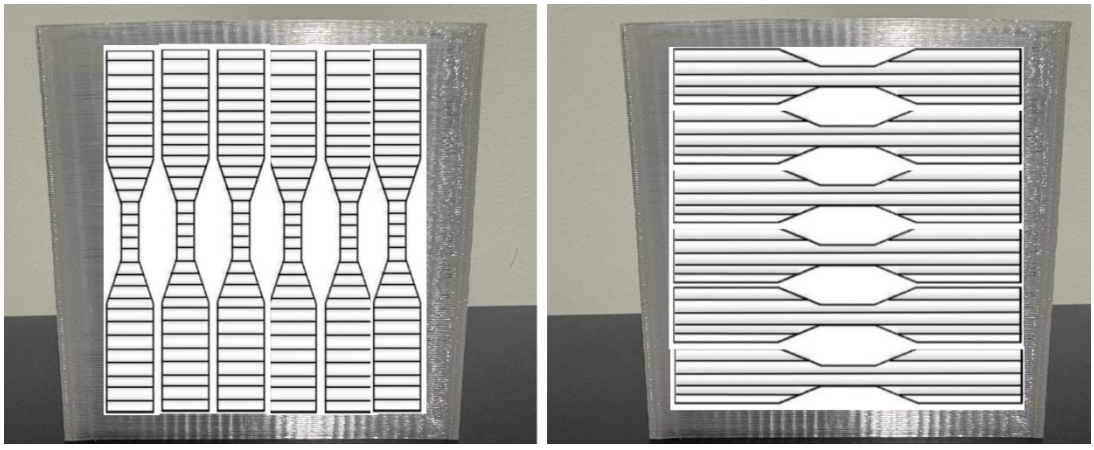

Figure 43. Photo of the printed cube with an overlaid schematic of the dogbone tensile bars as they are cut from the cube wall. The specimens on the right were cut with filament orientation parallel to the print direction, (longitudinal), while those on the left were cut with filament perpendicular to the print direction (transverse)

printed under UV light, the same procedures were followed, with the addition of an LED fiber optic cable connected to the printer head to irradiate the structures with UV light (λ = 365 nm) during the deposition process, as illustrated in **Figure 44**. For this experiment, a Thorlabs M365FP1 fiber-coupled LED paired with an LEDD1B driver is used. The fiber delivers a minimum power output of 9.8 mW at a drive current of 1400 mA. During the printing process, the fiber optic is positioned approximately 0.8 cm from the sample. Irradiation occurs directly on the filament below the printer nozzle, where the filament is extruded and deposited, as shown in **Figure 44**. UV light irradiates the PC sample throughout the entire printing process. The UV exposure time for any specific section of the print during the deposition process is approximately 2 seconds. The irradiance at the sample surface during the deposition process is approximately 0.063 W/m² and was measured using a Fisher Scientific traceable calibrated light meter. The integration of UV light into the FFF printer does not require significant alterations to the printer head. Importantly, the heat generated during printing does not affect the UV light fiber, ensuring practicality and efficiency.

Molecular weight characterization

The molecular weight and dispersity of the bulk PC samples were determined by gel permeation chromatography using a Tosoh EcoSEC equipped with a refractive index detector. In this analysis, tetrahydrofuran is the eluent and a PC solution concentration of 1.5mg/ml was used. All molecular weights are reported relative to a calibrated polystyrene standard.

Void space analysis via scanning electron microscopy

The fracture surfaces of the PC dogbones were imaged to visualize the voids between the printed layers using a ZEISS-EVO scanning electron microscopy (SEM) with a high electron tension set at 5.00kV. Prior to imaging, the fracture surfaces were sputter coated with gold to eliminate surface charging. The images were magnified between 33 and 200 X, with a working

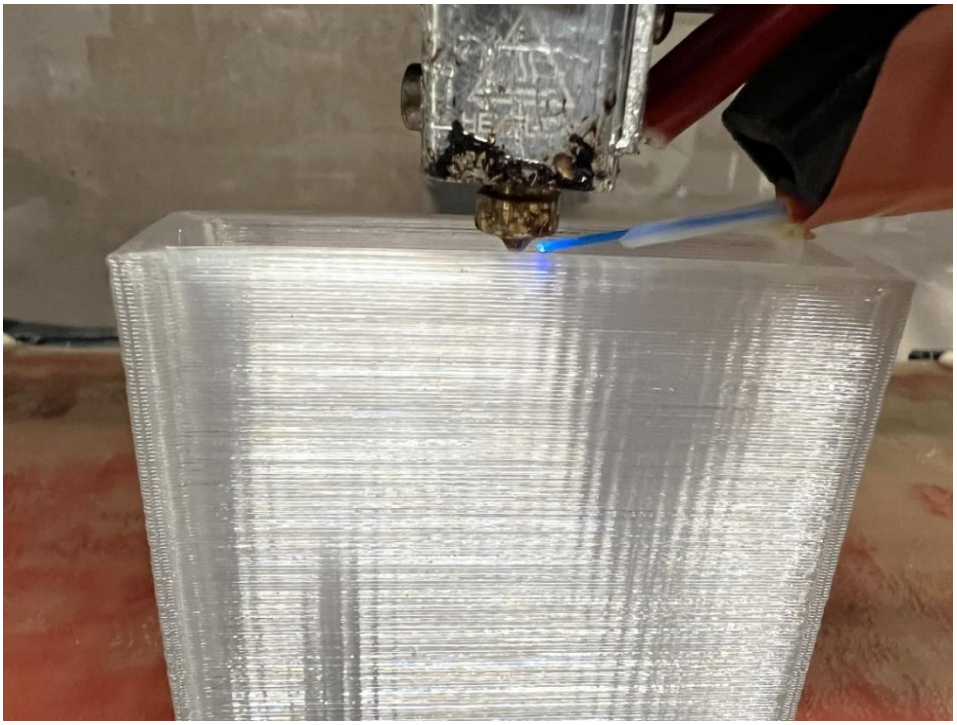

Figure 44. Photo of the in-situ UV irradiation of PC during FFF deposition process. The fiber optic is positioned approximately 0.8 cm from the sample. Irradiation occurs directly at the printer nozzle where the filament is extruded and deposited.

distance ranging from 18 to 32 mm. Employing lower magnifications facilitated the imaging of expansive areas of the fracture surface, ensuring a precise depiction of the voids across the entire surface. The fracture surfaces utilized for this analysis were obtained from the tensile experiments, as submerging PC dogbones in liquid nitrogen for approximately 15 minutes did not enhance the embrittlement of the polymer. Not all dogbone cross-sections were able to be analyzed due to tortured fracture surface from the breaking process. Nevertheless, a minimum of three dogbone cross-sections were examined for each sample. The amount of void space was determined by analyzing the resultant SEM images with ImageJ software, where a threshold tool was employed to identify and separate the black areas, representing voids, on the fracture surface. The number of pixels within these void areas was then counted. Finally, this count was divided by the total number of pixels in the image to calculate the percentage of void space, as shown in the following Equation:

$$\textbf{Void space } \% = \frac{\textbf{total number of black pixels}}{\textbf{total number of black+white pixels}} \textbf{x100}$$

Results and discussion

Mechanical properties of PC FFF printed parts

The process of FFF induces a complex shear and thermal history on the printed material that can lead to significant mechanical anisotropy in the resultant printed parts. To monitor the anisotropic behavior of the printed parts, dogbones were cut from the cube in two orthogonal orientations, as shown in **Figure 43**. Transverse and longitudinal specimens were cut from a printed cube to ensure uniform thermal histories for each sample. **Figure 45** shows representative examples of the stress-strain curves of the PC printed parts in the two orthogonal directions. As expected, the mechanical properties in the longitudinal direction are better than those in the transverse direction. Surprisingly, however, the PC parts printed exposed to UV light

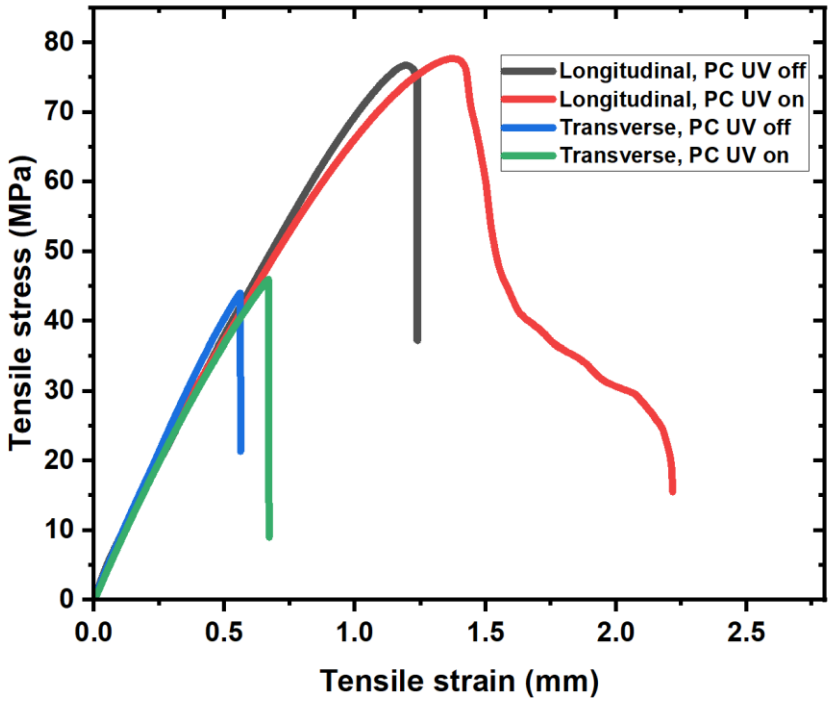

Figure 45. Stress-strain curves of PC FFF printed structures.

exhibit enhanced mechanical properties in both directions compared to those printed without UV light. **Figure 46** presents the toughness and tensile strength of the PC printed parts, reflecting their energy absorption capacity and resistance to tension-induced rupture, respectively. **Figure 46b** reveals little change in tensile strength when comparing the mechanical properties of the samples that are fabricated with UV off or UV on, irrespective of the direction. Conversely, **Figure 46a** illustrates a notable enhancement in toughness when the sample is printed with UV exposure in both directions, with 30% and 43% increase in longitudinal and transverse toughness, respectively, relative to samples printed without UV light. The observed improvements in longitudinal mechanical performance of the samples that are illuminated with UV are consistently greater than those in the UV off samples across all trials, as shown in **Table 6**. These results are surprising, as conventional assumptions might suggest that printing polycarbonate under UV light could degrade the polymer, deteriorating the mechanical strength of the printed parts. Nevertheless, the findings in **Figure 46** challenge these hypotheses. Consequently, further analysis and experimentation are needed to elucidate the underlying mechanisms driving the observed changes in mechanical behaviors.

Void Space Analysis

SEM images of the fracture surfaces of longitudinally oriented dogbones are examined to document the impact of UV light exposure during printing on the void structure. **Figure 47** shows representativ SEM images of the interfilament voids for both samples printed with and without UV light. These results offer qualitative insight into how UV illumination impacts the FFF process and the resulting properties of the printed parts. Examination of the fractured surface of the PC material shows that parts printed with UV light exhibit fewer interfilamentous voids compared to those printed without UV illumination. Quantitatively, the percentage of voids present in the samples is shown in **Figure 48**, indicating a 57% decrease in void space with UV

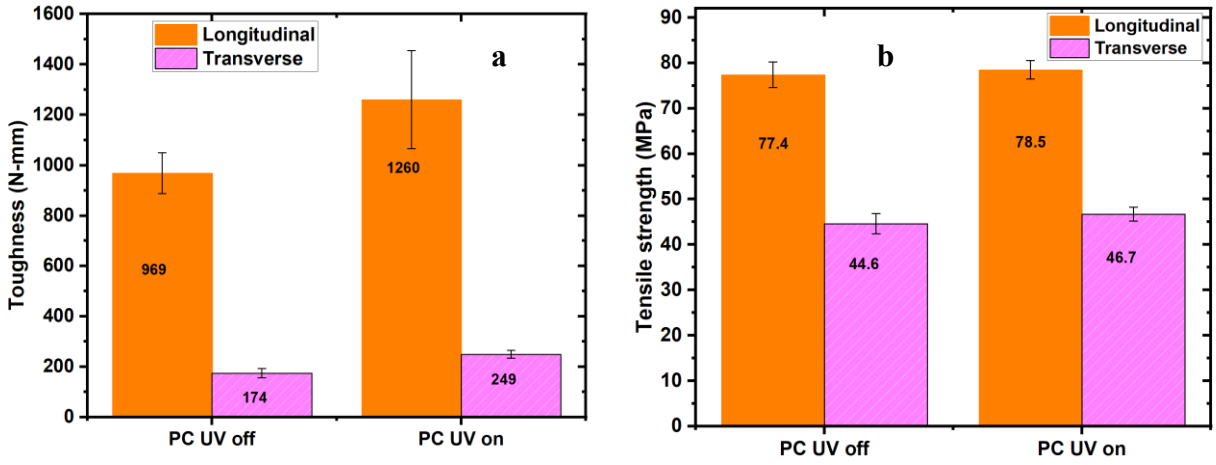

Figure 46. Toughness (a) and tensile strength (b) of the PC FFF printed structures.

Table 6. Longitudinal mechanical properties of PC printed with UV off and UV on

Experiment/ number of cubes printed	Toughness (N-mm)	
	PC UV off	PC UV on
1	1208	1393
2	974	1317
3	725	1077

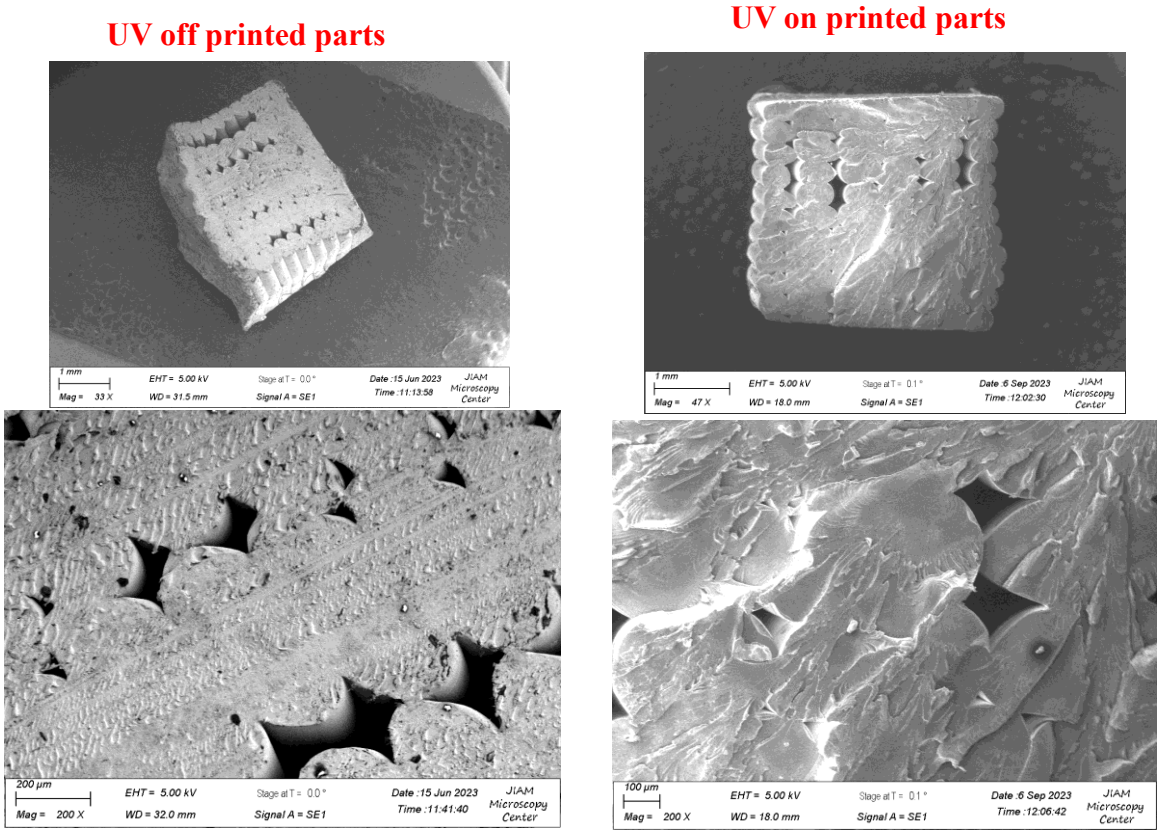

Figure 47. SEM images of longitudinal fracture surfaces of PC FFF printed parts. UV off printed parts (left), UV on printed parts (right), low magnification (top), high magnification (bottom)

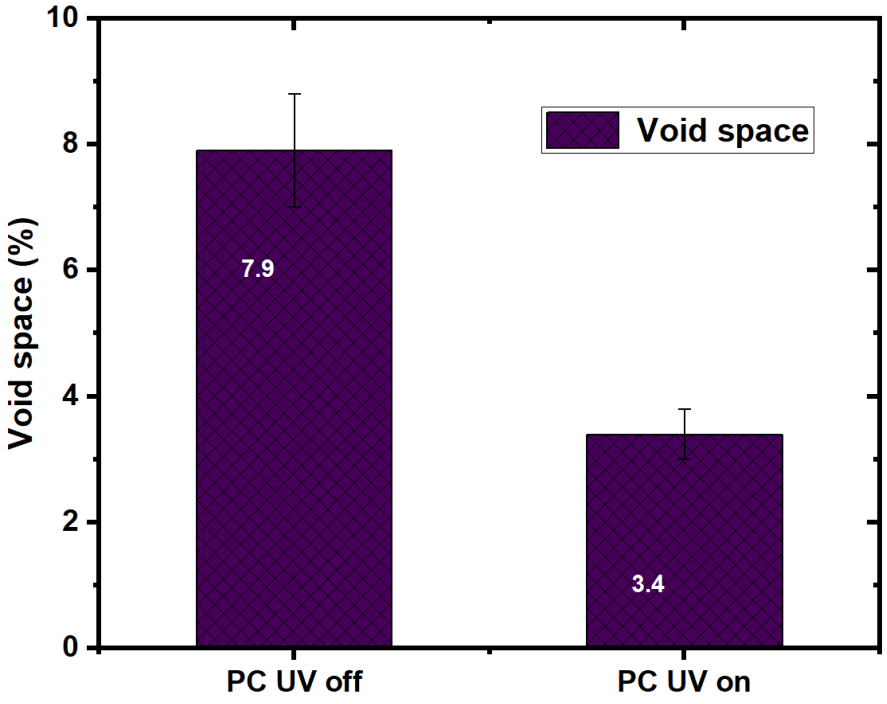

Figure 48. Percent void space of the PC FFF printed parts.

irradiation compared to parts printed without UV light. The decrease in void space in the UV on samples is consistently greater than in the UV off samples across all trials, as shown in **Table 7**.

This analysis suggests that UV illumination improves the diffusion of the polymers between filaments during the deposition process, creating a denser structure with fewer voids, thereby enhancing adhesion between filaments and enhancing the mechanical properties of the printed parts. At the molecular level, one of the major factors influencing the diffusion of polymer chains during the FFF process is the size of the polymer chains. Smaller chain sizes promote faster reptation processes during the FFF fabrication process. Therefore, one hypothesis is that UV illumination decreases the molecular size of the polymer through chain scission, facilitating molecular diffusion and interlayer adhesion during the printing. To validate this hypothesis, investigation of the molecular weight characteristics of the filament before printing and the polymer in the printed structure is necessary.

Effect of UV light on molecular weight characteristics of PC printed parts and FFF process

Polymer fragmentation leads to a decrease in molecular weight.[158,159] In order to assess the impact of UV light irradiation on the fragmentation of the polymer, the molecular weight of UV-light-printed PC parts were analyzed and compared to those of PC parts printed without UV light, that of the original PC pellet, and that of the PC filament before printing. **Figure 49** presents the molecular weight of the PC printed parts, as well as that of the PC pellets and PC filament prior to printing.

Inspection of **Figure 49** shows that the molecular weight of the polymer decreases during the filament formation process and decreases further after the filament is printed. This indicates that the extrusion process induces reactions that decrease the polymer molecular weight. Polymer pellets are melted at high temperature and extruded through a nozzle to create the filament. Throughout this process, the polymer undergoes significant thermal stress, mechanical forces,

Table 7. Void space from longitudinal fracture surfaces of PC FFF printed parts

Experiment/ number of cubes printed	Void space (%)	
	PC UV off	PC UV on
1	6.72	2.83
2	7.86	3.46
3	9.0	4.04

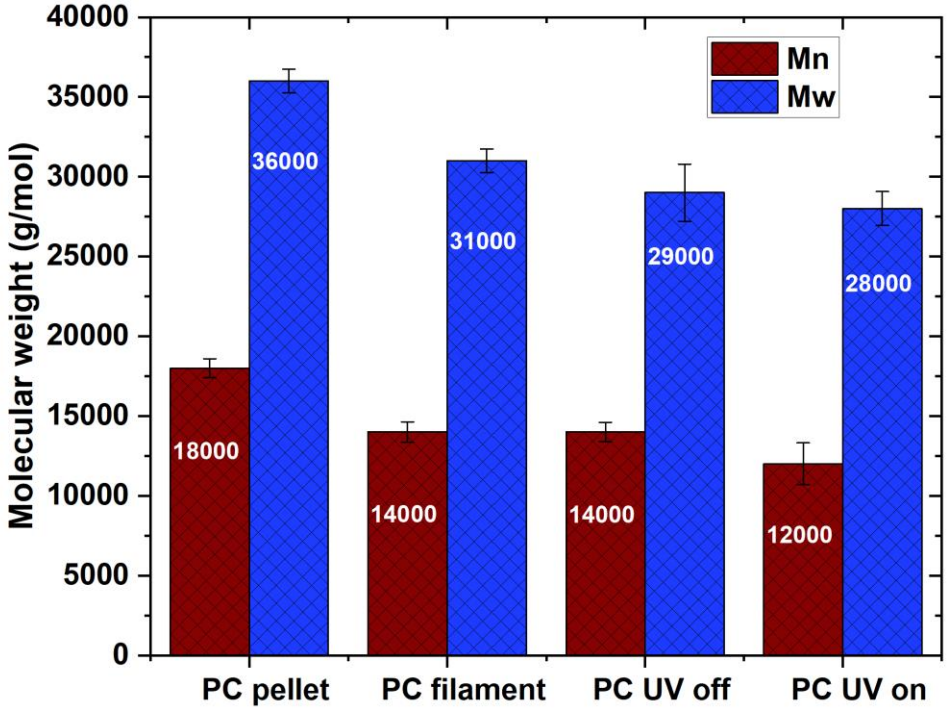

Figure 49. Weight and number average molecular weight of PC determined via gel permeation chromatography.

and shear forces, all of which can induce chain scission, breaking the polymer chains into smaller segments. Moreover, both the weight average and number average molecular weight of the printed samples decreased more with UV exposure than in the printed sample without UV exposure. Experiments were designed with multiple replicates to ensure data reliability, as shown in **Table 8**.This additional decrease in PC molecular weight upon UV exposure is consistent with previous studies that document the susceptibility of polycarbonate to chain scission with UV exposure.[159]

Although the decrease in molecular weight upon UV exposure is subtle, this change may be sufficient to affect the printing process and weaken the mechanical properties of the resulting printed parts. Previous studies have indeed shown that the degradation of polymers during the FFF process results in decreased mechanical properties of the printed parts.[160,161] However, our findings, as illustrated in Figures 45 and 46, contradict this expectation, demonstrating that samples printed with UV light exhibit improved mechanical properties compared to those printed without UV light, despite having (a slightly) lower molecular weight due to degradation. This implies that the degradation occurring during the printing and UV irradiation benefits the FFF process.

One possibility is that the decrease in molecular weight improves the interfilament adhesion, but is not sufficient to decrease mechanical properties. The improvement would appear to be related to the fact that a decrease in molecular weight leads to an increase in the diffusion coefficient and the distance that a given polymer can diffuse in a given time. Assessment of **Figure 49** and Equations 4 and 5 reveals that the change in molecular weight results in a 36% increase in the *average* diffusion coefficient and a 16% increase in the *average* diffusion distance when comparing the structure that are printed with UV off and UV on. Thus, the polymers in the UV irradiated sample diffuse faster than those printed without UV. Given that the thermal and

Table 8. Molecular weight and dispersity of PC FFF printed parts

Experiment / number of cubes printed	Mn (g/mol)		Mw (g/mol)		Mw/Mn	
	PC UV off	PC UV on	PC UV off	PC UV on	PC UV off	PC UV on
1	13,599	10,903	27,843	27,548	2.0	2.5
2	14,471	11,529	28,152	27,682	1.9	2.4
3	14,446	12,756	30,373	29,063	2.1	2.3

shear histories of the two samples are similar, the UV exposed polymer chains diffuse farther in the printing process than those not exposed to UV. This improved diffusion between layers may increase interlayer adhesion and reduce void space in the FFF printed parts.[9,58] In fact, **Figure 48** demonstrates that UV irradiation significantly reduces void space in the printed part. However, the 36% increase in *average* diffusion coefficient and 16% increase in *average* diffusion distance does not appear to be sufficient to account for the significant change in void space. For instance, it is hard to imagine how a 16% increase in average diffusion distance translates in a 57% decrease in void space. Therefore, the observed change in void space must be driven by other molecular weight characteristics apart from the alteration in the average molecular weight. With this in mind, **Figure 50** shows GPC traces, providing a qualitative comparison of the molecular weight distribution (MWD) of the PC in the printed parts, revealing a broader MWD of the PC printed with UV light compared to the PC in those printed without UV light. This figure elucidates the wider range of molecular sizes that emerge from the polymer chain scission due to UV illumination, including an enhanced low molecular weight tail (circled). As previously discussed, effective molecular diffusion is imperative to achieve adequate layer-layer adhesion and decrease void space in FFF process. For a robust interlayer interface, polymer chains must diffuse into the adjacent layer and become entangled during the printing process,[46] with the development of interfacial bond strength depending on the number of polymer chains that diffuse across the interface.[154] Thus, any factor that affects molecular diffusion in FFF process will impact interfilament adhesion and void formation, where the data presented here suggests that an increase in polymer molecular weight dispersity is important in realizing the improved diffusion.

Unfortunately, the impact of polymer molecular weight dispersity on molecular diffusion is not very well studied. In one study, Qiu et al. demonstrated that a broader molecular weight

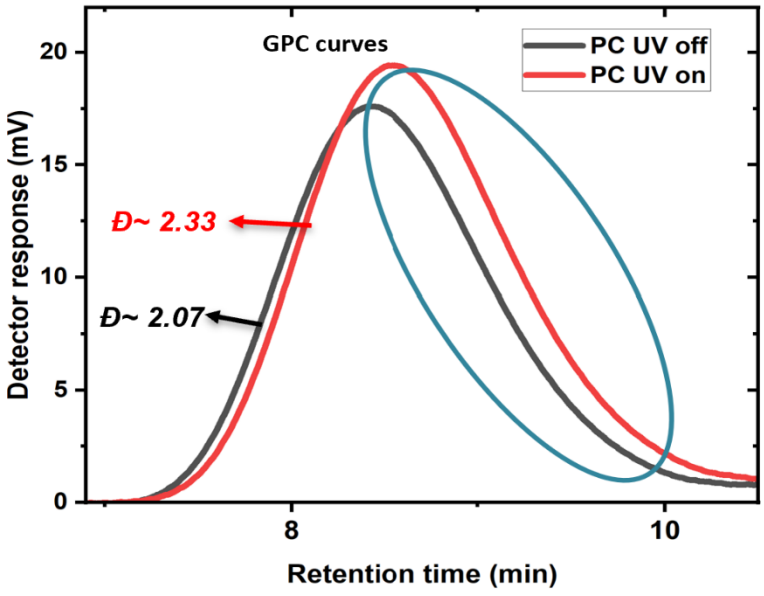

Figure 50. Gel permeation chromatography curves, GPC traces, providing a qualitative comparison of the molecular weight distributions of PC printed parts. Blue oval emphasizes low molecular weight tail.

dispersity facilitates faster polymer chain diffusion.[162] In these studies, it was observed that the diffusion coefficient of the polymer increased by a factor of 5 with an increase in the dispersity (*Đ)* of the polymer from 1.05 to 1.33. They interpret this to indicate that the polymer with a broader dispersity (*Đ*=1.33) contains more small chains than a polymer system with a similar average molecular weight and more narrow dispersity, accelerates molecular diffusion.[162]

The experimental results of Qiu et al. provides a compelling evidence that a broader molecular weight dispersity significantly increases molecular diffusion; a 27% increase in *Đ* leads to about fivefold increase in the diffusion coefficient.[162] Inspection of **Figure 49** shows that the *Đ* of the PC printed with UV on is 13% larger than the *Đ* of the PC printed with UV off. Although the exact increase in the diffusion coefficient that results from a 13% increase in *Đ* is not known, Qui et al.'s result and the pronounced reduction in interfilament voids in the PC printed with UV light relative to the PC printed without UV light suggests that it is significant. Thus, we ascribe the enhanced interfilament adhesion in PC printed with UV light to an increase in molecular weight dispersity that emerges from UV induced chain scission, resulting in increased rate of molecular diffusion.

An additional factor that may contribute to the improved interlayer adhesion and layer-to-layer diffusion is the surface segregation of the smaller polymer chains to the filament interface that would further enhance interfilament diffusion. Experimental studies have shown that surface segregation of smaller polymer chains to the interfilament interface is a crucial mechanism to reduce void space and strengthen FFF printed parts.[8,59] For example, Levenhagen et al. showed that the addition of low molecular weight surface segregating additives to commercially available acrylonitrile-butadiene-styrene (ABS) decreased the void space of ABS by more than 30%, substantially strengthening FFF ABS printed parts.[8] These studies showed that the lower molecular weight additives tend to surface segregate to the interfilament interface

more readily than higher molecular weight filament components, forming entanglements and improving adhesion between adjacent filaments.[8] This surface segregation is consistent with the entropic preference of polymer chain ends to the surface of a polymer melt.[60-62] Additionally, Chen et al. have demonstrated the significance of chain ends in promoting adhesion at a melt interface, where their studies show that interfacial adhesion increases at a polymer-polymer interface as the number of polymer chain ends at the interface increases.[62] Their interpretation of the data indicates that the increased mobility of chain ends fosters a greater rate and depth of interpenetration across the polymer interface. Increased interpenetration forms a more extensive polymer network at the interface, thereby improving adhesion. Moreover, the number of chain ends increases as polymer chain length decreases.[62]

The changes in the molecular weight characteristics of the PC that occur during printing in the presence or absence of UV is completely consistent with this interpretation. Inspection of Figures 49 and 50 shows that PC printed with UV light has a wider range of molecular sizes and more smaller chains compared to PC printed without UV light. The PC printed with UV light therefore has more chain ends than the PC printed without UV light, where these additional chain ends surface segregate during the printing process. We hypothesize that the greater number of polymer chain ends in PC printed with UV light results in more smaller chains segregated to the polymer interface which then more effectively penetrate the filament-filament interface to form entanglements between layers. This results in the PC printed with UV light to exhibit greater interfilament adhesion and fewer voids than those compared to PC printed without UV light. The data in Figures 45, 46, 47, and 48, document the pronounced improvement in the mechanical strength and significant reduction in interfilament voids for the PC printed with UV light relative to the PC printed without UV light. Thus, we holistically interpret the results presented here to indicate that the change in $Đ$ in the PC that is exposed to UV illumination results in the

formation of many smaller chains with more chain ends, improving interfilament diffusion and entanglement across the interfilament interface, thereby reducing interlayer voids and enhancing mechanical performance. The duration of UV exposure is a critical factor that could influence the extent of polymer chain scission and, consequently, the Mw, MWD, and printed part properties. Hence, the impact of varying UV light intensity and UV light exposure time on the FFF process of PC will be investigated in future work.

Thus, one of the key conclusions of this study is the demonstration of the in-situ benefits of UV light exposure during the FFF process of thermoplastics. While it is possible to create a PC with a broader molecular weight distribution by creating filaments that are a blend of molecular weights, the approach in this study offers a unique advantage by dynamically altering the dispersity of these parameters during the deposition process. This in-situ adjustment enhances part properties as they are being formed, ensuring that changes in Mw and MWD occur precisely when and where they are most beneficial. In contrast, using a molecular weight blend of PC would necessitate extensive efforts to create the filament and fine-tune the molecular weight characteristics of the blend filament. Thus, the approach presented in this study simplifies this process, offering a more versatile and effective means of enhancing mechanical performance and reducing void spaces in FFF-printed structures.

Conclusion

This study examines the impact of in-situ ultraviolet (UV) illumination during the FFF printing of polycarbonate on the molecular weight characteristics of the polymer and how changes in the molecular weight characteristics affect polymer chain diffusion and adhesion during the printing process, with the aim of reducing anisotropy and strengthening the mechanical integrity of the printed parts. Analysis of the mechanical characteristics and fracture surfaces of the printed components demonstrates that PC printed with UV light exhibits superior

mechanical strength, especially the toughness, in both transverse and longitudinal orientations, as well as reduced void space compared to PC printed without UV light. The enhancement in overall part strength and reduction in voids in PC printed with UV light is attributed to improved interlayer adhesion and entanglement across the interfilament interface. UV irradiation initiates fragmentation of the polymer, significantly altering the molecular weight distribution and creating many smaller chains with more chain ends. Formation of these many smaller chains with more chain ends enhances interfilament diffusion and adhesion, thereby mitigating interlayer voids and improving mechanical performance. Consequently, this study provides fundamental insights into the influence of UV light on the molecular dispersity of the polymer and the impact of these changes on the FFF process, emphasizing the importance of the enhanced low molecular weight tail in the molecular weight distribution on the molecular diffusion during the printing process. This insight offers a straightforward method for fabricating more robust and isotropic structures through 3D printing of UV susceptible thermoplastics. Furthermore, the cost-effectiveness of this approach makes it an economically viable alternative to material design methods involving intricate synthesis procedure.

Chapter 6: Conclusions and Future Work

3D printing technology enables the fast and cost-efficient fabrication of intricate objects with design flexibility. However, parts produced via 3D printing often exhibit weak mechanical and anisotropic properties compared to those created through traditional processing techniques, such as injection molding. The poor mechanical properties of 3D-printed parts stem from weak interfacial adhesion between layers resulting from limited chain mobility, large voids in the printed structures due to inadequate coalescence, insufficient molecular chain entanglement at the interfaces between adjacent layers, and residual stress due to crystallization. Another major shortcoming in fabricating 3D-printed structures is the limited availability of materials designed for specific environments encountered during printing. Therefore, the research presented in this dissertation focuses on applying the fundamental principles of polymer science to rationally design polymeric feedstocks to improve powder bed fusion (PBF) and fused filament fabrication (FFF) 3D printing processes and the properties of the resultant printed parts.

Tailoring Coalescence Dynamics of Polypropylene Feedstocks for Powder Bed Fusion Via Molecular Design

In this study, the coalescence dynamics of high molecular weight (HMW) polypropylene (PP) powders (250 kDa and 340 kDa) were modified to improve their particle consolidation during the PBF process. Low molecular weight (LMW) PP (12 kDa) were incorporated into 250 kDa and 340 kDa PP via thermally induced phase separation (TIPS) to form blended powders. Neat 250 kDa and 340 kDa PP powders were also prepared to serve as references for comparison with the blended powders. The rheological behavior of the prepared powders, evaluated using rotational rheometry, revealed a significant reduction in the zero-shear viscosity of the HMW PP powders with the inclusion of 12 kDa PP additive. In-situ hot-stage microscopy was employed to monitor the coalescence behavior of these powders. The results demonstrated a pronounced

increase in the coalescence rate and enhanced neck growth in the blended PP feedstocks compared to their neat polymer counterparts. The in-situ hot-stage microscopy technique combines microscopy with a temperature-controlled chamber, allowing for real-time monitoring of the PP particle consolidation under thermal condition. A temperature of 164°C was chosen for the coalescence experiments, as it is approximately at the peak melting temperature of PP. The observed enhancement in coalescence dynamics in the blended powders significantly improves their part robustness in the PBF process, as shown in Chapter 3 of this dissertation. The data were fit to the Hopper coalescence model to gain insight into the molecular-level mechanisms governing particle consolidation during coalescence and the fundamental driving forces influencing the molecular weight (MW) dependence of the coalescence process. The result shows that the improvement of the coalescence dynamics is governed by lowering the extensional viscosity of the polymer melt. Moreover, the addition of LMW does not significantly alter the surface tension of MW blend powders Additionally, the findings indicate that LMW does not surface segregate in the blend but is homogeneously distributed in the blend, and extensional flow dominates the coalescence process.

Future Work

The material formulations presented in this dissertation improve the coalescence dynamics of HMW polymer powdeers with addition of the LMW polymer. However, the effect of particle-substrate adhesion on the coalescence rate should also be explored. The coalescence experiment presented in this dissertation tracks the consolidation among PP particles and examines the impact of viscosity on particle coalescence. Microscopic glass slides are used as standard substrates for performing the in-situ hot-stage microscopy coalescence experiment. While the Hopper and Frenkel coalescence models used in this study show that viscosity and surface tension of the polymer are critical factors influencing the coalescence process, these models were

developed without considering adhesion forces between particles and the substrate. Nevertheless, these forces could significantly affect coalescence dynamics. The influence of particle adhesion on the substrate could potentially reduce the coalescence rate. Therefore, future investigations will explore how the substrate affects particle coalescence, as stronger interactions between the polymer and substrate may potentially delay particle-particle coalescence. A potential method for this experiment is using treated glass surfaces to tune the wettability of the powder particle with the glass surface. Comparing the coalescence rates of powders on silicone-coated glass surfaces versus untreated glass surfaces will help elucidate whether the interaction between the PP particles and the glass surface impacts coalescence dynamics.

Impact of Polymer Molecular Weight Blends on Polypropylene Printed Parts

50/50 mixtures of 12 kDa /250 kDa, 12 kDa /340 kDa, 250 kDa /340 kDa, and 33/33/33 mixture of 12 kDa /250 kDa /340 kDa PP powders were prepared via TIPS and printed via PBF by Chris Williams Group at Virginia Tech. Neat 250 kDa and 340 kDa powders were also prepared for comparison with the blended powder feedstocks. The mechanical properties of the parts printed from the blended powders were compared to mechanical properties of the samples printed from the neat 250 kDa or 340 kDa PP powders. All powders were printed at constant processing parameters (beam velocity: 3750 mm/s; hatch spacing: 0.3 mm; bed temperature: 140 °C; laser power:50 W) to allow a direct assessment of how MW affects the quality and mechanical strength of the printed parts. Careful examination of the printed components from these formulated powder feedstocks reveals that the samples printed from the feedstocks with blended MW have a pronounced reduction in void space and a slight increase in percent crystallinity compared to samples printed from powders printed from their unimodal MW counterparts. Additionally, dynamic mechanical analysis reveals a notable enhancement in storage modulus for samples printed from blended MW compared to samples printed from

unimodal MW. Surprisingly, powders formed from the neat 12 KDa PP were not printable via PBF at the set processing parameters, suggesting that a minimum zero-shear viscosity to surface tension ratio is required to accomplish an appropriate coalescence of a scanned layer during the PBF process. Enhancement in the mechanical performance of the blend with LMW additives indicates that adding LMW to larger polymers does not have a detrimental plasticizing effect on the mechanical properties. The increased moduli observed in blends are attributed to enhanced coalescence, driven by the decreased viscosity of the powder during the PBF process. Improved particle coalescence decreases void space, thereby strengthening the printed structures.

Future Work

Post-processing heat treatment, such as thermal annealing, can play a vital role in further enhancing the mechanical properties of the PP-printed parts. The thermal annealing process involves heating the printed parts to a specific temperature, holding them at that temperature for a set period, and cooling the samples to room temperature. Annealing above the polymer's glass transition temperature can facilitate interlayer diffusion of the polymer molecules, leading to increased interlayer adhesion and entanglements and, therefore, improves mechanical integrity. Additionally, this process can rearrange polymer segments into more crystalline structures and release residual stress by relaxing polymer chains, thus improving their mechanical strength. However, care must be taken to retain the initial dimensions of the structure, as this heating proess may result in loss of fidelity of the printed structure. Therefore, future work will leverage this post-processing heat treatment to examine how it may further enhance the mechanical properties of the PP-printed parts. The PP-printed samples will be annealed at different temperatures between Tg and T_m of PP for a specific period. The annealing temperature that provides the highest mechanical strength for the printed samples will be chosen for further study, examining additional annealing time to understand the correlation between annealing time and

the mechanical performance of the printed structures. By comparing the percentage crystallinity values as determined with DSC and the irreversible thermal strain of unannealed and annealed samples and correlating them to their mechanical behavior, the impact of this post-processing heat treatment on the properties and structure of the printed parts will be ascertained. Future work will also encompass more variation in the amounts of the LMW additive (12 kDa PP) in the powder formulation.

Impact of Polycarbonate on Polypropylene Feedstocks Tailored for Powder Bed Fusion

This study investigates the influence of incorporating polycarbonate (PC) into PP powder at varying concentrations. The TIPS method was used to create powders that are a blend of PC with a MW of 36 kDa and PP at loadings ranging from 10 to 50 wt.% to create feedstocks that are suitable for printing via PBF. Pure PC and PP powder feedstocks were also created from these MW to serve as baseline references for this investigation. The resultant formulated powder feedstocks were extensively characterized, employing various tools to determine the impact of the added PC on the resultant powders' intrinsic and extrinsic properties. Examination of the shape and size of the blend powder via scanning electron microscopy (SEM) and ImageJ software shows that the addition of PC does not remarkably alter the shape and size of the blend powder particles. This suggests that the PP drives the formation of these powders in the TIPS process. Energy dispersive X-ray spectroscopy (EDS) performed on the powders provides the composition of each powder particle after the TIPS process. These studies indicate that each powder particle is a blend of PP and PC. The EDS results also show that the PC content varies among individual particles. Further analysis of the Tg shows that the Fox model deviates significantly from the blend's experimentally determined glass transition temperature. This is interpreted to verify that PP and PC do not form a fully miscible blend in the powder formed by the TIPS process. DSC and small-angle X-ray scattering were used to analyze the crystallization

and crystal structures of the PC/PP blend powder, respectively. These results show faster crystallization and a significant decrease in lamella thickness of PP with the addition of PC. Furthermore, as determined by DSC, the % crystallinity of PP in the blend decreases with the addition of PC. The decrease in lamella thickness could be attributed to the presence of PC chains reducing the opportunity for crystalline regions to form during the crystallization process of the powder feedstocks.

Future Work

The future work will focus on droplet coalescence and the printability of the resultant PP-PC powder feedstocks. Droplet coalescence will be examined by in-situ hot-stage microscopy, whle the powders will be printed by our collaborators. Additionally, the mechanical performance of the printed structures will be examined to correlate how PC incorporation impacts the mechanical strength of PP printed components. The Tg analysis of the initial powders indicates that the PP and PC do not form a fully miscible blend in the TIPS process, and the impact of this initial morphology will be of particular interest in these studies. Thus, future work will also incorporate chemical compatibilizer into the PP-PC system to examine its impact on the PP-PC feedstock morphology.

Impact of UV Light Exposure on the FFF of Polycarbonate

PC is an engineering thermoplastic known for its high impact strength, transparency, excellent dimensional stability, and resistance to creep. Due to these desirable properties, PC is widely used in numerous industrial sectors. However, when PC filament is processed using FFF, the resulting printed parts suffer from poor interlayer bonding. This leads to large voids inside the printed parts, resulting in poor mechanical performance and anisotropic behavior. These issues stem from the poor interlayer diffusion and the intricate thermal histories experienced during fabrication. In this dissertation, these challenges were addressed by subjecting the PC

filament to UV light during printing. The exposure of PC filament to UV light causes photodegradation of PC, leading to a notable alteration in MW distribution and the formation of numerous smaller chains with increased chain ends. Creating these numerous smaller chains with increased chain ends facilitates interlayer diffusion and interlayer bonding, effectively minimizing interlayer voids, enhancing mechanical strength, and reducing anisotropy.

Future Work

In Chapters 2 and 3 of this dissertation, the design of MW blend feedstocks effectively enhances the droplet coalescence of semi-crystalline polymers during printing and strengthens the resultant printed parts. This same protocol will be applied to design PC materials for FFF. By incorporating LMW (MW < 36 kDa but above the entanglement MW of PC) PC into HMW (MW = 36 kDa) PC, bimodal MW PC feedstocks will be created for FFF. The LMW additives will be incorporated via TIPS using an appropriate solvent in the TIPS process to form bimodal MW PC powder materials. These powders will be dried to a constant mass and then extruded into the FFF filament using an extruder. Direct co-extrusion of HMW and LMW components using an extruder can present several challenges, including viscosity mismatch and the incomplete incorporation of the additives into the final filament formulation. In co-extruding HMW and LMW directly from the extruder, the HMW component is more viscous than the LMW component, which can hinder uniform flow and proper mixing of the two components during extrusion. This can lead to issues with filament uniformity and overall product consistency. In addition, some PC pellets may remain in the extruder, affecting the amount of the additives that go into the final FFF filament. Thus, using TIPS in this experiment will allow for better mixing at a molecular level, leading to a more homogeneous blend of HMW and LMW PC components and a more accurate incorporation of the additives in the final FFF filament formulation. Additional future work on the impact of UV light exposure on the FFF will be

investigation of the impact of varying UV light intensity and UV light exposure time on the FFF process of PC.

References

(1) Idrees, M.; Jeelani, S.; Rangari, V., Three-Dimensional-Printed Sustainable Biochar Recycled PET Composites. ACS Sustainable Chemistry & Engineering **2018,** 6 (11), 13940-13948.

(2) Pereira T.; Kennedy J. V,; Potgieter. J. A comparison of traditional manufacturing vs additive manufacturing, the best method for the job. Procedia Manufacturing.**2019**, 30, 11–18.

(3) Mwema, F. M.; Akinlabi, E. T., Basics of Fused Deposition Modelling (FDM). In Fused Deposition Modeling: Strategies for Quality Enhancement, Springer International Publishing: Cham, **2020**, 1-15

(4) Riggins. A. Material Formulation and Process Optimization Towards Fabricating Robust 3D Printed Structures. PhD diss., University of Tennessee, **2023**.

(5) Shahrubudin, N.; Lee, T. C.; Ramlan, R., An Overview on 3D Printing Technology: Technological, Materials, and Applications. Procedia Manufacturing **2019,** 35, 1286-1296

(6) Bhatia, A.; Sehgal, A. K. Additive Manufacturing Materials, Methods and Applications: A Review. Materials Today: Proceedings **2023**, 81, 1060–1067.

(7) Sargent. F. J.; Schwartz R. X. 3D Printing: Overview, Impacts, and the Federal Role. everycrsreport.com. **2019**

(8) Levenhagen, N. P.; Dadmun, M. D. Improving Interlayer Adhesion in 3D Printing with Surface Segregating Additives: Improving the Isotropy of Acrylonitrile-Butadiene-Styrene Parts. ACS Appl. Polym. Mater. **2019**, 1 (4), 876–884. https://doi.org/10.1021/ACSAPM.9B00051.

(9) Rostom, S.; Dadmun, M. D., Improving heat transfer in fused deposition modeling with graphene enhances inter filament bonding. Polymer Chemistry **2019,** 10 (44), 5967-5978.

(10) Perryman, S. C.; Dadmun, M. D. Incorporating Crosslinks in Fused Filament Fabrication: Molecular Insight into Post Deposition Reactions. Addit. Manuf. **2021**, 38. https://doi.org/10.1016/j.addma.2020.101746.

(11) Praveena, B. A.; Lokesh, N.; Buradi, A.; Santhosh, N.; Praveena, B. L.; Vignesh, R. A Comprehensive Review of Emerging Additive Manufacturing (3D Printing Technology): Methods, Materials, Applications, Challenges, Trends and Future Potential. Mater. Today Proc. **2022**, 52, 1309–1313. https://doi.org/10.1016/j.matpr.2021.11.059.

(12) Iftekar, S. F.; Aabid, A.; Amir, A.; Baig, M. Advancements and Limitations in 3D Printing Materials and Technologies: A Critical Review. Polym. 2023, Vol. 15, Page 2519 **2023**, 15 (11), 2519. https://doi.org/10.3390/POLYM15112519.

(13) Guan, K.; George, A.; Dadmun, M. D.; Bryant, J. S.; Bortner, M. J.; Williams, C. B. Expanding Polymeric Feedstocks for Powder Bed Fusion via Rational Control of Liquid–Liquid Phase Separation. J. Polym. Sci. **2023**. https://doi.org/10.1002/POL.20230286

(14) Bourell, D.; Kruth, J. P.; Leu, M.; Levy, G.; Rosen, D.; Beese, A. M.; Clare, A., Materials for additive manufacturing. CIRP Annals **2017,** 66 (2), 659-681

(15) Guan, Kaizhong, "Designing Polymer Materials for Improved Additive Manufacturing. " Master's Thesis, University of Tennessee, **2021.**

(16) Levy, G. N.; Schindel, R.; Kruth, J. P. Rapid Manufacturing and Rapid Tooling with Layer Manufacturing (LM) Technologies, State of the Art and Future Perspectives. CIRP Ann. - Manuf. Technol. **2003**, 52 (2), 589–609. https://doi.org/10.1016/S0007-8506(07)60206-6

(17) Williams, J. M.; Adewunmi, A.; Schek, R. M.; Flanagan, C. L.; Krebsbach, P. H.; Feinberg, S. E.; Hollister, S. J.; Das, S. Bone Tissue Engineering Using Polycaprolactone Scaffolds Fabricated via Selective Laser Sintering. Biomaterials **2005**, 26 (23), 4817–

4827. https://doi.org/10.1016/j.biomaterials.2004.11.057.

(18) Singh, R.; Gupta, A.; Tripathi, O.; Srivastava, S.; Singh, B.; Awasthi, A.; Rajput, S. K.; Sonia, P.; Singhal, P.; Saxena, K. K. Powder Bed Fusion Process in Additive Manufacturing: An Overview. Mater. Today Proc. **2019**, 26, 3058–3070. https://doi.org/10.1016/j.matpr.2020.02.635.

(19) Gibson, I.; Shi, D. Material Properties and Fabrication Parameters in Selective Laser Sintering Process. Rapid Prototyp. J. **1997**, 3 (4), 129–136. https://doi.org/10.1108/13552549710191836/FULL/PDF.

(20) Yan, C.; Shi, Y.; Hao, L. Investigation into the Differences in the Selective Laser Sintering between Amorphous and Semicrystalline Polymers. Int. Polym. Process. **2011**, 26 (4), 416–423. https://doi.org/10.3139/217.2452/MACHINEREADABLECITATION/RIS.

(21) Lupone, F.; Padovano, E.; Casamento, F.; Materials, C. B. Process Phenomena and Material Properties in Selective Laser Sintering of Polymers: A Review. mdpi.com **2021**. https://doi.org/10.3390/ma15010183.

(22) Chatham, C. A.; Long, T. E.; Williams, C. B. A Review of the Process Physics and Material Screening Methods for Polymer Powder Bed Fusion Additive Manufacturing. Prog. Polym. Sci. **2019**, 93, 68–95. https://doi.org/10.1016/J.PROGPOLYMSCI.2019.03.003.

(23) Das, A.; Bryant, J. S.; Williams, C. B.; Bortner, M. J. Melt-Based Additive Manufacturing of Polyolefins Using Material Extrusion and Powder Bed Fusion. **2023**.63 https://doi.org/10.1080/15583724.2023.2220024.

(24) Nelson, J. C. Selective Laser Sintering: A Definition of the Process and an Empirical Sintering Model. PhD diss, University of Texas Austin, **1993**

(25) Sola, A.; Nouri, A. Microstructural Porosity in Additive Manufacturing: The Formation and Detection of Pores in Metal Parts Fabricated by Powder Bed Fusion. **2019**. https://doi.org/10.1002/amp2.10021.

(26) Wang, Y.; Shen, J.; Yan, M.; Tian, X. Poly Ether Ether Ketone and Its Composite Powder Prepared by Thermally Induced Phase Separation for High Temperature Selective Laser Sintering. Mater. Des. 2021, 201. https://doi.org/10.1016/j.matdes.**2021**.109510.

(27) Wang, S.-J.; Liu, J.-Y.; Chu, L.-Q.; Zou, H.; Zhang, S.-J.; Wu, C.-J., Preparation of polypropylene microspheres for selective laser sintering via thermal-induced phase separation: Roles of liquid–liquid phase separation and crystallization. Journal of Polymer Science Part B:Polymer Physics **2017**, 55 (4), 320-329

(28) Kloos, S.; Dechet, M. A.; Peukert, W.; Schmidt, J., Production of spherical semicrystalline polycarbonate microparticles for Additive Manufacturing by liquid-liquid phase separation. Powder Technology **2018**, 335, 275-284

(29) Dechet, M. A.; Goblirsch, A.; Romeis, S.; Zhao, M.; Lanyi, F. J.; Kaschta, J.; Schubert, D. W.; Drummer, D.; Peukert, W.; Schmidt, J., Production of polyamide 11 microparticles for Additive Manufacturing by liquid-liquid phase separation and precipitation. Chemical Engineering Science **2019,** 197, 11-25

(30) Riggins, A. W.; Dadmun, M. D. Controlling Residual Stress in Material Extrusion 3D Printing through Material Formulation. Addit. Manuf. **2023**, 73, 103678. https://doi.org/10.1016/j.addma.2023.103678.

(31) Levenhagen, N. P.; Dadmun, M. D. Reactive Processing in Extrusion-Based 3D Printing to Improve Isotropy and Mechanical Properties. Macromolecules **2019,** 52 (17), 6495-6501

(32) Benedetti, L.; Brulé, B.; Decraemer, N.; Evans, K. E.; Ghita, O. Evaluation of Particle

Coalescence and Its Implications in Laser Sintering. Powder Technol. **2019**, 342, 917–928. https://doi.org/10.1016/J.POWTEC.2018.10.053.

(33) Chatham, C A.; Bortner, M. J.; Johnson, B. N.; Long, T. E.; Williams, C. B. Predicting Mechanical Property Plateau in Laser Polymer Powder Bed Fusion Additive Manufacturing via the Critical Coalescence Ratio. Mater. Des. **2021**, 201. https://doi.org/10.1016/J.MATDES.2021.109474.

(34) Benié, K.; Barrière, T.; Placet, V.; Cherouat, A. Introducing a New Optimization Parameter Based on Diffusion, Coalescence and Crystallization to Maximize the Tensile Properties of Additive Manufacturing Parts. Addit. Manuf. **2023**, 69. https://doi.org/10.1016/j.addma.2023.103538.

(35) Garzon-Hernandez, S.; Garcia-Gonzalez, D.; Jérusalem, A.; Arias, A. Design of FDM 3D Printed Polymers: An Experimental-Modelling Methodology for the Prediction of Mechanical Properties. Mater. Des. **2020**, 188. https://doi.org/10.1016/j.matdes.2019.108414

(36) Chatham, C. A.; Washington, A. L. A Framework for Forming Thermoset Polymer Networks during Laser Powder Bed Fusion Additive Manufacturing. Addit. Manuf. **2023**, 72. https://doi.org/10.1016/j.addma.2023.103620.

(37) Dechet, M. A.; Gómez Bonilla, J. S.; Grünewald, M.; Popp, K.; Rudloff, J.; Lang, M.; Schmidt, J. A Novel, Precipitated Polybutylene Terephthalate Feedstock Material for Powder Bed Fusion of Polymers (PBF): Material Development and Initial PBF Processability. Mater. Des. **2021**, 197. https://doi.org/10.1016/j.matdes.2020.109265.

(38) Jagota, A.; Argento, C.; Mazur, S. Growth of Adhesive Contacts for Maxwell Viscoelastic Spheres. J. applied Physics aip.scitation.org **1998**, 83 (1), 3840. https://doi.org/10.1063/1.366679.

(39) Lin, Y. Y.; Hui, C. Y.; Jagota, A. The Role of Viscoelastic Adhesive Contact in the Sintering of Polymeric Particles. J. Colloid Interface Sci. **2001**, 237 (2), 267–282. https://doi.org/10.1006/JCIS.2001.7470.

(40) Verbelen, L.; Dadbakhsh, S.; Van Den Eynde, M.; Kruth, J. P.; Goderis, B.; Van Puyvelde, P. Characterization of Polyamide Powders for Determination of Laser Sintering Processability. Eur. Polym. J. **2016**, 75, 163–174. https://doi.org/10.1016/J.EURPOLYMJ.2015.12.014

(41) Moreira, J. C.; Demarquette, N. R. Influence of Temperature, Molecular Weight, and Molecular Weight Dispersity on the Surface Tension of PS, PP, and PE. I. Experimental. J. Appl. Polym. Sci. **2001**, 82 (8), 1907–1920. https://doi.org/10.1002/APP.2036.

(42) Jalbert, C.; Koberstein, J. T.; Yilgor, I.; Gallagher, P.; Krukonis, V. Molecular Weight Dependence and End-Group Effects on the Surface Tension of Poly(Dimethylsiloxane). Macromolecules. **1993**, 26 (12), 3069–3074. https://doi.org/10.1021/MA00064A012

(43) Vlachopoulos, J.; Strutt. D. The Role of Rheology in Polymer Extrusion. New technologies for extrusion. polydynamics.com. **2003**

(44) Scribben, E.; Baird, D.; Wapperom, P. The Role of Transient Rheology in Polymeric Sintering. Rheol. Acta **2006**, 45 (6), 825–839. https://doi.org/10.1007/S00397-005-0039-1/FIGURES/13.

(45) Verdier, C.; Brizard, M. Understanding Droplet Coalescence and Its Use to Estimate Interfacial Tension. Springer **2002**, 41 (6), 514–523. https://doi.org/10.1007/s00397-002-0249-8

(46) Levenhagen, N. Improving the Isotropy of Additively Manufactured Parts by Fused Deposition Modeling: From Polymeric Self-Assembly to Reactive Processing. PhD diss., University of Tennessee, Knoxville, **2019**

(47) Lodge, T. P. Reconciliation of the Molecular Weight Dependence of Diffusion and Viscosity in Entangled Polymers. Phys. Rev. Lett. **1999**, 83 (16), 3218–3221. https://doi.org/10.1103/PhysRevLett.83.3218

(48) Das, A.; Marnot, A. E. C.; Fallon, J. J.; Martin, S. M.; Joseph, E. G.; Bortner, M. J. Material Extrusion-Based Additive Manufacturing with Blends of Polypropylene and Hydrocarbon Resins. ACS Appl. Polym. Mater. **2020**, 2 (2), 911–921. https://doi.org/10.1021/ACSAPM.9B01127

(49) Yang, D.; Cao, Y.; Zhang, Z.; Yin, Y.; Li, D. Effects of Crystallinity Control on Mechanical Properties of 3D-Printed Short-Carbon-Fiber-Reinforced Polyether Ether Ketone Composites. Polym. Test. **2021**, 97, 107149. https://doi.org/10.1016/J.POLYMERTESTING.2021.107149.

(50) Dupin, S.; Lame, O.; Barrès, C.; Charmeau, J. Y. Microstructural Origin of Physical and Mechanical Properties of Polyamide 12 Processed by Laser Sintering. Eur. Polym. J. **2012**, 48 (9), 1611–1621. https://doi.org/10.1016/J.EURPOLYMJ.2012.06.007.

(51) Andjelic, S.; Scogna, R. C. Polymer Crystallization Rate Challenges: The Art of Chemistry and Processing. J. Appl. Polym. Sci. **2015**, 132 (38). https://doi.org/10.1002/APP.42066

(52) Berlic, C.; Barna, V. SPORADIC POLYMER CRYSTALLIZATION IN THE n-DIMENSIONAL SPACE. Digest Journal of Nanomaterials and Biostructures. **2016**, 11, 159-165.

(53) Li, C.; Tian, G.; Zhang, Y.; Zhang, Y. Crystallization Behavior of Polypropylene/Polycarbonate Blends. Polym. Test. **2002**, 21 (8), 919–926. https://doi.org/10.1016/S0142-9418(02)00034-X.

(54) Papageorgiou, G. Z.; Achilias, D. S.; Bikiaris, D. N. Crystallization Kinetics of

Biodegradable Poly(Butylene Succinate) under Isothermal and Non-Isothermal Conditions. Macromol. Chem. Phys. **2007**, 208 (12), 1250–1264. https://doi.org/10.1002/MACP.200700084.

(55) Sperling, L. H. Introduction to Physical Polymer Science: Fourth Edition. Introd. to Phys. Polym. Sci. Fourth Ed. **2005**, 1–845. https://doi.org/10.1002/0471757128

(56) Guo, Q. Polymer Morphology: Principles, Characterization, and Processing. Polym. Morphol. Princ. Charact. Process. **2016**, 1–445. https://doi.org/10.1002/9781118892756.

(57) Iannace, S.; Nicolais, L. Isothermal Crystallization and Chain Mobility of Poly (L-Lactide). J Appl Polym Sci **1997**, 64, 911–919. https://doi.org/10.1002/(SICI)1097-4628(19970502)64:5.

(58) Levenhagen, N. P.; Dadmun, M. D. Bimodal Molecular Weight Samples Improve the Isotropy of 3D Printed Polymeric Samples. Polymer (Guildf). **2017**, 122, 232–241. https://doi.org/10.1016/J.POLYMER.2017.06.057.

(59) Levenhagen, N. P.; Dadmun, M. D. Interlayer Diffusion of Surface Segregating Additives to Improve the Isotropy of Fused Deposition Modeling Products. Polymer (Guildf). **2018**, 152, 35–41. https://doi.org/10.1016/J.POLYMER.2018.01.031.

(60) Mahmoudi, P.; Matsen, M. W. Entropic Segregation of Short Polymers to the Surface of a Polydisperse Melt. Eur. Phys. J. E **2017**, 40 (10). https://doi.org/10.1140/EPJE/I2017-11575-7.

(61) Blaber, S.; Mahmoudi, P.; Spencer, R. K. W.; Matsen, M. W. Effect of Chain Stiffness on the Entropic Segregation of Chain Ends to the Surface of a Polymer Melt. J. Chem. Phys. **2019**, 150 (1), 14904. https://doi.org/10.1063/1.5064549/152305.

(62) Chen, N.; Maeda, N.; Tirrell, M.; Israelachvili, J. Adhesion and Friction of Polymer Surfaces: The Effect of Chain Ends. Macromolecules **2005**, 38 (8), 3491–3503.

https://doi.org/10.1021/MA047733E.

(63) Perryman, Stevenson C. Interfaces and Dynamics in Polymeric 3D Printing and Crystalline Polymer Blends. PhD diss., University of Tennessee, **2021**.

(64) Kalogeras, I. M. Glass-Transition Phenomena in Polymer Blends. Encycl. Polym. Blends **2016**, 1–134. https://doi.org/10.1002/9783527653966.CH1

(65) Marin, N.; Favis, B. D. Co-Continuous Morphology Development in Partially Miscible PMMA/PC Blends. Polymer (Guildf). **2002**, 43 (17), 4723–4731. https://doi.org/10.1016/S0032-3861(02)00280-X.

(66) Hak Kim, J.; Ryul Min, B.; Soo Kang, Y. Thermodynamic Model of the Glass Transition Behavior for Miscible Polymer Blends. Macromolecules. **2006**. https://doi.org/10.1021/ma052436a.

(67) Aid, S.; Eddhahak, A.; Ortega, Z.; Froelich, D.; Tcharkhtchi, A. Predictive Coalescence Modeling of Particles from Different Polymers: Application to PVDF and PMMA Pair. J. Mater. Sci. **2017**, 52 (19), 11725–11736. https://doi.org/10.1007/S10853-017-1302-4.

(68) Bellehumeur, C. T.; Bisaria,', M. K.; Vlachopoulos', J. An Experimental Study and Model Assessment of Polymer Si Nte r i Ng. polym.Eng.sc. **1996**, 26 (17) 2198-2207

(69) R.W Hopper. Coalescence of Two Equal Cylinders: Exact Results for Creeping Viscous Plane Flow Driven by Capillarity. Wiley Online Libr. **1984**, 67 (12), C-262-C-264. https://doi.org/10.1111/j.1151-2916.1984.tb19692.x

(70) Xu, X.; Yi, W.; German, R. M. Densification and Strength Evolution in Solid-State Sintering. Part I Experimental Investigation. J. Mater. Sci. **2002**, 37 (3), 567–575. https://doi.org/10.1023/A:1013773725410.

(71) Xu, X.; Lu, P.; German, R. M. Densification and Strength Evolution in Solid-State Sintering. Part II. Strength Model. J. Mater. Sci. **2002**, 37 (1), 117–126.

https://doi.org/10.1023/A:1013110328307.

(72) German RM. Sintering: From Empirical Observations to Scientific Principles. Oxford, UK. **2014**. Elsevier

(73) Kang, S.-J. L. Sintering: Densification, Grain Growth and Microstructure. Oxford. **2005.** Elsevier

(74) Zhao, M.; Drummer, D.; Wudy, K.; Drexler, M. Sintering Study of Polyamide 12 Particles for Selective Laser Melting. Int. J. Recent Contrib. from Eng. Sci. IT **2015**, 3 (1), 28–33. https://doi.org/10.3991/IJES.V3I1.4290.

(75) Berretta, S.; Wang, Y.; Davies, R.; Ghita, O. R. Polymer Viscosity, Particle Coalescence and Mechanical Performance in High-Temperature Laser Sintering. J. Mater. Sci. **2016**, 51 (10), 4778–4794. https://doi.org/10.1007/S10853-016-9761-6.

(76) Laumer, T.; Wudy, K.; Drexler, M.; Amend, P.; Roth, S.; Drummer, D.; Schmidt, M. Fundamental Investigation of Laser Beam Melting of Polymers for Additive Manufacture. J. Laser Appl. **2014**, 26 (4), 042003. https://doi.org/10.2351/1.4892848.

(77) Asoro, M. Coalescence and Sintering in Metallic Nanoparticles: In-Situ Transmission Electron Microscopy (TEM) Study. **2012**

(78) Gibson, I.; Rosen, D.; Stucker, B.; Khorasani, M. Additive Manufacturing Technologies. Addit. Manuf. Technol. **2021**. https://doi.org/10.1007/978-3-030-56127-7.

(79) Hejmady P., van Breemen L.C.A., Anderson P.D., Cardinaels R.M. Laser sintering of polymer particle pairs studied by in situ visualization. Soft Matter. **2019,** 15 (6), 1373-1387.

(80) Wu, B.; Zhu, K.; Wang, F.; Wen, X.; Li, M.; Yang, Y.; Yang, J. Development of PA6/GO Microspheres with Good Processability for SLS 3D Printing. Polymer engineering. **2022**. https://doi.org/10.1002/pen.25957

(81) A. Salehi, G. Pircheraghi, R. Foudazi. Pore structure evolution during sintering of HDPE particles. Polymer. **2019**, 183. Elsevier

(82) Zhu, W.; Yan, C.; Shi, Y.; Wen, S.; Han, C.; Cai, C.; Liu, J.; Shi, Y. Study on the Selective Laser Sintering of a Low-Isotacticity Polypropylene Powder. Rapid Prototyp. J. **2016**, 22 (4), 621–629. https://doi.org/10.1108/RPJ-02-2015-0014/FULL/PDF.

(83) Yau, W. W. A Rheology Theory and Method on Polydispersity and Polymer Long-Chain Branching. Polymer (Guildf). **2007**, 48 (8), 2362–2370. https://doi.org/10.1016/j.polymer.2007.01.073

(84) Bernard, D. A.; Noolandi, J. Zero-Shear Viscosity Exponent and Polydispersity Effects. Macromolecules **1982**, 15 (6), 1553–1559. https://doi.org/10.1021/MA00234A018

(85) Hornsby, P.R., Maxwell, A.S. Mechanism of sintering between polypropylene beads. J. Material Sci.1992, 27, 2525–2533. https://doi.org/10.1007/BF01105065

(86) Bischoff White, E. E.; Henning Winter, · H; Rothstein, J. P.; Bischoff White, E. E.; Rothstein, · J P; Henning Winter, H. EExtensional-Flow-Induced Crystallization of Isotactic Polypropylen. Rheol Acta. **2012**, 51, 303–314. https://doi.org/10.1007/s00397-011-0595-5.

(87) Dee, G. T.; Sauer, B. B. The Surface Tension of Polymer Blends: Theory and Experiment. Macromolecules. **1993**, 26 (11), 2771–2778. https://doi.org/10.1021/MA00063A021.

(88) Qian, Z.; Minnikanti, V. S.; Sauer, B. B.; Dee, G. T.; Kampert, W. G.; Archer, L. A. Surface Tension of Polystyrene Blends: Theory and Experiment. J Polym Sci Part B Polym Phys **2009**, 47, 1666–1685. https://doi.org/10.1002/polb.21771.

(89) Van Hooreweder, B.; Moens, D.; Boonen, R.; Kruth, J. P.; Sas, P. On the Difference in Material Structure and Fatigue Properties of Nylon Specimens Produced by Injection Molding and Selective Laser Sintering. Polym. Test. **2013**, 32 (5), 972–981.

https://doi.org/10.1016/J.POLYMERTESTING.2013.04.014.

(90) Abbott, C. S.; Sperry, M.; Crane, N. B. Relationships between Porosity and Mechanical Properties of Polyamide 12 Parts Produced Using the Laser Sintering and Multi-Jet Fusion Powder Bed Fusion Processes. J. Manuf. Process. **2021**, 70, 55–66. https://doi.org/10.1016/J.JMAPRO.2021.08.012.

(91) Flodberg, G.; Pettersson, H.; Yang, L. Pore Analysis and Mechanical Performance of Selective Laser Sintered Objects. Addit. Manuf. **2018**, 24, 307–315. https://doi.org/10.1016/J.ADDMA.2018.10.001.

(92) Bourell, D. L.; Watt, T. J.; Leigh, D. K.; Fulcher, B. Performance Limitations in Polymer Laser Sintering. Phys. Procedia **2014**, 56, 147–156. https://doi.org/10.1016/j.phpro.2014.08.157.

(93) Schmid, M.; Kleijnen, R.; Vetterli, M.; Wegener, K. Influence of the Origin of Polyamide 12 Powder on the Laser Sintering Process and Laser Sintered Parts. Applied Sciences. **2017** - mdpi.com. https://doi.org/10.3390/app7050462.

(94) DK Leigh. A Comparison of Polyamide 11 Mechanical Properties Between Laser Sintering and Traditional Molding. International Solid Freeform Fabrication. **2012** repositories.lib.utexas.edu

(95) Gong, X.; Gao, X.; Yu, N.; Zhang, D.; Tan, L.; Li, J. Characterization of Thermally Treated Polypropylene Powders with Wide Sintering Window for Powder Bed Fusion of Polymers. Polym. Test. **2021**, 96. https://doi.org/10.1016/J.POLYMERTESTING.2021.107078

(96) Goodridge, R. D.; Tuck, C. J.; Hague, R. J. M. Laser Sintering of Polyamides and Other Polymers. Prog. Mater. Sci. **2012**, 57 (2), 229–267. https://doi.org/10.1016/J.PMATSCI.2011.04.001.

(97) Averardi, A.; Cola, C.; Zeltmann, S. E.; Gupta, N. Effect of Particle Size Distribution on the Packing of Powder Beds: A Critical Discussion Relevant to Additive Manufacturing. Mater. Today Commun. **2020**, 24, 100964. https://doi.org/10.1016/J.MTCOMM.2020.100964.

(98) Berretta, S.; Ghita, O.; KE Evans. Morphology of Polymeric Powders in Laser Sintering (LS): From Polyamide to New PEEK Powders. European Polymer Journal. **2014**. Elsevier.

(99) Schiochet Nasato, D.; Pöschel, T. Influence of Particle Shape in Additive Manufacturing: Discrete Element Simulations of Polyamide 11 and Polyamide 12. Addit. Manuf. **2020**, 36, 101421. https://doi.org/10.1016/J.ADDMA.2020.101421.

(100) Haeri, S.; Wang, Y.; Ghita, O.; Sun, J. Discrete Element Simulation and Experimental Study of Powder Spreading Process in Additive Manufacturing. Powder Technol. **2017**, 306, 45–54. https://doi.org/10.1016/J.POWTEC.2016.11.002.

(101) Deng, X. L.; Davé, R. N. Dynamic Simulation of Particle Packing Influenced by Size, Aspect Ratio and Surface Energy. Granul. Matter **2013**, 15 (4), 401–415. https://doi.org/10.1007/S10035-013-0413-0/FIGURES/10.

(102) Gusarov, A. V.; Kovalev, E. P. Model of Thermal Conductivity in Powder Beds. Phys. Rev. B - Condens. Matter Mater. Phys. **2009**, 80 (2). https://doi.org/10.1103/PHYSREVB.80.024202.

(103) Kruth J-P.; Levy G.; Klocke F.; Childs THC. Consolidation phenomena in laser and powder-bed based layered manufacturing. CIRP Ann Manuf Technol. **2007**, 56, 730–59.

(104) Pang, Y.; Dong, X.; Zhang, X.; Liu, K.; Chen, E.; Han, C. C.; Wang, D. Interplay between Crystallization Behaviors and Extensional Deformation of Isotactic Polypropylene and Its Blend with Poly(Ethylene-Co-Octene). Polymer (Guildf). **2008**, 49 (10), 2568–2577. https://doi.org/10.1016/J.POLYMER.2008.03.050.

(105) George, A.; Dadmun, M. D. Impact of Polymer Molecular Weight and Dispersity on the Coalescence of Polypropylene Powders Suitable for Laser Powder Bed Fusion. Submitted to Macromolecules **2024**

(106) O'Driscoll, K., Amin Sanayei, R. Chain-Length Dependence of the Glass Transition Temperature. Macromolecules **1991**, 24 (15), 4479–4480. https://doi.org/10.1021/MA00015A038.

(107) Askar, S.; Li, L.; Torkelson, J. M. Polystyrene-Grafted Silica Nanoparticles: Investigating the Molecular Weight Dependence of Glass Transition and Fragility Behavior. Macromolecules **2017**, 50 (4), 1589–1598. https://doi.org/10.1021/ACS.MACROMOL.7B00079/ASSET/IMAGES/LARGE/MA2017-000792_0004.JPEG

(108) White, R. P.; Lipson, J. E. G. Polymer Free Volume and Its Connection to the Glass Transition. Macromolecules **2016**, 49 (11), 3987–4007. https://doi.org/10.1021/ACS.MACROMOL.6B00215/ASSET/IMAGES/MA-2016-00215G_M024.GIF.

(109) Arranz-Andrés, J.; Peña, B.; Benavente, R.; Pérez, E.; Cerrada, M. L. Influence of Isotacticity and Molecular Weight on the Properties of Metallocenic Isotactic Polypropylene. Eur. Polym. J. **2007**, 43 (6), 2357–2370. https://doi.org/10.1016/J.EURPOLYMJ.2007.03.034.

(110) Li, J.; Zhu, Z.; Li, T.; Peng, X.; Jiang, S.; Turng, L. S. Quantification of the Young's Modulus for Polypropylene: Influence of Initial Crystallinity and Service Temperature. J. Appl. Polym. Sci. **2020**, 137 (16), 48581. https://doi.org/10.1002/APP.48581.

(111) Zhu, W.; Yan, C.; Shi, Y.; Wen, S.; Liu, J.; Shi, Y. Investigation into Mechanical and Microstructural Properties of Polypropylene Manufactured by Selective Laser Sintering in

Comparison with Injection Molding Counterparts. Mater. Des. **2015**, 82, 37–45. https://doi.org/10.1016/j.matdes.2015.05.043.

(112) Tan, L. J.; Zhu, W.; Sagar, K.; Zhou, K. Comparative Study on the Selective Laser Sintering of Polypropylene Homopolymer and Copolymer: Processability, Crystallization Kinetics, Crystal Phases and Mechanical Properties. Addit. Manuf. **2021**, 37, 101610. https://doi.org/10.1016/j.addma.2020.101610.

(113) Morrow, D. R.; Newman, B. A. Crystallization of Low-Molecular-Weight Polypropylene Fractions. J. Appl. Phys. **1968**, 39 (11), 4944–4950. https://doi.org/10.1063/1.1655891

(114) Dev Singh, D.; Mahender, T.; Raji Reddy, A. Powder Bed Fusion Process: A Brief Review. Mater. Today Proc. **2021**, 46, 350–355. https://doi.org/10.1016/J.MATPR.2020.08.415.

(115) Bain, E. D. Polymer Powder Bed Fusion Additive Manufacturing: Recent Developments in Materials, Processes, and Applications. ACS Symp. Ser. **2019**, 1315, 7–36. https://doi.org/10.1021/BK-2019-1315.CH002.

(116) C.R. Deckard. Method and apparatus for producing parts by selective sintering.**1989**, 4,538-863

(117) Das, A.; Chatham, C. A.; Fallon, J. J.; Zawaski, C. E.; Gilmer, E. L.; Williams, C. B.; Bortner, M. J. Current Understanding and Challenges in High Temperature Additive Manufacturing of Engineering Thermoplastic Polymers. Addit. Manuf. **2020**, 34. https://doi.org/10.1016/j.addma.2020.101218.

(118) Ziegelmeier, S.; Christou, P.; Wöllecke, F.; Tuck, C.; Goodridge, R.; Hague, R.; Krampe, E.; Wintermantel, E. An Experimental Study into the Effects of Bulk and Flow Behaviour of Laser Sintering Polymer Powders on Resulting Part Properties. J. Mater. Process. Technol. **2015**, 215 (1), 239–250. https://doi.org/10.1016/j.jmatprotec.2014.07.029.

(119) Duddleston L .Polyamide (Nylon) 12 Powder Degradation during the Selective Laser

Sintering Process. Univ. Wisconsin. **2015**.https://doi.org/10.13140/RG.2.1.3548.8487.

(120) Jallo, L. J.; Chen, Y.; Bowen, J.; Etzler, F.; Dave, R. Prediction of Inter-Particle Adhesion Force from Surface Energy and Surface Roughness. J. Adhes. Sci. Technol. **2011**, 25, 367–384. https://doi.org/10.1163/016942410X525623.

(121) Mullarney, M. P.; Beach, L. E.; Davé, R. N.; Langdon, B. A.; Polizzi, M.; Blackwood, D. O. Applying Dry Powder Coatings to Pharmaceutical Powders Using a Comil for Improving Powder Flow and Bulk Density. Powder Technol. **2011**, 212 (3), 397–402. https://doi.org/10.1016/j.powtec.2011.06.008.

(123) Tan, P.; Zhou, M.; Tang, C.; Su, Y.; Qi, H. J.; Zhou, K. Multiphysics Modelling of Powder Bed Fusion for Polymers. Virtual Phys. Prototyp. **2023**, 18 (1). https://doi.org/10.1080/17452759.2023.2257191.

(124) George, A.; Dadmun, M. D.; Bryant, J. S.; Taylor T.; Bortner, M. J.; Williams, C. B. Impact of Polymer Molecular Weight Blends on the Powder Bed Fusion Process and the Properties of Polypropylene Printed Parts. Submitted to Additve Manufactring, **2024**

(125) Benedetti, L.; Brulé, B.; Decreamer, N.; Evans, K. E.; Ghita, O. Shrinkage Behaviour of Semicrystalline Polymers in Laser Sintering: PEKK and PA12. Mater. Des. **2019**, 181. https://doi.org/10.1016/j.matdes.2019.107906.

(126) Maulet, T.; Gimenez, J.; Demé, F.; Alcouffe, P.; Vera, R.; Barrès, C.; Fulchiron, R. Effect of Self-Nucleation on the Crystallization Kinetics and the Microstructure of Polypropylene Parts Manufactured by Laser Powder Bed Fusion. Addit. Manuf. **2022**, 59. https://doi.org/10.1016/j.addma.2022.103153

(127) Wang, X.; Wang, Z.; Xiang, S.; Peng, M.; Li, G.; Huang, Y. Developing Polypropylene Copolymer Powder with a Wide Sintering Window for Laser Powder Bed Fusion via Extrusion and In-Blend Annealing. Addit. Manuf. **2024**, 86.

https://doi.org/10.1016/j.addma.2024.104188.

(128) Michelle, Pomatto. Crystallization Behavior, Tailored Microstructure, and Structure-Property Relationships of Poly(Ether Ketone Ketone) and Polyolefins. PhD diss., Virginia Tech, **2024**

(129) Das, A.; Shanmugham, N.; Bortner, M. J. Customized Blends of Polypropylene for Extrusion Based Additive Manufacturing. J. Vinyl Addit. Technol. **2023**, 29 (4), 649–661. https://doi.org/10.1002/VNL.21960

(130) Chatham, C. A.; Zawaski, C. E.; Williams, C. B.; Bobbitt, D. C.; Moore, R. B.; Long, T. E. Semicrystalline Polymer Blends for Material Extrusion Additive Manufacturing Printability: A Case Study with Poly(Ethylene Terephthalate) and Polypropylene. **2019**. https://doi.org/10.1002/mame.201800764.

(131) Jiang, Y.; Wu, J.; Leng, J.; Cardon, L.; Zhang, J. Reinforced and Toughened PP/PS Composites Prepared by Fused Filament Fabrication (FFF) with in-Situ Microfibril and Shish-Kebab Structure. Polymer (Guildf). **2020**, 186. https://doi.org/10.1016/j.polymer.2019.121971.

(132) Ho, Q. B.; Kontopoulou, M. Improving the Adhesion and Properties in the Material Extrusion of Polypropylene by Blending with a Polyolefin Elastomer. Addit. Manuf. **2022**, 55. https://doi.org/10.1016/J.ADDMA.2022.102818

(133) Harris, A. M.; Lee, E. C. Improving Mechanical Performance of Injection Molded PLA by Controlling Crystallinity. J. Appl. Polym. Sci. **2008**, 107 (4), 2246–2255. https://doi.org/10.1002/APP.27261.

(134) Vidakis, N.; Petousis, · M; Kechagias, · J D. A Comprehensive Investigation of the 3D Printing Parameters' Effects on the Mechanical Response of Polycarbonate in Fused Filament Fabrication. Prog. Addit. Manuf. **2022**, 7, 713–722.

https://doi.org/10.1007/s40964-021-00258-3

(135) Fang, L.; Yan, Y.; Agarwal, O.; Seppala, J. E.; Hemker, K. J.; Kang, S. H. Processing-Structure-Property Relationships of Bisphenol-A-Polycarbonate Samples Prepared by Fused Filament Fabrication. Addit. Manuf. **2020**, 35, 101285. https://doi.org/10.1016/J.ADDMA.2020.101285.

(136) Faroze, F.; Srivastava, V.; Batish, A. Enhancing Mechanical Properties of Polycarbonate Parts Developed by Fused Filament Fabrication Using RSM-TOPSIS Hybrid Approach.Wiley Online Libr. **2023**, 63 (12), 4186–4206. https://doi.org/10.1002/pen.26517.

(137) Bellehumeur, C.; Li, L.; Sun, Q.; Gu, P. Modeling of Bond Formation Between Polymer Filaments in the Fused Deposition Modeling Process. J. Manuf. Process. **2004**, 6 (2). https://doi.org/10.1016/S1526-6125(04)70071-7

(138) Gonabadi, H.; Yadav, A.; Bull, S. J. The Effect of Processing Parameters on the Mechanical Characteristics of PLA Produced by a 3D FFF Printer. Int. J. Adv. Manuf. Technol. **2020**, 111 (3–4), 695–709. https://doi.org/10.1007/S00170-020-06138-4.

(139) Ravi, A. K.; Deshpande, A.; Hsu, K. H. An In-Process Laser Localized Pre-Deposition Heating Approach to Inter-Layer Bond Strengthening in Extrusion Based Polymer Additive Manufacturing. J. Manuf. Process. **2016**, 24, 179–185. https://doi.org/10.1016/j.jmapro.2016.08.007.

(140) Li, H.; Wang, T.; Sun, J.; Yu, Z. The Effect of Process Parameters in Fused Deposition Modelling on Bonding Degree and Mechanical Properties. Rapid Prototyp. J. **2018**, 24 (1), 80–92. https://doi.org/10.1108/RPJ-06-2016-0090/FULL/PDF.

(141) Shaffer, S.; Yang, K.; Vargas, J.; Di Prima, M. A.; Voit, W. On Reducing Anisotropy in 3D Printed Polymers via Ionizing Radiation. Polymer (Guildf). **2014**, 55 (23), 5969–5979.

https://doi.org/10.1016/J.POLYMER.2014.07.054.

(142) Appuhamillage, G. A.; Reagan, J. C.; Khorsandi, S.; Davidson, J. R.; Voit, W.; Smaldone, R. A., 3D printed remendable polylactic acid blends with uniform mechanical strength enabled by a dynamic Diels–Alder reaction. Polymer Chemistry **2017,** 8 (13), 2087-2092

(143) Kumar, M.; Ramakrishnan, R.; Omarbekova, A. 3D Printed Polycarbonate Reinforced Acrylonitrile-Butadiene-Styrene Composites: Composition Effects on Mechanical Properties, Micro-Structure and Void Formation Study †. J. Mech. Sci. Technol. **2019**, 33 (11), 5219–5226. https://doi.org/10.1007/s12206-019-1011-9.

(144) Suárez-Macías, J.; Terrones-Saeta, J. M.; Iglesias-Godino, F. J.; Corpas-Iglesias, F. A., Surface Treatments with Dichloromethane to Eliminate Printing Lines on Polycarbonate Components Printed by Fused Deposition Modelling Technology. Materials **2020,** 13 (12), 2724

(145) Puglisi, C.; Sturiale, L.; Montaudo, G., Thermal Decomposition Processes in Aromatic Polycarbonates Investigated by Mass Spectrometry. Macromolecules **1999,** 32 (7), 2194-2203

(146) Diepens, M.; Gijsman, P., Photodegradation of bisphenol A polycarbonate. Polymer Degradation and Stability **2007,** 92 (3), 397-406

(147) Huang, J.; He, C.; Li, X.; Pan, G.; Tong, H., Theoretical studies on thermal degradation reaction mechanism of model compound of bisphenol A polycarbonate. Waste management (Elmsford) **2018,** 71, 181-191

(148) Yazdan Mehr, M.; van Driel, W. D.; Jansen, K. M. B.; Deeben, P.; Boutelje, M.; Zhang, G. Q., Photodegradation of bisphenol A polycarbonate under blue light radiation and its effect on optical properties. Optical materials **2013,** 35 (3), 504-508.

(149) Montaudo, G.; Puglisi, C.; Samperi, F., Thermal decomposition processes in

polycarbonates. Polymer Degradation and Stability **1989,** 26 (3), 285-304

(150) Rivaton, A.; Mailhot, B.; Soulestin, J.; Varghese, H.; Gardette, J. L. Comparison of the Photochemical and Thermal Degradation of Bisphenol-A Polycarbonate and Trimethylcyclohexane–Polycarbonate. Polym. Degrad. Stab. **2002**, 75 (1), 17–33. https://doi.org/10.1016/S0141-3910(01)00201-4.

(151) Rivaton, A. Recent Advances in Bisphenol-A Polycarbonate Photodegradation. Polym. Degrad. Stab. **1995**, 49 (1), 163–179. https://doi.org/10.1016/0141-3910(95)00069-X.

(152) Rivatont, A.; Sallet, D.; Lemairet, J. The Photochemistry of Bisphenoi-A Polycarbonate Reconsidered. Polym. Photochem. **1983**, 3, 463–481.

(153) Riggins, A. W.; Yu, J. H.; Dadmun, M. D. Increasing the Isotropy of 3D Printed Poly(Ether Ether Ketone) Using a Combination of Bimodal Polymer Blends and Post-Process Thermal Annealing. Addit. Manuf. **2024**, 84, 104127. https://doi.org/10.1016/j.addma.2024.104127.

(154) Ko, Y. S.; Herrmann, D.; Tolar, O.; Elspass, W. J.; Brändli, C. Improving the Filament Weld-Strength of Fused Filament Fabrication Products through Improved Interdiffusion. **2019**. https://doi.org/10.1016/j.addma.2019.100815.

(155) Kallel, A. C.; Koutiri, I.; Babaeitorkamani, E.; Khavandi, A.; Tamizifar, M.; Shirinbayan, M.; Tcharkhtchi, A. Study of Bonding Formation between the Filaments of PLA in FFF Process. Int. Polym. Process. **2019**, 34 (4), 434–444. https://doi.org/10.3139/217.3718/HTML.

(156) Zhou, M.; Zhou, X.; Si, L.; Chen, P.; Li, M.; Zhang, Y.; Zhou, H. Modeling of Bonding Strength for Fused Filament Fabrication Considering Bonding Interface Evolution and Molecular Diffusion. J. Manuf. Process. **2021**, 68, 1526–6125. https://doi.org/10.1016/j.jmapro.2021.06.064.

(157) Gurrala, P. K.; Regalla, S. P. Part Strength Evolution with Bonding between Filaments in Fused Deposition Modelling. Virtual Phys. Prototyp. **2014**, 9 (3), 141–149. https://doi.org/10.1080/17452759.2014.913400.

(158) Shi, Y.; Liu, P.; Wu, X.; Shi, H.; Huang, H.; Wang, H.; Gao, S. Insight into Chain Scission and Release Profiles from Photodegradation of Polycarbonate Microplastics. Water Res. **2021**, 195, 116980. https://doi.org/10.1016/j.watres.2021.116980.

(159) Tjandraatmadja, G. F.; Burn, L. S.; Jollands, M. J. THE EFFECTS OF ULTRAVIOLET RADIATION ON POLYCARBONATE GLAZING Effects of UV on Polycarbonate Glazing. **1999**.

(160) Moetazedian, A.; Gleadall, A.; Han, X.; Ekinci, A.; Mele, E.; Silberschmidt, V. V. Mechanical Performance of 3D Printed Polylactide during Degradation. Addit. Manuf. **2021**, 38, 101764. https://doi.org/10.1016/J.ADDMA.2020.101764

(161) Ceretti, D.V.A.; Marien, Y.W.; Edeleva, M.; La Gala, A.; Cardon, L.; D'hooge, D.R. Thermal and Thermal-Oxidative Molecular Degradation of Polystyrene and Acrylonitrile Butadiene Styrene during 3D Printing Starting from Filaments and Pellets. Sustainability **2022**, 14, 15488

(162) Qiu, H.; Bousmina, M. Molecular Weight Polydispersity Effects on Diffusion at Polymer/Polymer Interfaces. Can. J. Chem. Eng. **2002**, 80 (6), 1206–1213. https://doi.org/10.1002/CJCE.5450800623.

Vita

Akan Archibong George earned a BSc in Chemistry from the University of Lagos, Nigeria, in November 2016. He subsequently worked as a Research Chemist at Vitapur Nigeria Limited for two years. In Fall 2019, Akan joined Dr. Mark Dadmun's research group at the University of Tennessee, Knoxville, where he completed his Ph.D. in Polymer Chemistry in Fall 2024.